CALIFORNIA
ENERGY COMMISSION

Energy Research and Development Division

FINAL PROJECT REPORT

Intraurban Enhancements to Probabilistic Climate Forecasting for the Electric System

Gavin Newsom, Governor

January 2021 | CEC-500-2021-003

PREPARED BY:

Primary Author:
Haider Taha

Altostratus Inc.
940 Toulouse Way
Martinez, CA 94553
(925) 228-1573
http://altostratus.com

Contract Number: EPC-15-070

PREPARED FOR:
California Energy Commission

Yu Hou
Project Manager

Jonah Steinbuck, Ph.D.
Office Manager
ENERGY GENERATION RESEARCH OFFICE

Laurie ten Hope
Deputy Director
ENERGY RESEARCH AND DEVELOPMENT DIVISION

Drew Bohan
Executive Director

ACKNOWLEDGEMENTS

This work was funded by the California Energy Commission (CEC) under Agreement No. EPC-15-070. Support, guidance, and leadership provided by CEC Agreement Manager, Yu Hou, were critical in helping perform and complete this project and are very much appreciated. The project technical advisory committee members, Yu Hou (CEC), Susan Wilhelm (CEC), William Dean (California Environmental Protection Agency), Ash Lashgari (California Air Resources Board), David Fink (Climate Resolve), and Brian D'Agostino (San Diego Gas & Electric Company/Sempra) are acknowledged for their time and providing feedback during the course of this project.

The following are acknowledged for assistance and providing data used in this project: Earth Define/CALFIRE for tree canopy data; Southern California Association of Governments for fine-resolution land-use/land-cover data; City of Fresno for geographic information system land-use data; City of Bakersfield for land-use data; City of San Francisco for land-use data; Association of Bay Area Governments for land-use and land-cover data; City of Los Angeles for building footprint information; and County of Los Angeles for land-use and building footprint information.

PREFACE

The California Energy Commission's (CEC) Energy Research and Development Division supports energy research and development programs to spur innovation in energy efficiency, renewable energy and advanced clean generation, energy-related environmental protection, energy transmission and distribution and transportation.

In 2012, the Electric Program Investment Charge (EPIC) was established by the California Public Utilities Commission to fund public investments in research to create and advance new energy solutions, foster regional innovation and bring ideas from the lab to the marketplace. The CEC and the state's three largest investor-owned utilities—Pacific Gas and Electric Company, San Diego Gas & Electric Company and Southern California Edison Company—were selected to administer the EPIC funds and advance novel technologies, tools, and strategies that provide benefits to their electric ratepayers.

The CEC is committed to ensuring public participation in its research and development programs that promote greater reliability, lower costs, and increase safety for the California electric ratepayer and include:

- Providing societal benefits.
- Reducing greenhouse gas emission in the electricity sector at the lowest possible cost.
- Supporting California's loading order to meet energy needs first with energy efficiency and demand response, next with renewable energy (distributed generation and utility scale), and finally with clean, conventional electricity supply.
- Supporting low-emission vehicles and transportation.
- Providing economic development.
- Using ratepayer funds efficiently.

Intraurban Enhancements to Probabilistic Climate Forecasting for the Electric System is the final report for Contract Number EPC-15-070 conducted by Altostratus Inc. The information from this project contributes to the Energy Research and Development Division's EPIC Program.

For more information about the Energy Research and Development Division, please visit the CEC's research website (www.energy.ca.gov/research/) or contact the CEC at 916-327-1551.

ABSTRACT

Probabilistic climate forecasts for the electric system are currently produced using climate models at relatively coarse resolutions and observations from sparse networks of meteorological monitors, mostly at airports. The forecasts and analyses do not take into account the fine-scale intraurban variations in microclimates resulting from effects of urban land use, heat or cool islands, and intraurban heat transport, or future changes. Existing building energy modeling practices also do not take these effects into account.

This project developed a method for creating probabilistic fine-scale microclimate (temperature) zones in California, focusing on summer conditions in the Los Angeles region and the San Francisco Bay Area. The method was applied to current and future climates and land use. Forecasting errors and uncertainties were reduced by improving performance of the urban Weather Research and Forecasting model. Model validation used observational weather data from a dense network of automated weather monitoring stations as well as weather reporting used in aviation and by meteorologists.

The project found that the magnitudes of intraurban temperature variations are larger than the temperature differences across boundaries of the existing climate zones adopted by the Energy Commission, sometimes by severalfold. The results suggest that redrawing the current climate-zone boundaries in urban areas could provide more accurate forecasting for the electric system, and optimize allocation of generating resources. The project reduced the mean urban temperature forecasting error by up to 3.2°F (1.8°C) in the San Francisco Bay Area (up to 46 percent reduction in error) and up to 1.4°F (0.8°C) in the Los Angeles region (up to 33 percent reduction in error). Conservatively assuming an average improvement of 0.9°F (0.5°C) in forecasting peak temperatures in Californian cities, this translates into a more accurate allocation of approximately 500 megawatts in generating capacity in the California Independent System Operator service territory.

Keywords: Climate zones; intraurban microclimates; Land use; Meteorological modeling; Probabilistic forecasting; Urban climate

Please use the following citation for this report:

Taha, Haider. 2021. *Intraurban Enhancements to Probabilistic Climate Forecasting for the Electric System*. California Energy Commission. Publication Number: CEC-500-2021-003.

TABLE OF CONTENTS

LIST OF FIGURES

Page

LIST OF TABLES

Page

EXECUTIVE SUMMARY

Introduction

Probabilistic decadal, seasonal, and short-term climate forecasts for the electric system are typically produced with climate models at relatively coarse resolutions (3 to 10 kilometers) and observations from sparse networks of meteorological monitors, mostly at airports. New technologies and models can increase the granularity of climate forecasting and offer the potential for greater accuracy in planning for current and future demands on California's electric grid.

The foundation for current forecasts and models includes 16 climate zones defined in the California Energy Commission's 1995 publication, *California Climate Zone Descriptions for New Buildings*, which formed the basis for the state's Building Energy Efficiency Standards to conserve and efficiently use energy resources in residential and nonresidential building construction. Because building standards, not climate, prompted the creation of climate zones, definitions were derived from spatial properties and domains guided by factors other than, and in addition to, climate. For ease of enforcement, the California Energy Commission has maintained climate zone boundaries fairly consistent with city and utility jurisdictional boundaries and avoided creating pockets within a climate zone.

However, many climate zones contain microclimates that resemble a different climate. These microclimates have widely varying characteristics and thus different energy needs. Current forecasts and observational analyses do not consider the fine-scale intraurban variations in microclimates that result from the effects of urban land use, localized heat or cool islands, and intraurban heat transport, or their respective changes in the future. Nor are these effects considered in prevailing building energy modeling practices.

A demand exists for a method to create probabilistic fine-scale intraurban microclimate (temperature) zones in California based on observations and fine-scale atmospheric modeling. Such a method is desirable for current and future climates, as well as for changing land-use conditions, to reduce errors and uncertainties in climate forecasting for the electric system. The advent of increased computing power, more accurate fine-resolution atmospheric and land-surface models, a higher density of observational weather networks, and powerful data management and processing tools erases the need for climate zones to be large and contiguous. These new technologies can help to optimize energy system allocations, as well as energy modeling.

Project Purpose

The main goal of this project was to demonstrate that improvements in model performance and creation of probabilistic fine-scale microclimate (temperature) zones that consider the variations in intraurban climates can improve planning and forecasting for California's electric grid. Improved forecasting and planning would also optimize the allocation of generating resources and increase the grid's resilience to short- and long-term climate variations. By extension, such improvements would reduce greenhouse gas emissions and improve thermal environmental conditions.

A parallel goal was to reduce urban-climate forecasting errors and uncertainties related to the electric system by improving performance of the urban Weather Research and Forecasting (uWRF) model.

Project Approach

Using a much finer grid size (500 meters to 2 km), the project developed a method for creating current and future fine-scale microclimate (temperature) zones (with length scales ranging from 5 to 15 km), focusing on summer conditions in the Los Angeles region and the greater San Francisco Bay Area.

To improve uWRF meteorological-model performance, Altostratus Inc. applied study-modified and customized urban parameterizations and representations in the atmospheric and land-surface modules of uWRF. Three configurations were established to track incremental improvements in performance: (1) a reference state, obtained by running the Weather Research and Forecasting modeling system as commonly done in weather forecasting, without invoking any specific urban parameterizations; (2) a second meteorology state, obtained by running uWRF with the standard urban parameterizations, as often done by urban-climate modelers; and (3) a third state, obtained by running uWRF with the Altostratus Inc. study-specific modifications to input (bottom-up approach for surface characterizations) and model parameterizations.

Following the establishment of atmospheric-model performance, simulations were carried out to develop microclimate (temperature) zones for current and future climates. For current climate, Altostratus Inc. used observational data from a dense network of mesonet and metar weather stations to characterize the fine-scale microclimate variations. Mesonets are automated weather monitoring stations that observe mesoscale meteorological phenomena, mesoscale being an intermediate scale between weather systems and microclimates, while metar are weather monitoring networks used in aviation. Future-climate zones were developed based on a combination of observations and fine-scale meteorological modeling.

The project then used the improved uWRF model, along with the fine-scale observations, to quantify the magnitudes of intraurban temperature variations. This included effects of localized heat and cool islands and compared them to those of the current forecasting zones adopted by the California Energy Commission to demonstrate the improvements in electric grid planning and forecasting and in more area- and site-specific energy modeling and calculations.

A technical advisory committee provided feedback that was incorporated during the project. Committee members included Yu Hou and Susan Wilhelm from the California Energy Commission (CEC), Brian D'Agostino of San Diego Gas & Electric/Sempra, William Dean from the California Environmental Protection Agency, Ash Lashgari of the California Air Resources Board, and David Fink from Climate Resolve.

Project Results

The results demonstrate that it is critical to account for intraurban variability in microclimates when forecasting and planning for the electric system. A comparison of the fine-scale temperature zones with the forecast climate zones currently used by the CEC in planning for

the electric system and in building energy modeling showed that the intrazone variability in temperature was considerable and could be several-fold larger than the inter-zone differences.

The project's application of study-modified and customized urban parameterizations and representations in the atmospheric and land-surface modules of uWRF did yield improvements in performance. The project reduced temperature forecasting error with improved uWRF modeling by up to 3.2°F (1.8°C) in the San Francisco Bay Area and up to 1.4°F (0.8°C) in the Los Angeles region. Studies have shown that 1.8°F (1°C) of peak temperatures is equivalent to approximately 500 to 1000 megawatts of power. Thus, even a 0.9°F (0.5°C) reduction in forecasting error systemwide could translate to a reduction or reallocation of approximately 500 megawatts (MW) in generating capacity.

The project results suggest that redrawing climate zone boundaries and/or adopting fine-scale microclimate zones, using improved urban modeling techniques that better represent urban areas in atmospheric models, would benefit the electric system by improving planning and forecasting for California's electric grid and the allocation of generating resources, as well as benefit the creation of weather files for building energy modeling.

Knowledge Transfer

Knowledge generated in this project was provided to interested parties via several pathways. During execution of the contract, progress and results were shared with members of the Technical Advisory Committee. Presentations and webinars were also given to various audiences in addition to the California Energy Commission, including California air districts, the California Environmental Protection Agency, utilities, local and city governments, and public health agencies. Results were also made available in summaries, memos, scientific meetings, and technical papers. Certain data products from the project can also be made available upon request on the Altostratus Inc. file transfer protocol site.

Knowledge developed in this project can assist in planning and reducing vulnerability of the electric grid to changes in climate in short and long terms, as well as to future changes in urban land use. California's investor-owned utilities (IOUs) have expressed interest in the methodology developed in this project, and in the fine-scale climate/temperature zones generated for current and future years. The IOUs also are interested in potentially integrating this approach in their planning tools, and in undertaking future work in this area.

Benefits to Ratepayers

Knowledge generated in this project can benefit California ratepayers by helping to optimize the allocation of generating resources. Conservatively assuming an average improvement of 0.9°F (0.5°C) in forecasting peak temperatures within the California Independent System Operator service territory, the improvement translates into a more accurate allocation of approximately 500 MW in generating capacity, which is equivalent to output from one to three large power plants. The improvement in allocation accuracy can be twice as large, according to study findings. These more optimized allocations translate into savings that can be passed on to the ratepayers. In addition to monetary savings, a more optimized grid performance can result in lowered emissions of greenhouse gas and air pollutants.

CHAPTER 1:
Introduction and Objectives

Probabilistic decadal, seasonal, and short-term climate forecasts for the electric system are typically produced with climate models at relatively coarse resolutions, for example, 3-10 kilometers (km), and observations from sparse networks of meteorological monitors, mostly at airports. These forecasts and observational analyses do not explicitly consider the fine-scale intraurban variations in microclimate that result from effects of varying urban land use, heat or cool islands, and intraurban heat transport or their changes in the future. Nor are these effects considered in current building energy modeling practices (that is, in the creation of weather files).

For forecasting and planning purposes related to building energy use, the California Energy Commission (CEC) defines 16 or 20 climate zones (Kavalec et al., 2009; CEC, 2017) that are generally coarse and with spatial properties and domains that are guided by a number of factors other than and in addition to climate (see Figure 1). Of the two shown in Figure 1, the 16-zones scheme (right) is more climate-responsive than the 20-zones scheme (left) that follows city or utilities boundaries relatively more than climate characteristics.

Because the existing climate zones used in probabilistic decadal and short-term forecasts for the electric system, as well as in energy modeling, were spatially coarse and inclusive of a myriad of various microclimates, a demand exists for methodology to create probabilistic fine-scale intraurban microclimate (temperature) zones in California based on observations and fine-scale atmospheric modeling. This is desirable for current and future climates, as well as for changing land-use conditions, to reduce errors and uncertainties in climate forecasting for the electric system. In this project, the intraurban enhancements to probabilistic forecasting and to the CEC climate zones were developed for summer months, focusing on the Los Angeles region and the greater San Francisco Bay Area. This was done based on observations, that is development of synthetic, representative months, and on fine-scale modeling to account for current conditions, and future changes in climate and land use. The CEC climate zones depicted in Figure 1 were used as reference for comparison with the proposed fine-scale intraurban zones developed based on observations and modeling.

Thus, the main objectives in this study were to:

- Identify weather data sources and mesonet[1] monitor locations in the selected study areas and acquire data as needed
- Analyze the observed meteorology, and characterize the intraurban variations in microclimates at the weather-stations' network scales, focusing on air temperature during summer months of recent years

[1] Mesonets are automated weather monitoring stations that observe mesoscale meteorological phenomena, mesoscale being an intermediate scale between weather systems and microclimates.

- Develop characteristic or synthetic months based on observational weather data from the most recent years (for example, 2013—2015)
- Analyze observed meteorology in terms of energy-relevant metrics, for example, cumulative temperature metrics (degree-hours), peaks (maxima), and dips (minima) at stations and point-forecast locations of interest
- Recast the observational weather data for assimilation into the meteorological model, and for carrying out quantitative model performance evaluation
- Configure the atmospheric model (Weather Research and Forecasting, WRF) and its urbanized parameterizations (in the urbanized Weather Research and Forecasting, uWRF) for the specifics of the regions selected in this study, including application of suitable, best-performing urban parameterizations
- Modify and customize the uWRF model, its input, and parameterizations as required for this specific application
- Develop the meteorological and surface characterizations inputs to the model for current climates, and existing land use and land cover (current conditions)
- Carry out atmospheric modeling of current conditions
- Carry out quantitative model performance evaluation (MPE) and compare the performance of the modified uWRF to that of the standard model
- Develop future-climate meteorological input to WRF and uWRF, via dynamical downscaling of climate models focusing on summer months
- Develop characterizations of future land-use/land-cover and urban extents
- Carry out simulations of future climates and future land-use/land-cover conditions; recompute future-year intraurban variations in climate indicators
- Use the observational data analysis and temperature zoning (clustering), along with modeling results as the basis for development of statistical correlations or descriptive relations between temperature at any mesonet station and a reference point, such as forecast locations, metars, or CEC climate-zone stations
- Develop fine-resolution temperature zones in each area and corresponding correlations, and compare to existing CEC climate zones.

Figure 1: Building Energy Climate Forecast Zones

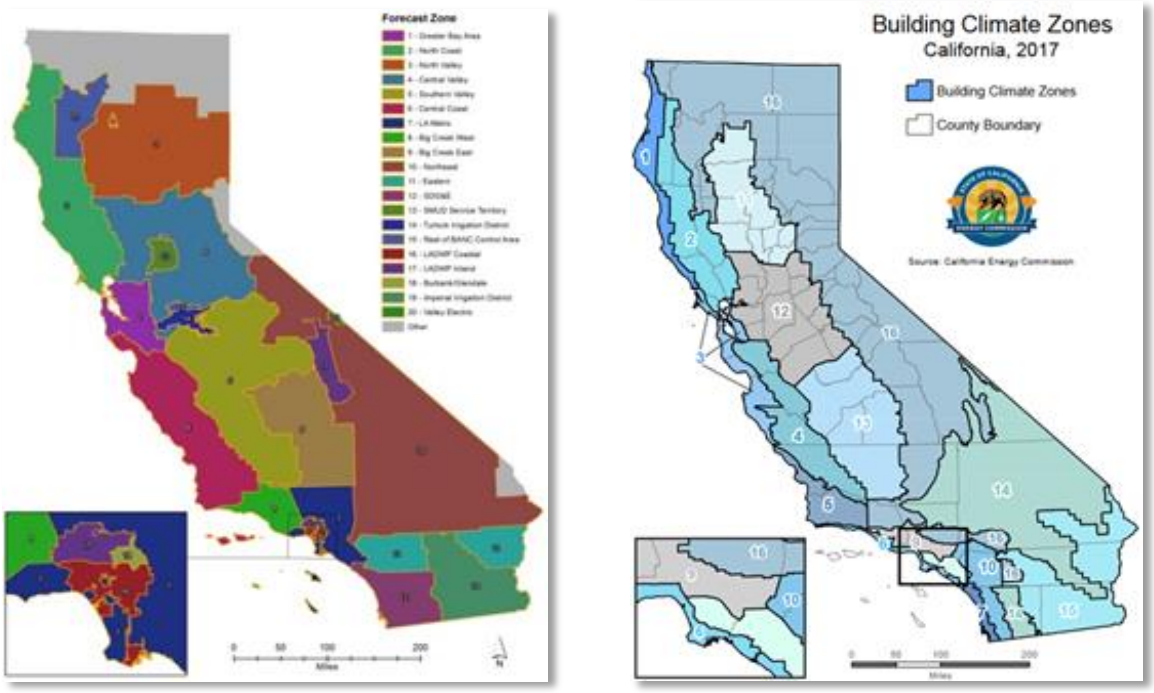

Left: newer scheme, 20 zones. Right: older scheme, 16 zones.

Source: CEC, California Energy Maps (CEC 2017; Kavalec et al., 2009).

CHAPTER 2:
Project Approach

2.1 Observational Meteorological Data

Several datasets were identified, evaluated for use in this study, and acquired as suitable. Datasets were examined at multiple spatial resolutions and geographical coverages, including both point and gridded data. The following observational meteorology datasets were considered for use in this study. Overlap existed, sometimes completely, among various datasets and, in such cases, only a subset was used in this analysis.

- Meteorological Assimilation Data Ingest System (MADIS, madis-data.ncep.noaa.gov): A repository of extensive weather datasets developed and maintained by the National Oceanic and Atmospheric Administration/National Centers for Environmental Prediction (NOAA/NCEP). It consists of and synthesizes data from various providers and, as such, was used mainly and heavily in this study.
- URBANET/National mesonet: An urban-monitors dataset by the National Centers for Environmental Prediction that can be partially accessed via MADIS (depending on access privileges).
- National Weather Service/NOAA Cooperative Observer Program (COOP): A dataset of annual averages and daily maximum and minimum temperatures and precipitation (nws.noaa.gov/om/coop/).
- Daymet (daymet.ornl.gov and urs.earthdata.nasa.gov): Gridded daily datasets at 1 km resolution of parameters including, for example, daily maximum and minimum air temperature, humidity, and precipitation. The data is prepared and maintained by the Oak Ridge National Laboratory.
- WeatherBug (weather.weatherbug.com): A commercial dataset consisting overwhelmingly of citizen weather observing program (CWOP) monitors. While the coverage and the spatial resolution of the monitoring network are relatively high, data quality can be difficult to ascertain and/or control via post-processing.
- Weather Underground (wunderground.com): A commercial dataset covering swathes of urban areas at relatively higher coverages and resolutions in some parts, but, as with the WeatherBug datasets, the quality is not consistently checked and most monitors are privately owned; that is, CWOP, and therefore not always subject to World Meteorological Organization (WMO)-standard siting criteria, maintenance, and/or calibration.
- NOAA MesoWest (www.weather.gov/wrh/): Map-based surface meteorology (point observations). Areas covered in California include the San Francisco Bay Area, Sacramento, San Diego, Los Angeles region, and the Fresno—Bakersfield areas. MesoWest also provides historical data (climate and daily weather information), as well as specific weather-station data.
- PRISM Climate Group (prism.oregonstate.edu) and PRISM UCAR (climatedataguide.ucar.edu): Gridded historical meteorology datasets.

- NCAR (U.S. National Center for Atmospheric Research) datasets 472.0: Hourly historical weather observations at airports or near airways. The dataset is developed and maintained by NCAR, and also made available for use as input to atmospheric models. This dataset also is useful in model performance evaluation.
- Mesowest mesonet (mesowest.utah.edu/): Mesonet data covering most of California and other western states. This dataset also is included in the MADIS system.
- NOAA daily datasets (Livneh et al., 2015): National gridded datasets of daily temperature maxima and minima, and other daily variables, such as precipitation, based mainly on the NOAA COOP observations. Available for several decades to present (2013), with a spatial resolution of 6 km (data.ncdc.noaa.gov).
- California Irrigation Management Information System (CIMIS): A dataset developed mainly for agricultural applications with limited observations in urban areas.
- Network-specific California datasets: Data from various California agencies, including the Air Resources Board, Air Quality Management Districts (of relevance to this project: the South Coast Air Quality Management District, Bay Area Air Quality Management District, and the San Joaquin Valley Air Pollution Control District).
- Utilities-specific mesonet: PG&E and SDG&E mesonets (Pacific Gas & Electric; San Diego Gas & Electric).
- California Climate Data Archive, CALCLIM (calclim.dri.edu): A climate monitoring and data access website for the State of California. It is sponsored by the CEC as a joint effort with the Scripps Institute of Oceanography and the Western Regional Climate Center (WRCC). CALCLIM lists many of the same networks found in MADIS and other data sources listed above. Other useful climate datasets at WRCC can be accessed from wrcc.dri.edu/coop-inventory/ and wrcc.dri.edu/climate-maps.

Figure 2 shows a geographical search window for weather stations that was defined as shown by the white polygon. This search area encompassed the study regions of interest in this project, including the San Francisco Bay Area, the Fresno-Bakersfield area, and the Los Angeles region. From MADIS, the number of monitors with valid data in this search area was about 1,400. This total did not include stations from the Weather Underground and Weather Bug networks, as they were not used in this study, although some of these stations may be included in the MADIS datasets. The number of monitors (mesonet and metar[2] stations) in the study-defined analysis domains of the San Francisco Bay Area was ~245 and, in the Los Angeles region, it was ~330 depending on reporting (these analysis domains are shown in Figure 2). In addition, several upper-air/radiosonde sites were available in each of these regions.

Data acquired from each monitor included variables of interest, such as air temperature, dew point, relative humidity, wind speed, wind direction, wind gusts, solar radiation, pressure, and precipitation. In this application, observed air temperature, dew point, and humidity were at 2 meters (m) (6.5 feet) above ground level (AGL) in most cases; whereas, wind direction and speed were either at 6.1 or 10 m (20 or 32 feet) AGL, in general. Upper-air information were

[2] Metar are weather monitoring networks used in aviation.

also acquired, including radiosonde data from NOAA's National Center for Environmental Information. Radiosonde sites within the search window defined above are located at Vandenberg Air Force Base, Edwards Air Force Base, Los Angeles International Airport (LAX), Oakland International Airport (OAK), Fresno Yosemite International Airport (FAT), San Diego International Airport (SAN), and Point Mugu Air Force Base. Figure 2 shows the locations of weather stations (mesonet, metars, airways, and radiosonde sites) windowed over the areas of interest in this study.

Figure 2: Search Window for Observational Data (Meteorological Monitors)

Top: Overall study area
Bottom left: locations of weather stations in the Los Angeles region (approximately 330 stations). Bottom right: locations in the San Francisco Bay Area (approximately 245 stations).

Source: Altostratus Inc.

In addition to their use in detailed analysis of observed meteorology, the acquired datasets were also recast for use in model performance evaluation, including time series, maxima, minima, bias, error, and index of agreement (Taha and Freed, 2015). The data were also reformatted for input to the meteorological model, that is in four-dimensional data assimilation. The WRF model (Skamarock et al., 2008) was also configured in this study for running with the NOAA/NCEP Global Forecast Model for short-term, days-ahead localized forecasting. Thus, for this additional purpose, a streamlined routine for acquiring Global Forecast Model data in real time from NCEP/NCAR and use in WRF was also implemented. For long-term decadal modeling, dynamical downscaling of climate model output was carried out with the urbanized WRF model (uWRF), as discussed later in this report. Observational data were quality checked to ensure suitability. MADIS allowed for various levels of quality check based on (1) static, station-specific checks, and (2) spatial analysis of observations at the target monitor relative to nearest-neighbor stations (analysis) which, in this case, generally included some four to six stations surrounding the target (buddy check). Thus, the full hourly

meteorological datasets (for June, July, August, and September of 2013, 2014, and 2015) were filtered further to produce secondary quality-checked datasets that were then used in subsequent analysis and in model performance evaluation.

2.2 Land-Use/Land-Cover Data and Preparation of Surface Input to Urbanized Weather Research and Forecasting

2.2.1 Land-Use/Land-Cover Data Sources

To characterize the land use, land cover (LULC), physical, and geometrical properties of the surface, the following datasets were identified and used in this project:

- 30-m National Land Cover Data (NLCD), including Land Use/Land Cover (LULC), vegetation cover, and impervious surfaces (MRLC, 2006)
- 30-m United States Geological Survey (USGS) Anderson Level-II LULC classification (Anderson et al., 2001), including urban and nonurban areas
- Area-specific LULC, following the Anderson USGS Level-IV classification (Anderson et al., 2001), obtained from the cities and counties in the study areas
- Fine-scale, area-specific building footprints and geometry obtained from cities and counties in the study areas
- Google Earth urban morphological and land-cover data (canopy layer)
- 1-m area-specific roof albedo from satellite imagery (Lawrence Berkeley National Lab) (Ban-Weiss et al. 2015)
- 1-m area-specific urban morphological and geometrical data from the National Urban Datasets and Portal Tool (N/WUDAPT; Ching et al., 2009)
- 1-m Earth Define/CALFIRE urban tree-canopy cover (www.earthdefine.com).

To prepare the surface-characterization input to uWRF, the subsequent steps were followed:

- Obtained additional fine-resolution LULC and building-footprint datasets for several counties in the study areas. These included the counties of Kern, Fresno, San Francisco, Santa Clara, Contra Costa, Alameda, San Mateo, Los Angeles, Orange, San Bernardino, Riverside, and Ventura. Additional information was also acquired from associations of governments in the Los Angeles region and the San Francisco Bay Area (Southern California Association of Governments, Association of Bay Area Governments).
- Used the LULC information to derive various parameter inputs to the meteorological model (uWRF) for various schemes that simulate the urban canopy layer as well as for nonurban areas. Urban parameters included building and vegetation frontal-, plan-, and top-area densities, roughness length, view factor, albedo, soil moisture content, shade factor, and other parameters as specific to each modeling scheme.
- Performed analysis of urban-morphology data for buildings, structures, and vegetation (based on Google Earth and National Urban Database and Access Portal Tool datasets) for various urban land-cover categories. These datasets along with building footprint information were used in the calculations of parameters for input to the land-surface models. The morphological categories were also cross-walked to LULC categories.

- Vectorized a 1-m raster tree-cover dataset obtained from EarthDefine/CALFIRE and used in development of certain model-input parameters related to vegetation such as shade factor, soil moisture, and roughness length to complement those derived based on LULC and urban-morphology characteristics.
- Developed future-year land-use input to uWRF based on projection scenarios (Bierwagen et al. 2010; Thorne et al., 2012) and USGS LUCAS datasets (Sleeter et al., 2015) in addition to cross-referencing among various city-specific LULC datasets and NLCD 2011/USGS GIRAS Level-II and Level-IV classes (Anderson et al., 2001) for use as extrapolation templates in data-sparse areas.

The available datasets were merged, after processing, on a grid cell-by-cell basis to develop a detailed bottom-up surface characterization input to the atmospheric and land-surface models. Because of the large amount of data generated in these tasks, this section presents only a few random small samples, as shown in Figure 3, from the various activities carried out in the characterization of LULC and urban morphology (Figure 1 through Figure 13 in Appendix B provide additional examples). The gridded land-cover and morphology information was then used to derive meteorological-model input parameters, including urban fraction, albedo, shade factor, soil moisture, roughness length, anthropogenic heat flux, and other relevant canopy-layer descriptors.

Figure 3: Examples from Land Use, Land Cover Analysis

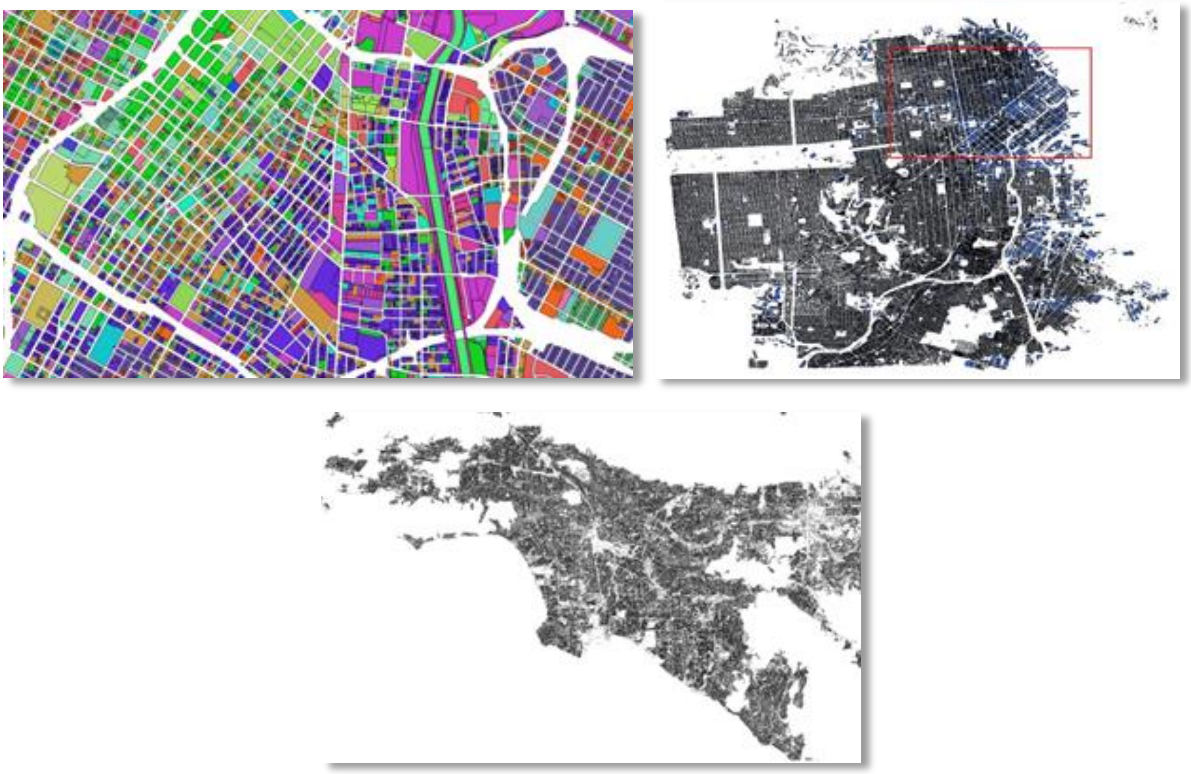

Top left: Sample detail of Los Angeles County land-use classifications (Downtown Los Angeles is the area predominantly color-coded green in this figure) data source: SCAG. Right: San Francisco County building footprints, red rectangle is the downtown San Francisco area, data source: Association of Bay Area Governments. Bottom: Urban tree cover (1-m resolution) in a subdomain of the Los Angeles region (data source: EarthDefine/CALFIRE).

Source: Altostratus Inc.

2.2.2. Development of Surface Input to Urbanized Weather Research and Forecasting

Based on the LULC analysis, fine-scale urban surface physical and geometrical properties input to the urbanized WRF meteorological model (uWRF) was generated in two manners: (1) for areas explicitly covered by particular LULC and/or morphometric datasets, the surface properties were developed directly from these data; and (2) for areas that were not covered by one or more datasets, characterizations were done indirectly. In the latter case, correlations were developed between highly resolved LULC classes and building morphometric properties, such as height, area, frontal-area density, probability distribution of building area with height, and so on. For example, in the Los Angeles County alone, there were about 130 LULC classes, more than 2 million LULC patches, and more than 3 million buildings (thus, more than 6 trillion points for the development of such correlations).

With GIS, centroids were assigned to each LULC patch to more easily correlate with specific buildings in each area and, thus, derive certain properties of interest. The correlations were then used as a basis for computing geometrical, roughness, and drag-related input parameters to uWRF in each area. Figure 4 is a random example from the analysis of building properties versus LULC classes, in this case, average building plan area and average building height within LULC patch 1122 (Figures 14.A through 14.L in Appendix B provide additional examples of such correlations).

The calculations were applied to present years and repeated for developing future-year land-use and land cover scenarios. Data were then merged to develop gridded model input parameters including: LULC coverage (percentage); roof albedo; roof area; mean building heights; mean building floor areas; top-, frontal-, and plan-area densities for buildings; probabilities of building areas at each of 5-m vertical intervals from surface to 40+ m AGL; vegetation cover; soil moisture; roughness length; and drag coefficients. Figure 5 is an example from this analysis (additional examples can be found in Figures 15.1 through 15.16 in Appendix B).

Figure 4: Snapshot from Analysis of Land Use, Land Cover and Building Properties

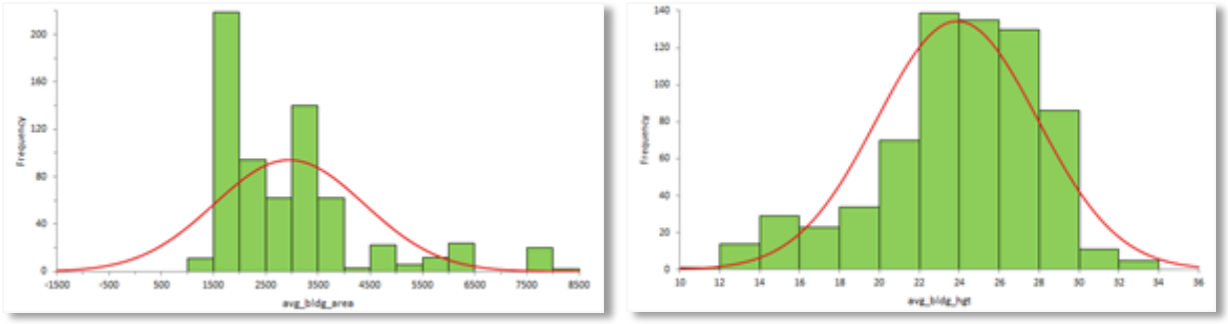

This example is from the Agoura Hills area of Los Angeles County. Left: LULC 1122 (duplexes, triplexes, and condominiums), average building area (m^2) at ground level. Right: LULC 1122 average building height (m).

Source: Altostratus Inc.

Figure 5: Examples from Land Use, Land Cover and Urban Morphology Analysis

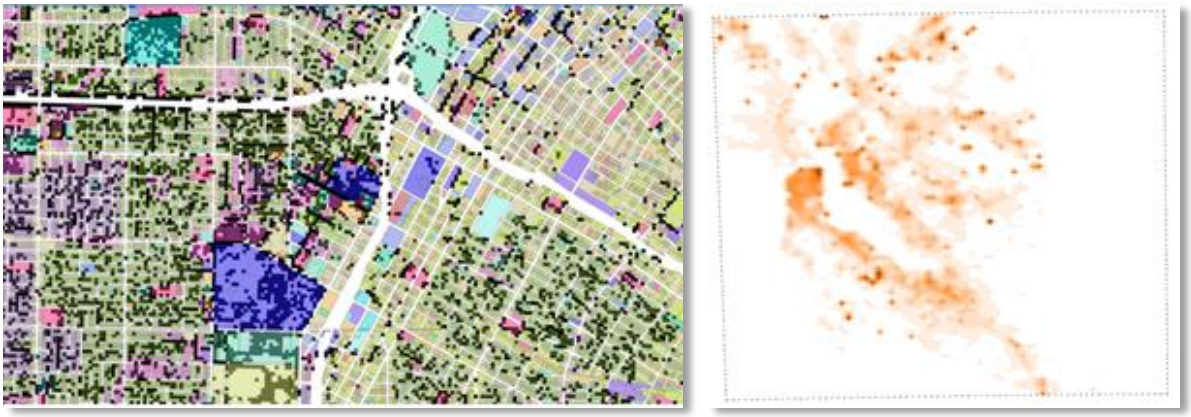

Left: Arbitrary example for an area southwest of Downtown Los Angeles. Background colored tiles represent LULC and the small dark squares represent tree canopy cover >15 percent. Right: Arbitrary example for the San Francisco Bay Area: grid-cell mean building height (light to dark color corresponds to low to tall buildings).

Source: Altostratus Inc.

2.2.3. Development of Future Land Use

As part of the task of modeling future climates, the LUCAS USGS land-use projections (Sleeter et al., 2015) for years 2015, 2030, 2050, and 2100 for the business-as-usual (BAU) case were adopted in this study. Although there were other scenarios available, such as BAU high and BAU low, the BAU scenario selected here is a middle-of-the-road situation representing likely trends in urbanization. A small sample from this analysis is shown in Figure 6 (Figures 16.1 through 16.12 in Appendix B provide additional examples from this analysis).

The LUCAS land-use dataset was originally acquired as raster layers that were then vectorized in this project and recast to the modeling grids of the study areas as shown in the examples below. The figures depict the changes in urban land use in future years — here for 2015 (as reference), 2050, and 2100. The projected future changes in urban land cover were used in this study to revise the thermo-physical properties input to the land-surface and urban modules of the modified uWRF model to capture future-year conditions (in addition to the changes in climate fields, that is, the downscaled projections of meteorology corresponding to those years). The composition and surface physical characteristics of the new urban areas (expanded to in 2050 and 2100) were assumed to be an extension of and having similar properties to the urban areas closest to the current boundaries where the urban expansion would occur.

2.3 Meteorological Modeling

Meteorological modeling in this project was carried out with the WRF system (Skamarock et al., 2008). The urban modules (uWRF) and land-surface model (LSM) in WRF were updated and customized in this project for the specifics of fine-scale intraurban modeling of the selected study regions. The model was modified to (1) ingest the bottom-up surface characterizations developed in this study (discussed in Section 2.2), (2) to trigger the urban parameterizations at grid cells based on physical-properties criteria (not LULC criteria as in the standard WRF),

and (3) modifications to parameterizations so that calculations of roughness, drag, and other properties are wind-direction-dependent.

Figure 6: San Francisco Bay Area and Los Angeles Region Urbanization

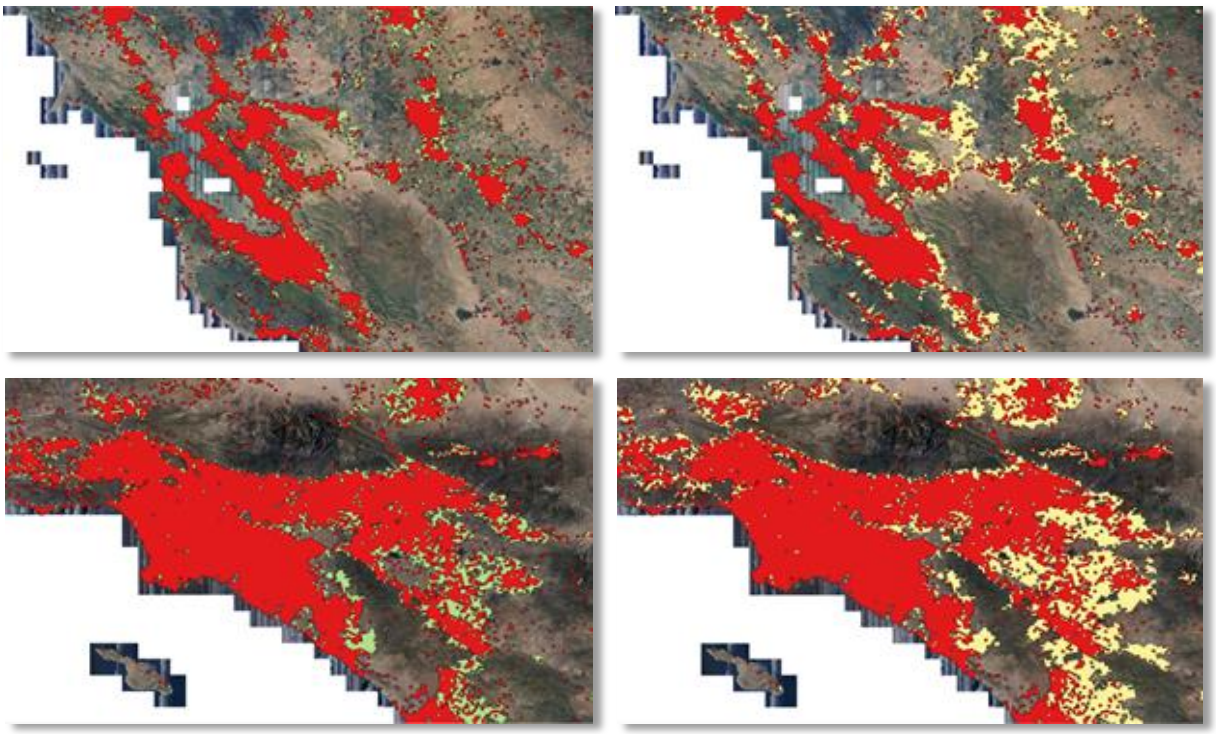

San Francisco Bay Area (top) and Los Angeles region (bottom) urban land use in 2015 (red). Green color represents additional areas urbanized by 2050 (left) and yellow is additional areas urbanized by 2100 (right). Data generated based on Sleeter et al. (2015).

Source: Altostratus Inc.

Three current-climate meteorological states were simulated: (1) a reference state, based on often-used standard modeling approaches and configurations in WRF, excluding any urban parameterizations, (2) a standard urbanized modeling approach, that is, standard WRF-urban, typically used by urban climate modelers, and (3) study-specific customized uWRF meteorology for comparison with the reference state and evaluation of improvements in model performance relative to the standard WRF-urban. For the reference state, some of the more common options the model was configured with include (all these are explained in the WRF model documentations):

- Kain-Fritsch cumulus parameterizations
- MYJ PBL scheme with prognostic TKE
- Nonurban physics
- NOAH LSM surface physics, prognostic soil temperature and moisture
- RRTM longwave radiation transfer scheme, multiple bands, trace gases
- Dudhia shortwave physics, downward integration, clouds, scattering, clear-sky
- Smagorinsky horizontal diffusion K diagnosed from 3D deformation of the wind field
- WSM3 microphysics cloud water and rain

For study-specific uWRF (number 3, above), the following additional options were used:

- Urban physics: AREAMOD, mod-UCM, mod-BEP (Altostratus Inc. modified approaches)
- Altostratus Inc. urban schemes trigger and meshing with nonurban cell components
- BouLac/MYJ PBL schemes
- Updated NOAH LSM parameters
- Bottom-up and improved LULC and morphology characterization/model input, Level-IV, NLCD, NUDAPT-based characterizations (as discussed above)
- Future-climate downscaling via uWRF (years and RCP combinations); fine-resolution dynamical downscaling
- LUCAS future land-use and land-cover projections, as discussed above

For a discussion of these various options and configurations, the reader is referred to Taha (2017), Taha and Freed (2015), and Taha et al. (2018). Figure 7 shows the nested-grid model configuration used in this project. The study-modified urbanized WRF model (uWRF) was applied at the innermost, finest-resolution four grids, that is 2-km and 500-m resolutions, corresponding (from north to south) to the San Francisco Bay Area, Fresno, Bakersfield, and the Los Angeles region. In this report, most of the discussion focuses on the San Francisco and Los Angeles regions. The geographical extent of the innermost grids for the Los Angeles and San Francisco Bay Area domains were shown earlier in Figure 2. Figure 8 is an example from the WRF output for the reference-state meteorology, depicting the simulated air temperature at 2 m AGL.

Figure 7: Weather Research and Forecasting and Urbanized Weather Research and Forecasting Modeling Grids Applied in Study

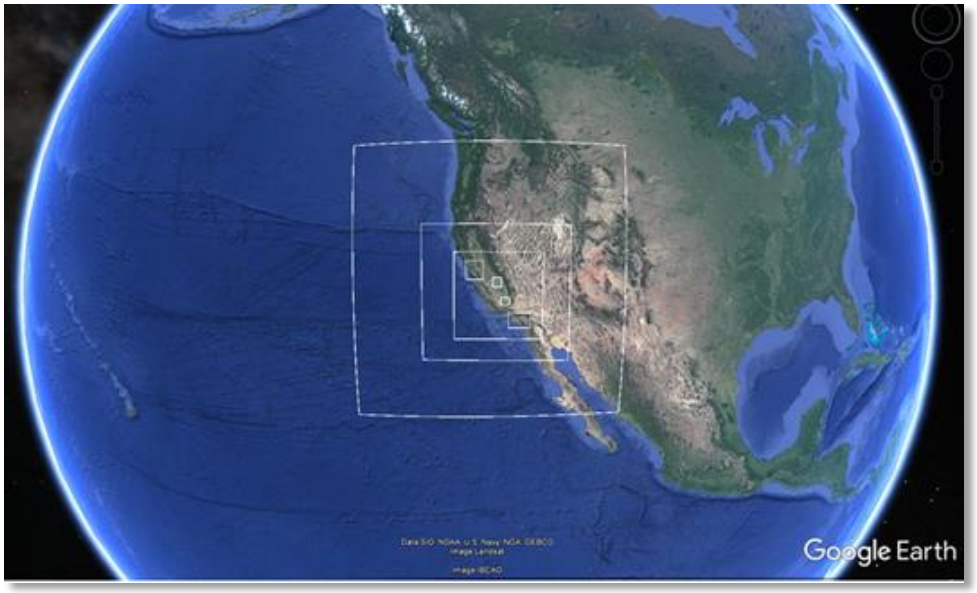

Horizontal grid resolutions are: 54, 18, 6, 2, and 0.5 km (the latter not shown in the figure).

Source: Altostratus Inc.

Figure 8: Weather Research and Forecasting Model Reference-State Simulation-Result Examples

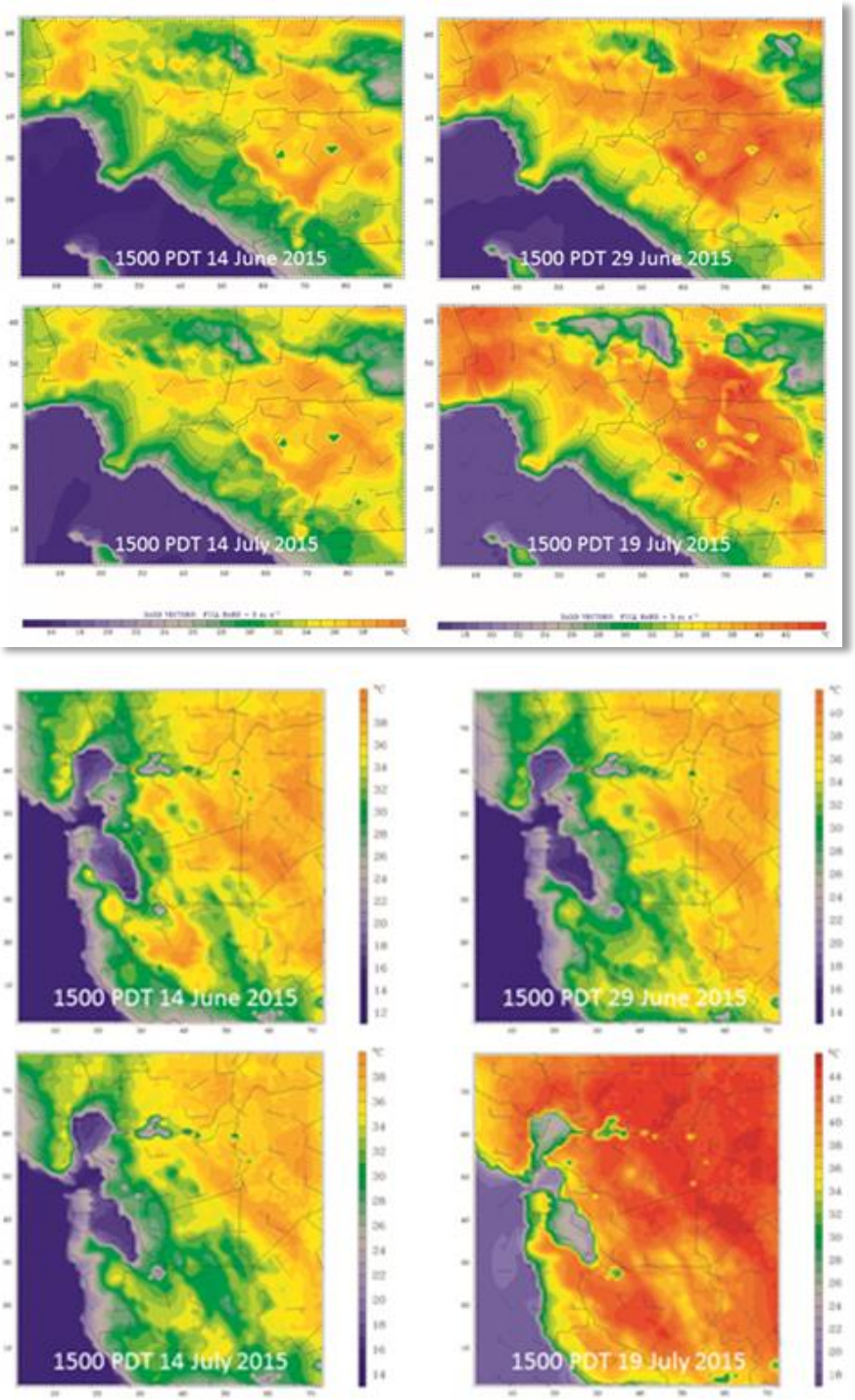

Examples are for the 2-km grid for four sample 1500 PDT periods in June and July 2015 representing 2-m air temperature for the Los Angeles region (*top*) and the San Francisco Bay Area (*bottom*).

Source: Altostratus Inc.

The simulations were carried out with an overlapping scheme where 17 days at a time were simulated (and the first two, spin-up days discarded), then another overlapping 17 days were simulated (overlapping with the last two days of the preceding interval), and the two first spin-

up days discarded, and marching on until reaching the end of the summer season being modeled. The reasons for splitting the simulations into overlapping intervals were to:

- Provide an ensemble of model runs as the basis for developing probabilistic correlations and error estimates (deviations from ensemble means) for each region (ensembles are across years, months, and weeks). This was equivalent to running the meteorological model with a set of perturbed (varying) initial conditions to provide ensembles for a probabilistic forecast.
- Provide successive correction of the simulations toward reanalysis.
- Take into consideration that two weeks (~15 days) is also generally the accepted limit for deterministic predictability (deterministic forecasting limits), that is, a two-week period is the optimum length to minimize the growth of errors from initial conditions (typically occurring in longer runs).
- Capture upper-air signals (from reanalysis and observational data) that did not exist or were lost during model integration (if relying solely on a single set of initial conditions), hence the necessity to re-initialize the model so as to recapture those upper air signals.
- Model performance that was found to be better with overlapping runs than long runs with cold starts.

CHAPTER 3:
Project Results

3.1 Observational Characterizations

Station-by-station analysis was undertaken for each study domain (up to ~330 stations or more in the Los Angeles region and up to ~245 stations or more in the San Francisco Bay Area, depending on reporting), including computing cumulative metrics, degree-hours (DH) or degree-hours per day (DH/day) at each monitor, with or without thresholds, as well as stations maxima, minima, and other metrics (an example from this analysis is shown in Figures 1.A through 1.L in Appendix C). In addition, domain-wide characterizations of the observations were also carried out, including a statistical evaluation of the distributions of the DH/day metric over the mesonet networks in the study areas. (Figures 2.A through 2.I, in Appendix C, are examples.)

The interquartile ranges (IQR) corresponding to the observational data analyzed in this task (and shown in Figures 1 and 2 of Appendix C) are summarized in Table 1. The IQR are used here as an indicator to the spread in DH/day values over each of the study regions. The DH/day quartiles were also used as one of several bases in developing temperature zones and spatial analysis discussed later in this report.

Table 1: Means and Interquartile Ranges of Degree Hours/Day in Study Areas

Mo./Yr.	Fresno-Bakersfield Region		Los Angeles Region		San Francisco Bay Area	
	Mean	IQR	Mean	IQR	Mean	IQR
6-2013	616	34	488	67	432	84
7-2013	700	46	536	76	445	125
8-2013	636	41	539	84	441	74
9-2013	559	40	534	71	440	41
6-2014	613	35	485	55	430	85
7-2014	687	44	558	65	472	103
8-2014	653	52	552	69	456	77
9-2014	609	36	565	63	455	54
6-2015	638	42	510	70	442	88
7-2015	648	37	524	61	472	71
8-2015	646	32	579	64	484	56
9-2015	592	38	570	45	481	47

DH/day (°C·hr/day); non-threshold DH/day metric.

Source: Altostratus Inc.

The following observations were made:

- The regional differences in climate, as expected, are evident from the mean values showing the Fresno-Bakersfield region as warmest (means in the 600s °C·hr/day or 1800s °F·hr/day), the Los Angeles region as second (means in the 500s °C·hr/day or 1600s °F·hr/day), and the San Francisco Bay Area as the cooler of the three regions (means in the 400s °C·hr/day or 1400s °F·hr/day).
- The IQR, on the other hand, showed a reverse order in general, with the Fresno-Bakersfield region having the smallest IQR (30s and 40s°C·hr/day), the Los Angeles region coming in second, with IQRs mostly in the 60s and 70s °C·hr/day, and the San Francisco Bay Area with the largest IQR, but also with considerable variability. The explanation rested in the characteristics of the geographical locations: the Fresno-Bakersfield region is inland and relatively uniform across the domain, and hence has a smaller IQR. The Los Angeles region is a vast expanse from coastal areas to inland deserts (urban climate archipelago) and, as such, has a higher IQR. Finally, the San Francisco Bay Area, another large urban climate archipelago, has the most variability in intraurban weather as it ranges from colder coastal areas, milder bay areas, to inland regions in the central valley, hence the larger IQR.
- The spread (IQR) changed in smaller levels in both the Fresno-Bakersfield and Los Angeles regions compared to the San Francisco Bay Area.
- The variations in the regional weather across the months also differed from one area to another:
- In the Fresno-Bakersfield domain, the DH/day mean increased from June to July, is highest in July, then decreased to August, and then to September (and was consistent across the years). The highest mean was in July.
- In the Los Angeles region, the general order was an increase from June to July to August, peaking in August, and then decreasing in September. The highest mean was in August (although it was different in 2014 when the peak month was September).
- In the San Francisco Bay Area, the order was such that the mean DH/day increased from June to July (peaked in July), then came down in August and September. However, there was practically no difference between the months of August and September in terms of the means in the Bay Area—and in 2015, the hottest months were August and September.
- The variations in IQR were more difficult to characterize and there did not seem to be a systematic pattern. However, one feature that stood out was the IQR in the San Francisco Bay Area, which was very large in July and very small in September.

3.1.1 Initial Temperature Zoning (Clustering)

Based on the analysis of observational surface meteorological data, several fine-scale temperature zones and subzones were developed within each of the study regions. Each zone or subzone encompassed a number of mesonet stations and could be represented by (correlated to) one or more spatial surrogates, or *handshake points*. The quartile ranges are summarized in Table 2. This initial temperature and DH/day zoning represented a first-level classification and characterization of intraurban climate variations.

Table 2: Quartiles of Degree-hour Per Day at Mesonet Stations

Region/Date	Min	Q1	Median	Q3	Max
LA 6-2013	361	455	492	522	628
LA 7-2013	428	499	535	575	690
LA 8-2013	383	497	545	581	712
LA 9-2013	312	502	547	573	677
LA 6-2014	343	457	486	513	615
LA 7-2014	428	526	563	591	687
LA 8-2014	346	520	557	589	692
LA 9-2014	341	537	576	600	715
LA 6-2015	403	475	511	546	647
LA 7-2015	377	493	530	555	648
LA 8-2015	459	547	581	611	682
LA 9-2015	378	556	580	602	696
SF 6-2013	293	391	441	475	579
SF 7-2013	295	379	454	504	618
SF 8-2013	334	405	444	479	568
SF 9-2013	341	420	446	462	541
SF 6-2014	296	388	446	473	580
SF 7-2014	342	419	485	523	610
SF 8-2014	353	416	461	493	574
SF 9-2014	367	428	457	483	566
SF 6-2015	309	398	453	487	591
SF 7-2015	365	439	475	510	601
SF 8-2015	372	458	491	514	602
SF 9-2015	359	458	489	506	576

Tables are for all mesonet stations in the study regions (LA: Los Angeles region; SF: San Francisco Bay Area), for 2013 through 2015 and June through September, as identified in the first column. (DH/day in units of °C hr/day).

Source: Altostratus Inc.

3.1.2 Nonthreshold Degree-Hours Analysis

The goal of computing nonthreshold cumulative metrics was to compare, within each region and time period, the relative spatial variations in temperature and derived quantities. Based on the analysis of the temperature field, several fine-scale temperature zones and subzones (clusters) were developed within every study region. Each temperature zone or subzone contained a number of mesonet stations that were correlated to one or more surrogates or handshake points, such as the CEC's climate zone's representative weather stations.

Thus, degree-hour metrics were computed for each monthly period, and average degree-hour per day metrics were derived (DH/day in units of °C·hr/day). Based on the analysis presented in this and the following sections, it was deemed possible, at least semi-quantitatively, to identify *tiers* or levels of temperature zones: (1) the first tier included temperature zones that were persistent across months and years, (2) a second tier included zones that were semi-permanent, but covered major areas in the domain, and (3) a third tier included temperature zones that were inconsistent in terms of signal, that is, they tended to change substantially from one interval to another. In Appendix D, further discussion is provided along with figures.

In the following discussion (and in Figures 1.A through 1.I in Appendix D), the temperature zones are labeled as *z_MMMYY-#L*, where *z* refers to the region, that is, *LA* (for Los Angeles region), *SF* (for San Francisco Bay Area), and *FB* (for Fresno-Bakersfield region), *MMM* is month (JUN, JUL, AUG, or SEP), *YY* is year (13, 14, or 15), *#* is the cluster number within each region and month, that is, first through fifth quantile intervals of the domain and month's temperature range (values for *#* are *1, 2, 3, 4* and *5*) and *L* is a letter indicating noncontiguous similar temperature zones, that is, subzones. Thus, *L* can take on values of *a*, *b*, *c*, *d*, and *e*, each of which identifying a subzone within each temperature zone or cluster. The matrix of possible combinations of clusters and subzones is shown diagrammatically in Figure 9. Note that this matrix was based on the analysis of observational data only; the modeling task (discussed later) will result in more resolved (additional) categories of *#* and *L*.

Figure 9: Temperature Subzones from Observational Data Spatial Analysis

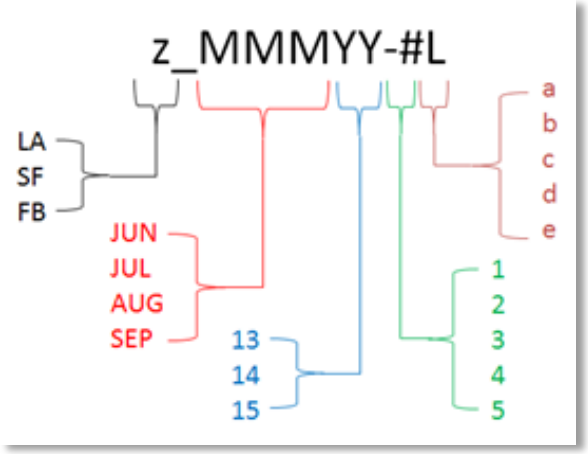

Source: Altostratus Inc.

Because the discussion of each temperature cluster, month, region, and level separately was extremely lengthy and tedious, only the first month of each region (June 2013) is discussed as an example to provide a general idea regarding the clusters, their extents, and geographical representations. The possible combinations of clusters, as defined in Figure 9, are shown in Figures 1.A through 1.I in Appendix D.

Some general observations were made with respect to the month-to-month variations in the temperature zones and subzones in the Los Angeles region and the San Francisco Bay Area:

- Clusters generally retained their characteristic spatial patterns but moved closer to or farther away from the coastline.

- Clusters bundled together and formed more contiguous, larger clusters or could split into a number of subclusters, sometimes forming isolated *islands*.
- In some cases, the clusters covered smaller or larger areas even as they retained their general spatial patterns; for example, the coastal cluster (band) became wider or narrower, or completely disappeared in some cases.
- The urban-climate archipelago effects and on-shore warming signals were evident in the spatial patterns of temperature subzones. In the case of Los Angeles region, this was seen as westerly, southwesterly, and southerly gradients in temperature.

To provide a quantitative definition of the clusters' boundaries and ranges (temperature zones), Table 3: Los Angeles Region Cluster Ranges (quantiles of DH/day; °C·hr/day) and Table 4 list the quantiles and intervals for each month and year considered in this analysis.

Table 3: Los Angeles Region Cluster Ranges (quantiles of DH/day; °C·hr/day)

Zone z=LA	DH/day quantiles (year 2013)					
	1st interval z_MMM13_1L	2nd interval z_MMM13_2L	3rd interval z_MMM13_3L	4th interval z_MMM13_4L	5th interval z_MMM13_5L	
z_JUN13_#L	361	449	476	501	528	628
z_JUL13_#L	428	483	521	553	589	690
z_AUG13_#L	383	485	529	559	593	712
z_SEP13_#L	312	486	536	555	579	677

Zone z=LA	DH/day quantiles (year 2014)					
	1st interval z_MMM14_1L	2nd interval z_MMM14_2L	3rd interval z_MMM14_3L	4th interval z_MMM14_4L	5th interval z_MMM14_5L	
z_JUN14_#L	343	449	474	499	520	615
z_JUL14_#L	428	520	545	571	600	687
z_AUG14_#L	346	512	548	568	594	692
z_SEP14_#L	341	526	568	586	604	715

Zone z=LA	DH/day quantiles (year 2015)					
	1st interval z_MMM15_1L	2nd interval z_MMM15_2L	3rd interval z_MMM15_3L	4th interval z_MMM15_4	5th interval z_MMM15_5L	
z_JUN15_#L	403	462	498	524	553	647
z_JUL15_#L	377	488	517	542	563	648
z_AUG15_#L	459	538	569	593	621	682
z_SEP15_#L	378	548	573	589	606	696

z = Los Angeles region; cluster ranges (quantiles of DH/day; °C·hr/day).

Source: Altostratus Inc.

3.1.3 Threshold-Specific Degree-Hours Analysis

The goal of computing threshold-specific cumulative metrics was to facilitate direct inter-comparisons across various regions as well as various time periods within each region. While any threshold could be used for this purpose, T > 72°F (T > 22.2°C) was selected as an example in this discussion. This represented one of many common temperature thresholds used by the electric utilities as a basis to calculate cooling degree hours. Thus, a cutoff value of 533 DH/day (°C·hr/day) was used in this analysis: 72.0°F × 24 hours = 1728°F·hr/day (22.2°C × 24 hours = 533°C·hr/day).

Figures 1.A through 1.I in Appendix E are provided for this example (the contouring of the threshold is done in reverse color coding, that is, areas with higher than 533 DH/day are

unshaded and those below the threshold are masked). The reason for this *reverse* color coding is to outline the outer boundaries of the observational data-analysis domain, that is the spatial extent of mesonet and metar stations in each study area.

Table 4: San Francisco Bay Area (z=SF) Clusters Ranges (quantiles of DH/day; °C·hr/day)

Zone z=SF	DH/day quantiles (year 2013)					
	1st interval z_MMM13_1L	2nd interval z_MMM13_2L	3rd interval z_MMM13_3L	4th interval z_MMM13_4L	5th interval z_MMM13_5L	
z_JUN13_#L	293	385	421	455	482	779
z_JUL13_#L	295	371	421	475	508	618
z_AUG13_#L	334	392	429	462	482	568
z_SEP13_#L	341	416	432	452	466	541

Zone z=SF	DH/day quantiles (year 2014)					
	1st interval z_MMM14_1L	2nd interval z_MMM14_2L	3rd interval z_MMM14_3L	4th interval z_MMM14_4L	5th interval z_MMM14_5L	
z_JUN14_#L	296	378	417	455	479	580
z_JUL14_#L	342	410	457	499	527	610
z_AUG14_#L	353	407	446	478	498	574
z_SEP14_#L	367	420	443	468	487	566

Zone z=SF	DH/day quantiles (year 2015)					
	1st interval z_MMM15_1L	2nd interval z_MMM15_2L	3rd interval z_MMM15_3L	4th interval z_MMM15_4	5th interval z_MMM15_5L	
z_JUN15_#L	309	380	432	466	490	591
z_JUL15_#L	365	429	462	492	514	601
z_AUG15_#L	372	445	477	499	517	602
z_SEP15_#L	359	452	475	496	513	576

San Francisco Bay Area; cluster ranges (quantiles of DH/day; °C·hr/day).

Source: Altostratus Inc.

Los Angeles Region

For all three years (2013, 2014, and 2015), the geographical area above the threshold started out small in June, increased in size in July and August, and then somewhat decreased again in September. This cyclical pattern was to be expected as it followed the monthly changes in heat, typically peaking in August and beginning to decrease afterward. In June, the areas above the threshold were confined to the east basin (EB) and other parts of the Inland Empire (IE), including Riverside, Moreno Valley, Hemet, and Beaumont. In July, the area over the threshold expanded to additionally include Highland, San Bernardino, Rancho Cucamonga, Fontana, Riverside, Corona, Perris, Lake Elsinore, Murrieta, and Temecula. In some cases, for example, July 2014, this area also merged with parts of the west basin. During July, the area above the threshold also included San Fernando Valley and central parts of the domain, such as Whittier, Norwalk, Fullerton, Anaheim, and Pomona. In the months of August and September, most of the Los Angeles region was above the threshold, except for a coastal band that varied in width from year to year—relatively wider in 2013, narrower in 2014, and very narrow in 2015, indicating the latter being the warmer year of the three in that area. (Refer to figures 1.A through 1.C in Appendix E.)

San Francisco Bay Area

The San Francisco Bay Area is generally below the threshold at all times, except for some small areas in the eastern parts of the domain during certain months. For example, in July 2013, the only areas above the threshold were in the northeastern part of the domain, including the cities of Brentwood, Oakley, Antioch, Pittsburg, and Bay Point. In July 2014, that area expands to also include Byron and the mountains to its south. In August and September 2013, the entire observational analysis domain in the San Francisco Bay Area was below the threshold. In 2014, during the months of June, August, and September there were no areas above the threshold—only in July. These were the same zones as in July 2013, plus a large area covering desert, agriculture, and mountains stretching from east of Livermore/Altamont Pass all the way south to east of Santa Clara Valley. In 2015, all four months had a small area in the northeast of the domain above the threshold. As in July 2013, these areas included Brentwood, Oakley, Antioch, Pittsburg, and Bay Point. Refer to figures 1.D through 1.F in Appendix E.

Of note, an area being under the threshold did not necessarily imply that its temperature never exceeded 72°F (22.2°C). In some cases, this indicated that the exceedance during daytime was offset at night, thus resulting in a sum of less than 533 DH/day. The daytime-high temperatures exceeding 72°F (22.2°C) were evident in Section 3.1.4, (see the values listed in Table 5 and Table 6). Furthermore, the threshold used here is only an example.

3.1.4 Analysis of Temperature Maxima

The purpose of evaluating afternoon conditions was to generally assess the temperature field characteristics near the time of the peak in each region and period, as well as to evaluate whether the geographical locations of these peak temperatures were consistent across years and months. While daytime maximum temperature at any given location can generally occur anytime between 1200 and 1800 local standard time (LST), depending on weather conditions and land-surface properties, in large urban areas, such as the urban climate archipelagos of Los Angeles and San Francisco Bay Area, various zones can peak at different times and, therefore, it may not be very informative to compare them simultaneously for the purpose of this discussion. Thus, a uniform time stamp, for example, 1400 PDT (Pacific Daylight-Saving Time), was used for intraurban comparisons of the peak daytime temperature zones (Appendix F provides Figures 1.A through 1.I and additional information to this discussion).

Los Angeles Region

In the Los Angeles region (Figures 1.A through 1.C in Appendix F), several observations were made based on the analysis of 1400 PDT temperatures. The first was that the on-shore warming tendency was evident (as well as the urban climate archipelago effect) as positive temperature gradient away from the western and southern coasts. Areas with higher than domain-mean temperatures were generally consistent across the months and years, and while there were variations in the spatial patterns from one period to another, four areas (subzones A—D) were relatively consistent with high peak temperatures:

- Subzone A encompassed most of the EB ranging from San Bernardino in the north to Temecula in the south. The boundaries of subzone A varied from one time period to another, but its geographical position was consistent across all months and years considered in this analysis.

- Subzone B represented the most downwind part of the west basin, ending at the Santa Ana Mountains. Although this subzone was relatively small and with low urbanization levels, it nevertheless was consistent in terms of peaking temperatures and was separated from subzone A by the Santa Ana Mountains.
- Subzone C was another consistent area of higher peak temperatures. It comprised (from east to west) the areas of Claremont, Pomona, San Dimas, Glendora, Diamond Bar, Azusa, Irwindale, West Covina, Arcadia, and East Pasadena.
- Subzone D represented mainly the San Fernando Valley and mostly its western part.

In Table 5, the values of the 1400 PDT temperature quantiles and the corresponding intervals are summarized for the Los Angeles region. To provide an idea of the 1400 PDT temperature spread in the domain, an inter-quantile range, IQR (defined for the purpose of this discussion as the difference between the 5th and 2nd quantiles), is computed. Across the three years in Table 5, the IQR for June is 13.5°F, 12.8°F, and 13.7°F (7.5°C, 7.1°C, and 7.6°C), respectively. For the month of July, the IQR is 14.2°F, 12.9°F, and 11.7°F (7.9°C, 7.2°C, and 6.5°C), and for the month of August it is 15.3°F, 13.5°F, and 13.1°F (8.5°C, 7.5°C, and 7.3°C), respectively. For the month of September, the IQR is 12.9°F, 12.6°F, and 10.6°F (7.2°C, 7.0°C, and 5.9°C), respectively.

Table 5: Los Angeles Region Cluster Ranges

Zone z=LA	1400-PDT temperature quantiles (year 2013)					
	1st interval	2nd interval	3rd interval	4th interval	5th interval	
z_JUN13_#L	18.2	22.3	25.5	27.6	29.8	33.9
z_JUL13_#L	19.4	23.6	26.9	29.0	31.5	35.7
z_AUG13_#L	17.9	24.5	28.2	30.6	33.0	36.1
z_SEP13_#L	18.7	24.7	28.2	30.1	31.9	34.7

Zone z=LA	1400-PDT temperature quantiles (year 2014)					
	1st interval	2nd interval	3rd interval	4th interval	5th interval	
z_JUN14_#L	18.8	22.5	25.4	27.3	29.6	33.8
z_JUL14_#L	20.8	25.3	28.2	30.2	32.5	35.9
z_AUG14_#L	19.4	25.0	28.6	30.6	32.5	35.4
z_SEP14_#L	18.6	25.8	29.5	31.3	32.8	36.1

Zone z=LA	1400-PDT temperature quantiles (year 2015)					
	1st interval	2nd interval	3rd interval	4th interval	5th interval	
z_JUN15_#L	18.1	23.0	26.0	27.9	30.6	34.8
z_JUL15_#L	19.3	23.5	26.5	28.3	30.0	33.4
z_AUG15_#L	21.5	26.4	29.2	31.7	33.7	37.1
z_SEP15_#L	19.9	26.4	29.6	31.2	32.3	35.7

Los Angeles region; cluster ranges (quantiles of 1400 hours, Pacific daylight time; temperature in °Celsius.) Also refer to figures 1.A through 1.C in Appendix F.

Source: Altostratus Inc.

San Francisco Bay Area

In the San Francisco Bay Area's urban-climate archipelago (Figures 1.D through 1.F in Appendix F), the on-shore temperature gradients were less obvious than in the Los Angeles region. However, this warming tendency could be detected in the east and south bays as well as in the Santa Clara Valley as shore-parallel temperature gradients. As with the Los Angeles region discussed above, there were some areas of higher than domain-mean temperatures in

the San Francisco Bay Area that were relatively consistent across the months and years examined in this study:

- Subzone A encompassed the north-eastern region of the analysis domain, including the areas of Discovery Bay, Brentwood, Oakley, Antioch, Pittsburg, and Bay Point.
- Subzone B ran roughly in a north-south direction, including (from north to south) the areas of Clayton, Concord, Walnut Creek, Alamo, Diablo, Danville, Black Hawk, San Ramon, Dublin, Pleasanton, and Livermore.
- Subzone C comprised mainly the south and southwestern parts of Santa Clara Valley, including the areas of Cupertino, Saratoga, Campbell, and Cambrian Park, as well as Morgan Hill, farther to the south.
- Subzone D was a relatively smaller area to the west of Santa Clara Valley including the cities of Palo Alto, Mountain View, Los Altos, and parts of Sunnyvale.

In Table 6, the 1400 PDT temperature quantiles and corresponding intervals are summarized. As was done above, an inter-quantile range, IQR (defined for the purpose of this discussion as the difference between the 5th and 2nd quantiles) is computed. Across the years 2013, 2014, and 2015, the IQR for June is 13.1°F, 13.1°F, and 13.5°F (7.3°C, 7.3°C, and 7.5°C), respectively. For the month of July, the IQR is 16.7°F, 14.4°F, and 11.8°F (9.3°C, 8.0°C, and 6.6°C), respectively. In August, the IQR is 11.7°F, 13.6°F, and 10.6°F (6.5°C, 7.6°C, and 5.9°C), and for September, it is 7.7°F, 10.9°F, and 9.1°F (4.3°C, 6.1°C, and 5.1°C), respectively.

Table 6: San Francisco Bay Area Cluster Ranges

Zone z=SF	1400-PDT temperature quantiles (year 2013)					
	1st interval	2nd interval	3rd interval	4th interval	5th interval	
z_JUN13_#L	14.0	20.3	22.6	25.7	27.6	30.8
z_JUL13_#L	13.8	20.0	23.0	26.7	29.3	32.9
z_AUG13_#L	15.6	21.3	23.7	26.0	27.8	34.4
z_SEP13_#L	16.2	22.3	23.8	25.2	26.6	36.1

Zone z=SF	1400-PDT temperature quantiles (year 2014)					
	1st interval	2nd interval	3rd interval	4th interval	5th interval	
z_JUN14_#L	13.7	20.7	23.7	26.3	28.0	31.8
z_JUL14_#L	15.8	21.6	24.9	27.6	29.6	33.2
z_AUG14_#L	16.4	20.9	24.2	26.9	28.5	32.2
z_SEP14_#L	17.7	21.7	24.4	26.0	27.8	31.2

Zone z=SF	1400-PDT temperature quantiles (year 2015)					
	1st interval	2nd interval	3rd interval	4th interval	5th interval	
z_JUN15_#L	14.3	20.8	24.2	26.5	28.3	33.1
z_JUL15_#L	16.9	21.7	24.6	26.9	28.3	32.7
z_AUG15_#L	17.7	23.3	25.9	27.6	29.2	32.8
z_SEP15_#L	17.3	23.7	25.9	27.4	28.8	31.4

San Francisco Bay Area; cluster ranges (quantiles of 1400 hours, Pacific daylight time; temperature in °Celsius.) Also refer to figures 1.D through 1.F in Appendix F.

Source: Altostratus Inc.

3.1.5 Analysis of Temperature Minima

The goal of evaluating 0200 PDT temperatures was to assess the characteristics around the times of the lows in each region and period and evaluate whether the geographical locations of the minima were consistent across years and months. The lowest diurnal temperatures, depending on land use and land physical properties and local climate, typically occur just before sunrise. Here, 0200 PDT was selected for discussion as a uniform time interval across all domains and periods for the sake of direct inter-comparability and also because it was a time when there still may have been activity.

Figures 1.A through 1.I in Appendix G provide additional information, where, in each figure, the following information is shown:

- Mesonet stations are depicted with small circles representing 0200 PDT air temperature averaged for the month.
- Metar stations are shown with triangles and represent the 0200 PDT average air temperature for the month at those locations.
- Mesonet stations clusters (temperature zones and subzones) based on the six quantiles (five intervals) of average 0200 PDT air temperature for the given month.

Los Angeles Region

In the Los Angeles region, several observations were made based on examination of the 0200 PDT temperature field. The on-shore warming tendency was much less detectable at night, relative to daytime/peak temperature hours (Section 3.1.4), or was completely nonexistent. The temperature field at 0200 PDT was disorganized relative to that during the daytime. While zones A, B, C, and D of 1400 PDT air temperatures (Section 3.1.4) were still identifiable at 0200 PDT, there were many more areas throughout the domain with 0200 PDT high temperatures.

In particular, the west basin and coastal areas were as warm as other areas in the Los Angeles region at this hour. For example, an area in the west basin stretching from downtown Los Angeles all the way south to Anaheim, Orange, and Santa Ana, was as warm (at 0200 PDT) as subzones A—D and sometimes even warmer. Thus, while the daytime on-shore gradient in temperature toward inland locations near the foothills and the EB was evident, the nighttime distribution of 0200 PDT temperature was relatively more uniform throughout the Los Angeles region. Thus, while subzones A—D appeared to consistently have higher temperatures whether during daytime or nighttime, the west basin saw high temperatures only during night hours (relative to other parts of the region).

In Table 7, the values of the 0200 PDT temperature quantiles and the corresponding intervals are summarized for the Los Angeles region. To provide an idea of the spread of 0200 PDT temperature across the domain during different time intervals, an inter-quantile range, IQR (defined here as the difference between the 5th and 2nd quantiles), is discussed. Across the three years listed in Table 7, the IQR is 3.6°F, 4.3°F, and 3.2°F for June (2.0°C, 2.4°C, and 1.8°C), respectively. For July, the IQR is 3.9°F, 3.4°F, and 3.9°F (2.2°C, 1.9°C, and 2.2°C), and for August it is 3.9°F, 3.2°F, and 3.4°F (2.2°C, 1.8°C, and 1.9°C). For September, the IQR is 3.9°F, 3.6°F, and 3.7°F (2.2°C, 2.0°C and 2.1°C), respectively. As expected, the IQR ranges

are much smaller (one fourth to one third) during the nighttime than during the day, such as at 1400 PDT, indicating more uniform temperatures at night.

Table 7: Los Angeles Region Cluster Ranges

Zone z=LA	0200-PDT temperature quantiles (year 2013)					
	1st interval	2nd interval	3rd interval	4th interval	5th interval	
z_JUN13_#L	10.2	15.2	15.9	16.7	17.2	23.6
z_JUL13_#L	13.3	17.3	17.9	18.6	19.5	22.3
z_AUG13_#L	12.8	17.0	17.5	18.3	19.2	23.5
z_SEP13_#L	9.6	17.0	17.8	18.3	19.2	22.3

Zone z=LA	0200-PDT temperature quantiles (year 2014)					
	1st interval	2nd interval	3rd interval	4th interval	5th interval	
z_JUN14_#L	8.6	14.7	15.5	16.2	17.1	19.8
z_JUL14_#L	13.0	18.1	18.9	19.4	20.0	22.6
z_AUG14_#L	10.7	17.9	18.6	19.1	19.7	22.2
z_SEP14_#L	10.0	18.5	19.3	19.9	20.5	22.8

Zone z=LA	0200-PDT temperature quantiles (year 2015)					
	1st interval	2nd interval	3rd interval	4th interval	5th interval	
z_JUN15_#L	8.1	16.1	16.9	17.4	17.9	20.8
z_JUL15_#L	10.0	17.3	18.1	18.9	19.5	22.5
z_AUG15_#L	12.7	18.9	19.6	20.2	20.8	24.9
z_SEP15_#L	9.9	19.0	19.8	20.5	21.1	23.5

Los Angeles region; cluster ranges (quantiles of 0200 hours, Pacific daylight time; temperature in °Celsius.) Also refer to figures 1.A through 1.C in Appendix G.

Source: Altostratus Inc.

San Francisco Bay Area

In the San Francisco Bay Area, the following observations were made:

- Subzones A and C were relatively still persistent, relative to daytime positions, while subzones B and D either no longer existed or were different in spatial extent (compare with figures in Appendix F).
- Subzone A was larger in coverage than during daytime, extending south to the hills east of Fremont, Milpitas, and San Jose. In addition, a new area of high 0200 PDT temperatures emerged over the cities of Fremont and Milpitas. Here, a caveat mentioned earlier is recalled relating to lack of observations over the mountains and, thus, that the temperature zones in these areas could be fictitious.
- Subzone C was unchanged in position relative to the daytime peaks (1400 PDT), however, the spatial pattern was observed to change from one period to another.

Table 8 summarizes the values of the 0200 PDT temperature quantiles and corresponding intervals for the San Francisco Bay Area. The spread of 0200 PDT air temperature across the domain during different time intervals is evaluated with an inter-quantile range, IQR (again, defined for the purpose of this discussion as the difference between the 5th and 2nd quantiles). Across the three years in Table 8, the IQR for June is 3.9°F, 4.3°F, and 4.5°F (2.2°C, 2.4°C, and 2.5°C), respectively. For July, it is 5.2°F, 4.6°F, and 3.6°F (2.9°C, 2.6°C, and 2.0°C), respectively. For the month of August, the IQR is 3.7°F, 3.4°F, and 3.2°F (2.1°C, 1.9°C, and 1.8°C), and for September, it is 3.9°F, 3.7°F, and 3.9°F (2.2°C, 2.1°C, and 2.2°C),

respectively. As expected, and mentioned earlier, the IQR ranges are much smaller (about one third) during the nighttime than during the day.

Table 8: San Francisco Bay Area Cluster Ranges

Zone z=SF	0200-PDT temperature quantiles (year 2013)					
	1st interval	2nd interval	3rd interval	4th interval	5th interval	
z_JUN13_#L	10.2	12.7	13.5	14.2	14.9	18.6
z_JUL13_#L	11.0	12.9	13.9	14.8	15.8	22.0
z_AUG13_#L	11.3	13.8	14.6	15.2	15.9	18.4
z_SEP13_#L	11.6	13.8	14.5	15.0	16.0	18.4

Zone z=SF	0200-PDT temperature quantiles (year 2014)					
	1st interval	2nd interval	3rd interval	4th interval	5th interval	
z_JUN14_#L	9.8	12.0	12.9	13.6	14.4	18.4
z_JUL14_#L	12.3	14.4	15.3	16.0	17.0	22.2
z_AUG14_#L	12.3	14.4	15.2	15.7	16.3	20.7
z_SEP14_#L	12.2	14.6	15.2	15.9	16.7	19.0

Zone z=SF	0200-PDT temperature quantiles (year 2015)					
	1st interval	2nd interval	3rd interval	4th interval	5th interval	
z_JUN15_#L	10.5	12.8	13.8	14.5	15.3	18.6
z_JUL15_#L	12.7	15.0	15.8	16.4	17.0	19.7
z_AUG15_#L	11.7	15.4	16.1	16.6	17.2	20.0
z_SEP15_#L	11.8	14.6	15.3	16.0	16.8	19.8

San Francisco Bay Area; cluster ranges (quantiles of 0200 hours, Pacific daylight time; temperature in °Celsius.) Also refer to figures 1.D through 1.F in Appendix G.

Source: Altostratus Inc.

3.1.6 Development of Observational Characteristic Months and Coarse-scale Temperature Zones

Based on the identification of persistent, semi-persistent, and inconsistent tiers or levels of temperature zones, as discussed in Sections 3.1.2 – 3.1.5, a final product from the observational data analysis in this project, based on clustering the temperature tiers, was the development of characteristics or synthetic months that included probabilistic temperature zones. This product was based on the nonthreshold DH/day metric that was defined earlier. The objective was to create a representative month for each of June, July, August, and September (JJAS) based on the three years analyzed. In other words, the product is a characteristic or synthetic June, July, August, and September for each region based on the observations from years 2013—2015.

Arriving at a characteristic month for temperature in each study region consisted of the following three steps (A, B, and C):

(A) First, a logical (Boolean) union of each temperature subzone from each month was formed via spatial analysis with GIS tools. Thus, unlike the temperature zones discussed in Section 3.1.2 (and shown in Figures 1.A through 1.I in Appendix D) that were month-specific and spatially consistent in terms of boundaries of DH/day quantile intervals, an inclusive union of each temperature subzone in each month (across the years) was developed here. For example, subzones LA_JUN13-5a in Appendix D (seen in Figure 1.A, top left graph), LA_JUN14-5a (seen in Figure 1.B, top left graph), and LA_JUN15-5a (seen in Figure 1.C, top left graph) were combined (Boolean union, $\cup$) to produce a new

inclusive subzone at that geographical location (in this example, this was in the eastern basin of the Los Angeles region). Thus, the resulting new *inclusive subzone* in this example was:

$$(\text{LA\_JUN13-5a}) \cup (\text{LA\_JUN14-5a}) \cup (\text{LA\_JUN15-5a}) \quad (1)$$

(B) Second, a logical (Boolean) intersection ($\cap$) within each of the inclusive subzones resulting from step A above was done as follows: a) an area resulting from the intersection of all three subzones (one subzone per month from each year) was first defined to which b) are added the intersections of any two subzones outside of that area. Steps a and b (pattern recognition) resulted in a new characteristic subzone. Thus, in this example, the characteristic subzone was defined as the total area of the following combinations (i, or ii, or iii) depending on which of the subzones actually overlapped in each direction around the central intersection subzone:

$$[(\text{LA\_JUN13-5a}) \cap (\text{LA\_JUN14-5a}) \cap (\text{LA\_JUN15-5a})] + [(\text{LA\_JUN13-5a}) \cap (\text{LA\_JUN14-5a})] \quad (2)$$

$$[(\text{LA\_JUN13-5a}) \cap (\text{LA\_JUN14-5a}) \cap (\text{LA\_JUN15-5a})] + [(\text{LA\_JUN14-5a}) \cap (\text{LA\_JUN15-5a})] \quad (3)$$

$$[(\text{LA\_JUN13-5a}) \cap (\text{LA\_JUN14-5a}) \cap (\text{LA\_JUN15-5a})] + [(\text{LA\_JUN13-5a}) \cap (\text{LA\_JUN15-5a})] \quad (4)$$

The union and intersection processes (discussed above) to generate a characteristic subzone via pattern recognition are explained schematically in Figure 10, using three hypothetical subzones A, B, and C. In this figure, the inclusive subzone is delineated with the black dashed line and the characteristic subzone is delineated with the dashed brown line.

Figure 10: Development of Characteristic Temperature Subzone

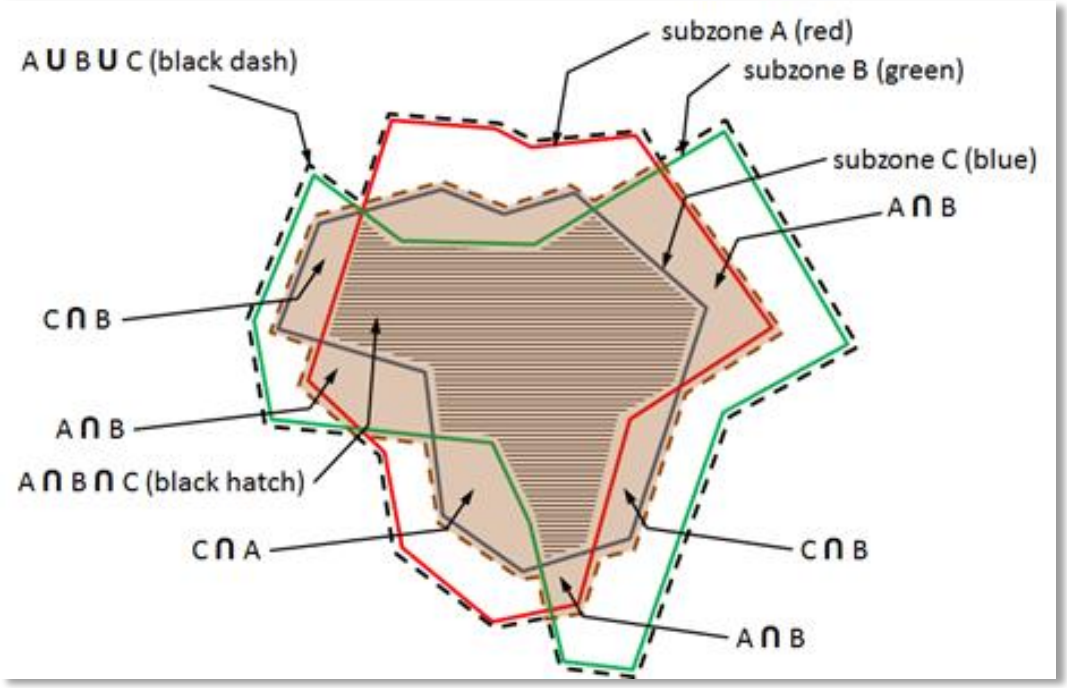

Figure depicts subzones for each month across three years.

Source: Altostratus Inc.

Thus, in this example, the desired characteristic subzone is shown in brown (including both the brown hatch area and nonhatch brown area) and also delineated with the dashed brown line. It is defined as:

$$[A \cap B \cap C] + A \cap B + C \cap B + A \cap B + C \cap A + A \cap B + C \cap B + A \cap C \quad (5)$$

The first term (in brackets) represents the hatched area (in Figure 10), which is the equivalent of what was defined earlier as a *persistent* or *permanent* tier (in Section 3.1.2), and the remaining terms of Equation 5 represent the individual brown-colored parcels surrounding the hatched area (in this example, clockwise from top right). The repetitions of some terms in Equation 5 occur because there were cases with more than one overlap area between any two of the three subzones A, B, and C. Thus, the final areas (characteristic subzones) used in producing the synthetic or characteristic months were the areas denoted by the entire brown background and outlined by the dashed brown line. This process was repeated for all subzones in all regions and all months.

Thus, the characteristic subzone resulting from the above example (Equations 2, 3, and 4) was *LA_jun_i5_a* seen in the eastern part of the domain in Figure 1.1 in Appendix H. The resulting characteristic subzones for all the study regions and the months of June, July, August, and September are shown in Figures 1. through 1.40 in Appendix H. The temperature subzones in these figures are labeled *zz_MMM_i#_L*, where *zz*, *MMM*, *#*, and *L* are as defined earlier in Section 3.1.2 (this analysis was not undertaken for the Fresno-Bakersfield region because of the sparse network of monitors.

(C) The final step involved superimposing all of the characteristic temperature subzones and meshing them together in a mosaic to produce the synthetic, month-representative

temperature zones. Thus, the product of this step was a characteristic month for each of June, July, August, and September, for each region, and over the span of the three years examined in this analysis. This is shown in Figures 11.A through 11.H, below, for the Los Angeles region and the San Francisco Bay Area. The color-coded dots in these figures were intentionally staggered to allow for visually discerning the overlap among the characteristic subzones in each month. The reason why overlap exists is because each temperature zone was calculated probabilistically from a different set of three months (not as single consistent months such as done earlier in Section 3.1.2 and shown in Figures 1.A through 1.I in Appendix D).

In the context of this analysis, a synthetic month represents a probabilistic characterization of that month and its intraurban temperature field. Thus, Figure 11 shows five quantiles of degree-hours (DH) for each synthetic month, that is the clustering of temperature zones in the Los Angeles and San Francisco Bay Area regions based on observational data from metar and mesonet stations networks. The stations shown as black triangles on each figure were a small subset from the observation networks for use in solar radiation and cloud-cover characterizations to evaluate overcast conditions in coastal and inland areas. Accumulated solar radiation, as will be discussed later, was computed at each of these stations and used in the development of correlations.

While there were dominant and persistent features in the spatial patterns in both regions (as seen in Figure 11), and the general spatial features were relatively unchanged from one month to another, some observations were made as follows. It is to be noted here that the DH scales are not similar across the figures and that the figures were meant to show relative, not absolute spatial patterns of temperature; for example, whereas the red color indicated the warmest quantile (fifth interval) in all months, the absolute temperature within this zone differed from one month to another). The same also applied to all other quantiles.

Los Angeles domain (Figures 11.A through 11.D):

- Variations occurred in the coastal zones 1 and 2 (white and blue dots) relative to one another, such that in July, zone 1 (white) was at its widest, and zone 2 (blue) at its narrowest (indicating a large temperature gradient near the coastline), although in September, zone 1 was nearly nonexistent and zone 2 as at its widest extent (indicating smaller temperature gradients near the coast and the penetration of a relatively more uniform air mass farther onshore in September).
- Zone 3 (green) was relatively unchanged in extent throughout the four months, although its boundaries and shapes changed from one month to another.
- Zone 4 (yellow) was smallest (narrowest transition zone) in June, indicating a sharper transition in the climate between the west and east basins, but became wider in August and September, thus suggesting a milder (smaller gradient) transition from the west basin to the eastern one.
- Zone 5 (red) in the IE was large and relatively unchanged in June through August, but became relatively smaller in September.

Figure 11(A-D): Current-Climate, Observations-Based Coarse-Level Intraurban Variability in Temperature – Los Angeles Region

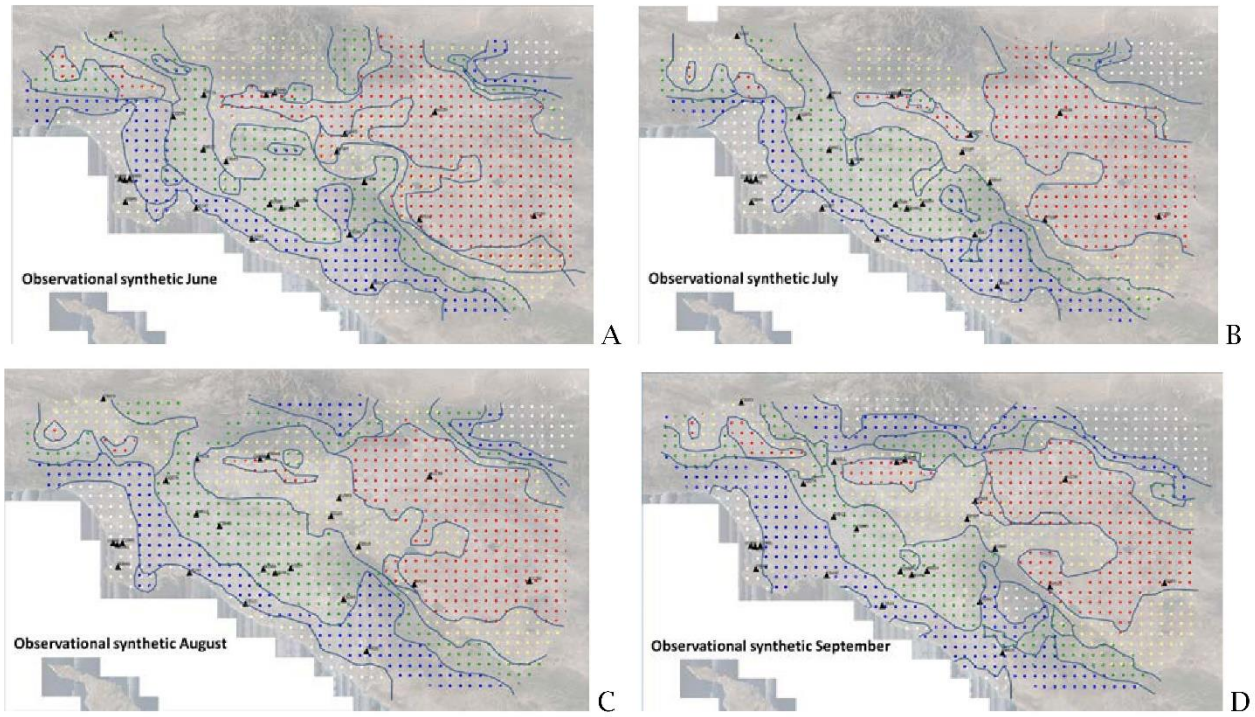

Observational DH/temperature zones: Synthetic June (A), July (B), August (C), and September (D) in the Los Angeles region. Quantiles from coolest to warmest: white, blue, green, yellow, and red.

San Francisco Bay Area (Figures 12.A through 12.D):

- In general, there was less month-to-month variation in the spatial patterns of temperature zones in the San Francisco Bay Area relative to those in the Los Angeles region.
- Some month-to-month variations could be seen in the East Bay (especially in the area from Richmond to San Leandro) in terms of the relative spatial extent of zones 1 and 2 (white and blue dots).
- There were some changes near the southwestern part of the domain, but did not occur in urban areas.
- Zone 3 (green) was relatively unchanged through the months, except for a notable difference in August (Figure 11.G) where this zone extended to the southeast along the eastern hills in San Jose.
- Similarly, zone 4 (yellow) was relatively unchanged except for August when it is at its narrowest.

Figure 12 (A-D): Current-Climate, Observations-Based Coarse-Level Intraurban Variability in Temperature – San Francisco Bay Area

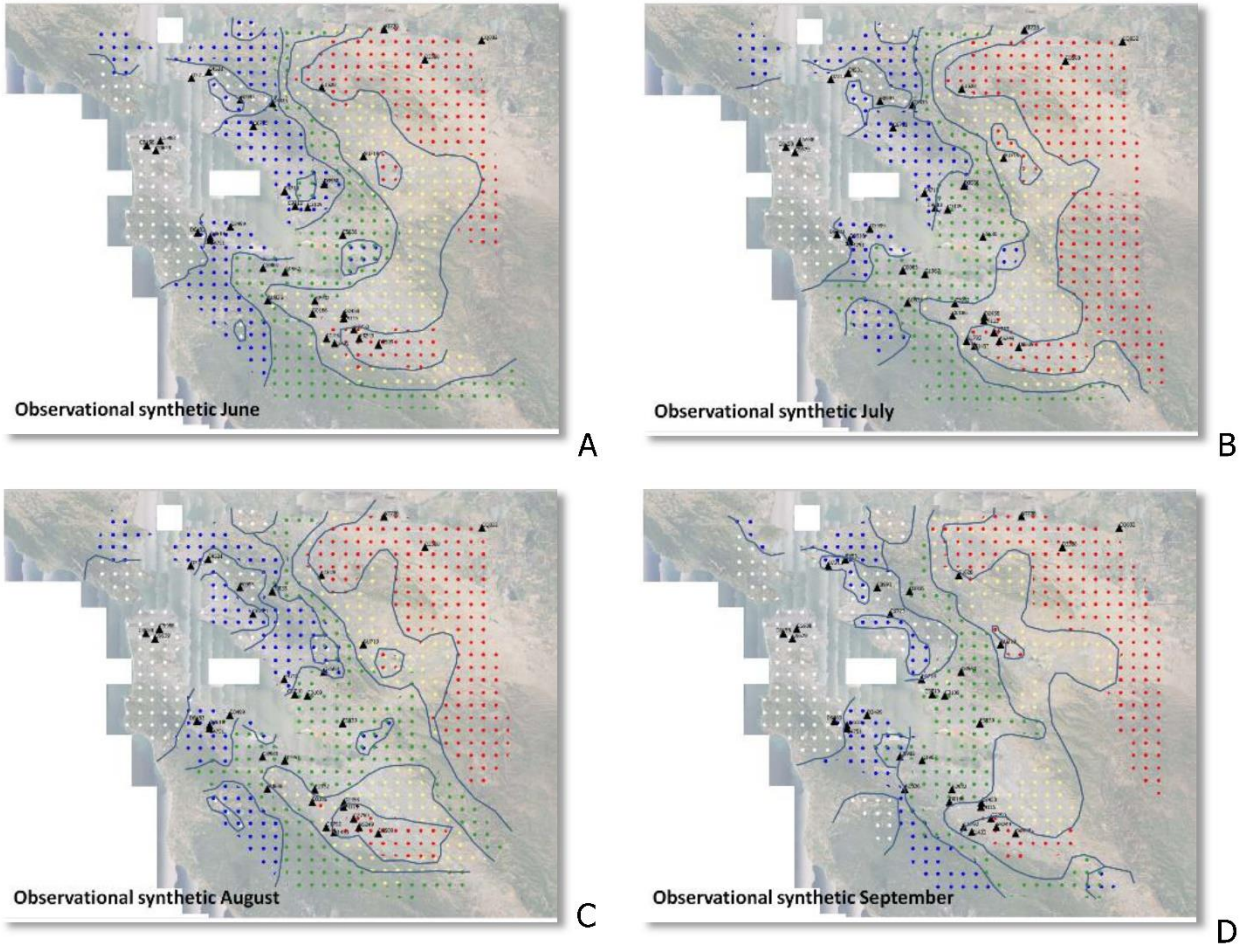

Observational degree hours/temperature zones: Synthetic June (A), July (B), August (C), and September (D) in the San Francisco Bay Area. Quantiles from coolest to warmest: white, blue, green, yellow, and red.

Source: Altostratus Inc.

3.2 Modeling Results and Characterizations

3.2.1 Current Climate

Atmospheric modeling with the study-modified uWRF was undertaken to evaluate intraurban variations in microclimate. Figure 13 provides a random example snapshot from the analysis of model results for current climate (2013—2015) for the Los Angeles and San Francisco Bay Area regions (Figures 17.1 through 17.36 in Appendix B provide a complete set of results and additional information for other hours).

The example in Figure 13, below, represents degree-hour (DH) totals for all hours in the given intervals (in units of °C·hr), that is, total degree-hours over 15 days of 24 hours in each given interval. The graphs are plotted with 500 DH spacing relative to a reference value of 1000 DH. The range is 1000 to 12000 DH.

Figure 13: Model Results Snapshot for Current Climate for the Los Angeles Region and San Francisco Bay Area

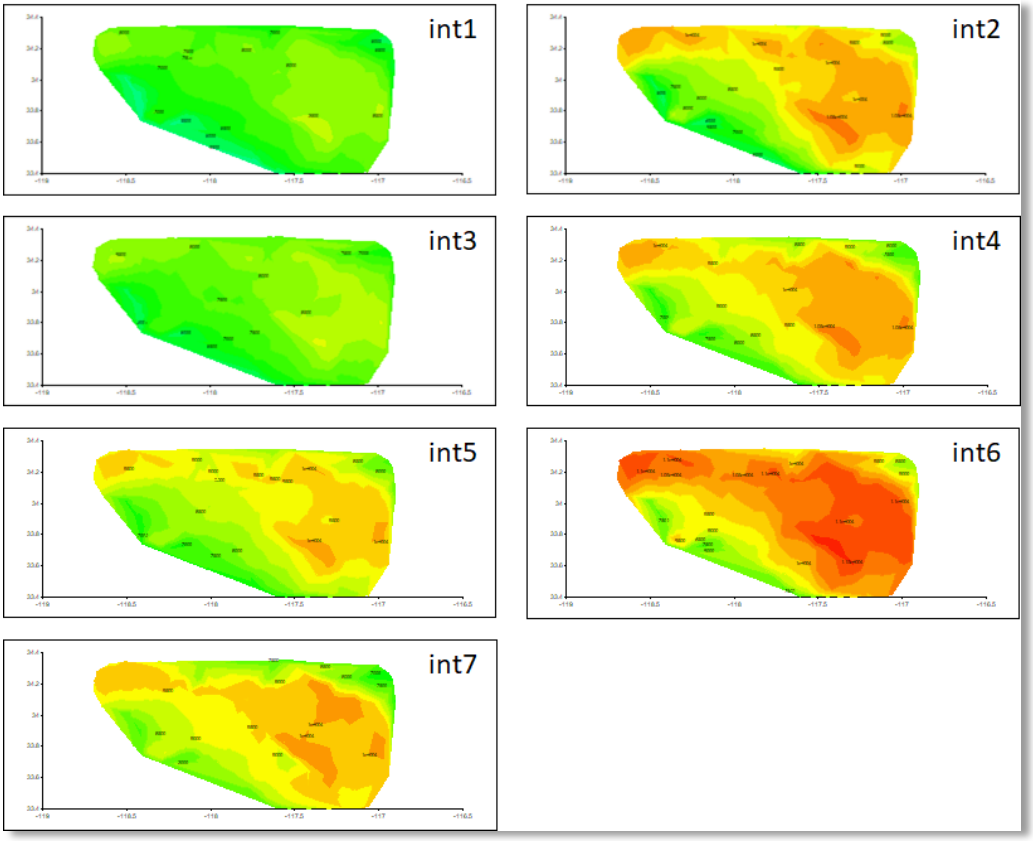

Intervals 1—7, 2015, Los Angeles region, DH total, all hours per 15 days, based on 2-m air temperature, uWRF/modUCM, 500 DH spacing relative to a reference value of 1000 DH. Range 1000 to 12000 DH (ºC·hr).

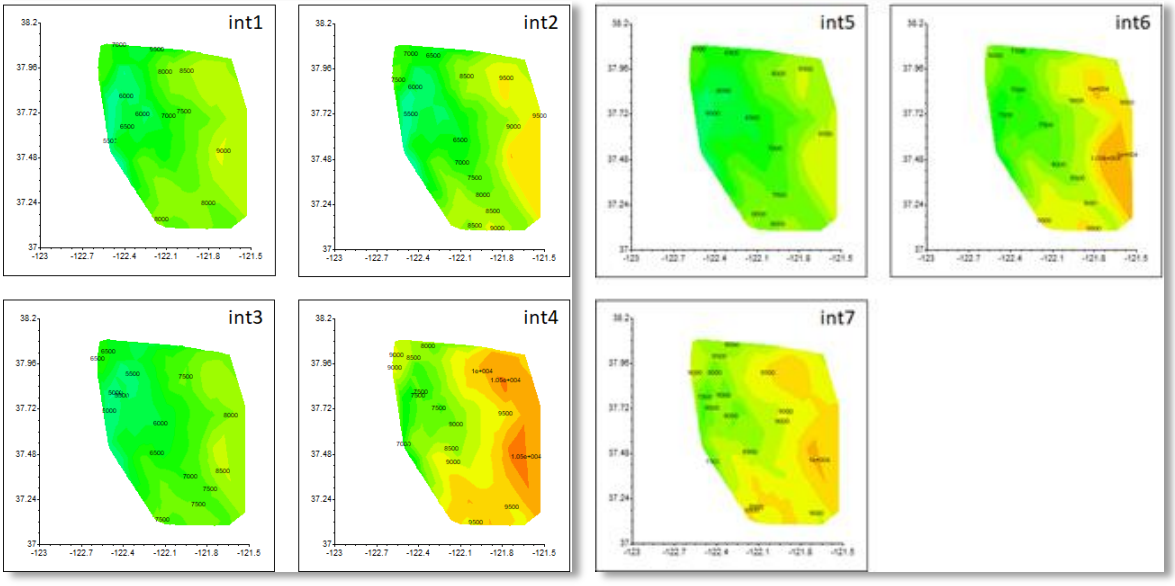

Intervals 1—7, 2015, San Francisco Bay Area, DH total, all hours per 15 days, based on 2-m air temperature, uWRF/modUCM2, 500 DH spacing relative to a reference value of 1000 DH. Range 1000 to 12000 DH (ºC·hr).

Source: Altostratus Inc.

3.2.2 Improved Model Performance

One of the objectives in this project was to improve meteorological-model performance by applying study-modified and recent improvements in urban parameterizations and representations in the atmospheric and land-surface modules of the urbanized WRF modeling system. The goal was to reduce errors in current and future weather forecasts for the electric system as well as to develop finer-scale and more accurate intraurban climate zones. As discussed in the introduction to this report, an error of 1.8°F (1°C) is equivalent to ~500—1,000 megawatts (MW) of generation, systemwide, in the California Independent System Operator service territory (CAISO 2007; Davis et al. 2004; Herter et al 2005). Thus, even small, sub-degree improvements in the forecast can translate into considerable savings in generation, namely, more accurate allocation of resources.

Modifications were carried out in this study to further improve model performance beyond the current capabilities of the WRF modeling system. As introduced earlier in the report, three configurations, or states, were established to track incremental improvements in performance: (1) a reference meteorology state, which is obtained by running the WRF modeling system as commonly done by meteorological modelers and forecasters, without invoking any urban parameterization, (2) a second state obtained by running WRF with the standard urban parameterizations as often done by urban-climate modelers, and (3) a third state obtained by running urban WRF with the Altostratus Inc. study-specific modifications to input (bottom-up approach), parameterizations, and model as discussed elsewhere in this report.

Table 9 and Table 10 summarize the improvements in WRF model performance using the Altostratus Inc.-modified version of uWRF in this study. The tables show improvements in model performance for the most important parameter in this study, air temperature, for the San Francisco Bay Area and Los Angeles regions, respectively. In each table, column 1 provides the year and interval (two-week intervals discussed in Section 2.3) and columns 2—5 are the metrics for the reference state. The metrics include mean bias and mean error computed for each of T2 and Tair. Both of these temperatures are at 2 m (6.5 feet) above ground level, but computed in different manners. T2 is computed based on surface temperature and a vertical heat-transfer coefficient in the atmosphere, while Tair is computed by interpolating between surface temperature and the prognostic temperature at the lowest level of the atmospheric model. Hence, Tair can be thought of as being more representative of a four-dimensional prognostic temperature field that also includes the effects of heat transport from one area to another, whereas T2 is more representative of a diagnostic air temperature.

Columns 6—9 and 10—13 represent the changes (relative improvements) in these metrics as a result of applying uWRF (urban parameterizations). Columns 6—9 show improvements in performance for the standard uWRF relative to standard nonurban WRF. Columns 10—13 show the improvements in model performance using the Altostratus Inc.-modified uWRF relative to the standard nonurban WRF. The tables show that the Altostratus modifications to uWRF have resulted in marked improvements in performance over both the standard nonurban WRF and the standard uWRF model (also see Figure 14 and Figure 15, discussed below).

The modeling results suggest that T2 is the better representative of temperature in the Los Angeles domain, and that Tair is the better representative in the San Francisco Bay Area and,

as such, each will be used accordingly in this performance evaluation. Thus, as can be seen in columns 10—13 of the tables, the modifications and modeling in this study improved WRF performance as follows (for mean bias, changes of over 100 percent in the tables mean a switch in sign relative to the reference state, but is reported as 100 percent below):

- For the San Francisco Bay Area domain: whereas the standard WRF-urban improves air temperature mean bias by 2—100 percent and mean error by 0—12 percent relative to the standard nonurban WRF, the Altostratus-modified WRF-urban improves mean bias by 19—100 percent and mean error by 2—46 percent relative to standard nonurban WRF. This is more than double (in some cases almost four times better than) the improvement relative to the standard WRF-urban.
- For the Los Angeles domain: whereas the standard WRF-urban improves air temperature mean bias by 27—100 percent and mean error by 5—21 percent relative to the standard nonurban WRF, the Altostratus-modified WRF-urban improves mean bias by 45—100 percent and mean error by 10—33 percent relative to standard nonurban WRF. Again, this is about double the improvement relative to the standard WRF-urban.

In absolute terms, these improvements are as follows:

- The reductions in the temperature mean bias for the San Francisco Bay Area domain are between 0.7°F and 3.4°F (0.4°C and 1.9°C), and for mean error, the reductions are between 0.1°F and 3.2°F (0.06°C and 1.8°C).
- For the Los Angeles region, reductions in the temperature mean bias range from 1.3°F to 2.6°F (0.77°C to 1.46°C), and the reductions in the mean error range from 0.5°F to 1.44°F (0.3°C to 0.8°C).

Thus, in the context of the aforementioned equivalence of 1°C ≈ 500 – 1,000 MW, the improvements in model performance, that is error reduction, are quite noteworthy (even though these are local, and not systemwide effects).

Table 9: Model Performance Improvements Using Modified, Customized uWRF in Greater San Francisco Bay Area

	Ref state				Standard WRF-urban WRT standard non-urban WRF				Altostratus Inc. WRF-urban relative to sta			
Domains and period	T2_bias	T2_error	Tair_bias	Tair_error	T2_bias	T2_error	Tair_bias	Tair_error	T2_bias	T2_error	Tair_bias	Tair_error
d04_2013_int1	2.86	3.15	2.34	2.76	-22%	-15%	-18%	-10%	-46%	-37%	-57%	-40%
d04_2013_int2	0.90	1.76	0.37	1.50	-62%	-12%	-100%	1%	-64%	-13%	-118%	-2%
d04_2013_int3	2.80	3.02	2.20	2.49	-26%	-19%	-23%	-12%	-44%	-36%	-53%	-36%
d04_2013_int4	2.34	2.70	1.73	2.20	-27%	-16%	-25%	-8%	-39%	-25%	-49%	-23%
d04_2013_int5	1.84	2.36	1.31	2.00	-27%	-13%	-26%	-7%	-42%	-22%	-58%	-23%
d04_2013_int6	1.40	2.21	0.99	2.01	-31%	-9%	-31%	-3%	-38%	-11%	-52%	-9%
d04_2013_int7	1.20	2.20	0.77	2.06	-27%	-3%	-27%	0%	-44%	-9%	-66%	-8%
d04_2014_int1	4.18	4.28	3.52	3.68	-16%	-14%	-13%	-9%	-38%	-35%	-45%	-39%
d04_2014_int2	2.63	3.07	1.91	2.53	-25%	-15%	-22%	-7%	-27%	-16%	-31%	-12%
d04_2014_int3	3.67	4.00	2.89	3.33	-21%	-15%	-17%	-10%	-37%	-29%	-47%	-31%
d04_2014_int4	1.61	2.52	0.88	2.04	-37%	-12%	-43%	-3%	-39%	-11%	-53%	-4%
d04_2014_int5	2.47	3.01	1.75	2.51	-25%	-12%	-23%	-6%	-31%	-16%	-38%	-13%
d04_2014_int6	2.27	2.79	1.69	2.35	-21%	-13%	-19%	-7%	-31%	-19%	-43%	-21%
d04_2014_int7	4.17	4.28	3.77	3.92	-6%	-5%	-4%	-3%	-43%	-40%	-50%	-46%
d04_2015_int1	3.50	3.86	2.78	3.28	-22%	-16%	-18%	-10%	-27%	-19%	-32%	-18%
d04_2015_int2	3.37	3.88	2.53	3.25	-27%	-17%	-24%	-9%	-32%	-20%	-39%	-18%
d04_2015_int3	0.93	2.79	-0.02	2.46	-86%	-6%			-89%	-1%		
d04_2015_int4	3.97	4.23	3.22	3.63	-15%	-12%	-11%	-6%	-22%	-17%	-30%	-20%
d04_2015_int5	1.54	2.59	0.71	2.23	-44%	-12%	-59%	-1%	-49%	-11%	-89%	-3%
d04_2015_int6	1.95	2.78	1.31	2.46	-25%	-9%	-24%	-3%	-27%	-10%	-33%	-6%
d04_2015_int7	3.48	3.87	3.11	3.69	-4%	-3%	-2%	-2%	-12%	-10%	-19%	-14%

Source: Altostratus Inc.

Table 10: Model Performance Improvements Using Modified, Customized uWRF in Greater Los Angeles Area

	Ref state				Standard WRF-urban WRT standard non-urban WRF				Altostratus Inc. WRF-urban relative to sta			
Domains and period	T2_bias	T2_error	Tair_bias	Tair_error	T2_bias	T2_error	Tair_bias	Tair_error	T2_bias	T2_error	Tair_bias	Tair_error
d07_2013_int1	1.81	2.69	1.98	3.04	-41%	-10%	-24%	6%	-80%	-28%	-102%	-33%
d07_2013_int2	1.91	2.43	2.23	2.73	-28%	-16%	-14%	-1%	-50%	-28%	-71%	-40%
d07_2013_int3	1.73	2.33	2.00	2.60								
d07_2013_int4	1.84	2.42	2.14	2.71	-41%	-21%	-23%	-2%	-62%	-33%	-82%	-40%
d07_2013_int5	1.66	2.24	2.09	2.75	-45%	-16%	-24%	3%	-71%	-28%	-88%	-35%
d07_2013_int6	1.45	2.18	1.96	2.76								
d07_2013_int7	1.55	2.15	2.13	2.75	-38%	-16%	-15%	2%	-50%	-24%	-65%	-32%
d07_2014_int1	1.31	2.45	1.73	3.14	-62%	-10%	-31%	8%	-100%	-25%	-118%	-31%
d07_2014_int2	2.01	2.77	2.43	3.31	-33%	-12%	-16%	4%	-71%	-28%	-97%	-39%
d07_2014_int3	0.90	2.24	1.21	2.78	-85%	-11%	-38%	10%	-108%	-13%	-121%	-16%
d07_2014_int4	0.78	2.07	1.18	2.52	-105%	-11%	-44%	13%	-133%	-15%	-130%	-17%
d07_2014_int5	1.24	2.15	1.72	2.87								
d07_2014_int6	1.23	2.11	1.90	2.87	-55%	-10%	-22%	6%	-82%	-17%	-90%	-27%
d07_2014_int7	2.00	2.58	2.82	3.43	-27%	-11%	-11%	2%	-45%	-20%	-68%	-35%
d07_2015_int1	1.49	2.60	1.94	3.20	-52%	-13%	-26%	3%	-79%	-18%	-103%	-31%
d07_2015_int2	2.02	2.98	2.50	3.51	-39%	-13%	-20%	2%	-61%	-20%	-84%	-31%
d07_2015_int3	0.95	2.41	1.31	2.96	-101%	-11%	-48%	9%	-131%	-10%	-144%	-19%
d07_2015_int4	1.76	2.92	2.45	3.78	-43%	-8%	-19%	4%	-76%	-18%	-97%	-32%
d07_2015_int5	1.32	2.17	1.90	2.97	-62%	-15%	-28%	7%	-87%	-16%	-101%	-23%
d07_2015_int6	2.06	2.83	2.83	3.73	-36%	-12%	-16%	4%	-71%	-21%	-92%	-35%
d07_2015_int7	0.73	2.29	1.59	3.29	-97%	-5%	-26%	9%	-147%	-10%	-117%	-25%

Source: Altostratus Inc.

Figure 14 and Figure 15 depict an example of model performance evaluation (to quantify performance improvements and forecasting accuracy) at the locations of mesonet stations in each study domain. The change in temperature forecast error is given as a percent of the reference-state error at each weather station. Figure 14 shows an example of improved forecasting in the Los Angeles region (example is for 2013, interval 4). In this case, model performance worsens at a very small number of stations (6). At all other stations (225), performance improves considerably. Note that while the scale in the figure is from -100 percent to +100 percent, the actual range in this example is -72.9 percent to +44.8 percent. Figure 15 shows an example of improved forecasting in the San Francisco Bay Area (example is for 2013, interval 1). In this case, model performance improves dramatically at 150 stations, but worsens at a small number of stations (10). The actual range is -80.2 percent to +88.9 percent.

Figure 14: Improved Forecasting Example in Los Angeles Region

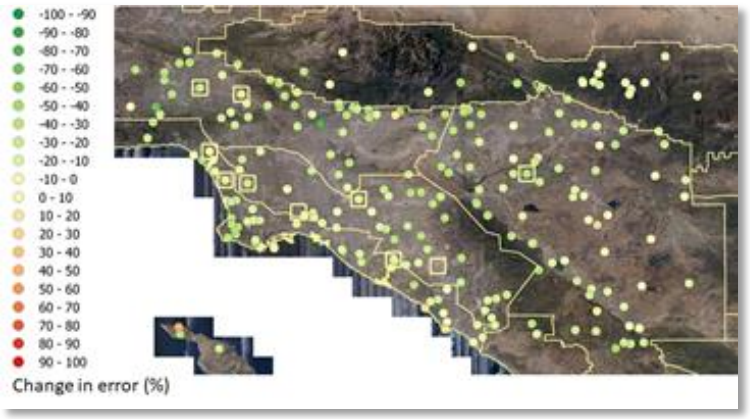

The change in error is given as a percent of reference-state error at each station. Yellow squares represent the locations of EPW weather-file stations (used in existing building energy modeling) in each region.

Source: Altostratus Inc.

Figure 15: Improved Forecasting Example in San Francisco Bay Area

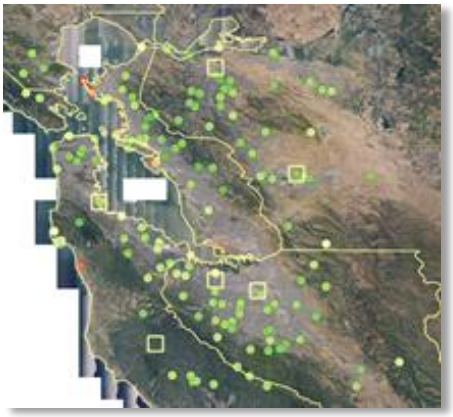

The change in error is given as a percent of reference-state error at each station. Yellow squares represent the locations of EPW weather-file stations (used in existing building energy modeling) in each region.

Source: Altostratus Inc.

3.2.3 Development of Fine-Scale Temperature Zones Based on Model Results

The current-climate temperature zones (discussed in Section 3.1.6) were created based on observations from mesonet and metar stations networks. The future-climate zones, discussed here, were developed based on both observations and model results from the urbanized WRF, as discussed earlier. Current climate zones based on model also were generated for reference purposes and for characterizing the changes into the future. In the following sections, the general characteristics of model climate zones are presented.

To avoid potential issues with bias (Sun et al., 2015) when computing future-climate conditions based on present-day climate-model results, this study mapped the changes (perturbations) obtained from the uWRF-downscaled simulations onto observed current-climate conditions, namely the averages of 2013—2015 for each synthetic month. In other words, this was similar to the concept of relative reduction factor used in air quality modeling of attainment of the eight-hour ozone standard, except (1) it was applied here to temperature (not ozone), and (2) it was not a reduction. It was also similar to the approach used in bias-correcting climate models (Bruyere et al., 2014), one of which was used in this study (CCSM4). This will also be discussed in the following sections.

Similar to Sun et al. (2015), who found that the best temperature descriptor in the Los Angeles region was a combination of 2/3 surface temperature and 1/3 air temperature, this study showed, as discussed above in Section 3.2.2, that the variable T2 from the uWRF model was the better indicator (producing better MPE in the Los Angeles region) than air temperature. On the other hand, the modeling also shows that air temperature (4-D prognostic temperature) is the better indicator in the San Francisco Bay Area, Fresno, and Bakersfield regions. Thus, these different temperature indicators were used according to their corresponding regions in this analysis.

At the time scales and spatial resolutions of most global climate studies, including those of the Intergovernmental Panel on Climate Change (IPCC), the tendencies in temperature are generally monotonic and positive, that is, temperature tends to increase with year and higher

representative concentration pathways (RCP), which are greenhouse gas concentration scenarios adopted by the IPCC. However, this study examined much finer spatiotemporal scales, that is kilometer-scale intraurban and intra-seasonal, hourly temporal resolutions. As such, perturbations of different signs around the generally increasing temperature mean became noticeable. That is, at the shorter time intervals and the finer resolutions, both increases and decreases in temperature occurred (compared to present conditions). This was seen, for example, in Table 11 as discussed next. Furthermore, when accounting for the effects of changes in urban land-use in future years (in addition to changes in climate) which was not often done in climate studies, a certain amount of cooling also occurred, because of the introduction of urban vegetation canopy cover, which in some cases was higher than vegetation cover in the nonurban surroundings that may have included desert, rangeland, or agriculture.

3.2.4 Threshold Exceedance

As there are several ways to evaluate intraurban variability in climate under current conditions and its change in the future, one simple indicator to begin the analysis with is temperature exceedance above some threshold. For example, a threshold of 95°F (35°C) has been used by utilities and researchers alike, such as Sun et al. (2015), to identify excessive heat events and to assess energy demand—thus it is used here as an example to demonstrate changes in the temperature field.

To do so, the number of stations (mesonets and metars) with 15-day average maximum daily temperature (~1500 PDT) greater than 95°F (35°C) was computed. For each of the time intervals one through seven listed in Table 11, in each year, the 15-day average of the maximum daily temperature was computed at each station, and if that average exceeded 95°F (35°C), then it counted as one station above the threshold (thus this 15-days basis is a more stringent criterion than computing exceedance as number of days, that is on a daily basis). Then, the total number of stations above this threshold was calculated and referred to as exceedance in the following discussion.

This is summarized in Table 11, where the values for *current* are based on observational analysis, that is, averages over years 2013—2015 for stations with valid observations (the results at each station were weighted by the number of hours with valid observations). The values for years 2050 and 2100 were computed using the bias-corrected approach discussed above; they were calculated by adding perturbations predicted by the model (uWRF) to the observations in the current climate. This was a unique approach (and unlike other studies where the absolute fields from model were used for the base year as well) in that it minimized potential errors from model bias. Thus, equation 6 was applied at each station location for every hour:

$$T_{future} = T_{present\_obs} + (T_{future\_model} - T_{present\_model}) \quad (6)$$

where the difference computed by the last two terms (in parentheses) is the perturbation in temperature obtained from the fine-resolution, modified uWRF model.

Figure 16 shows a small sample for this analysis for interval 6 listed in Table 11. Weather stations where the 15-day average of daily maximum temperature is greater than 95°F (35°C) are color-coded in red. The purpose of this figure is to show, spatially, where the exceedances

listed in Table 11 occurred in each study domain (Figures 18.A through 18.J in Appendix B provide additional information for other intervals and years).

Table 11: Stations with 15-Day Average Daily Maximum Temperature > 35°C

Bakersfield region (maximum number of stations = 12)					
		RCP 4.5		RCP 8.5	
	current	2050	2100	2050	2100
Int 1	0	10	4	4	3
Int 2	0	0	4	7	10
Int 3	4	8	0	12	11
Int 4	4	5	1	3	12
Int 5	2	5	4	5	12
Int 6	2	2	8	4	12
Int 7	0	0	2	0	12

Fresno region (maximum number of stations = 18)					
		RCP 4.5		RCP 8.5	
	current	2050	2100	2050	2100
Int 1	1	7	6	6	4
Int 2	1	2	6	7	12
Int 3	6	11	1	16	16
Int 4	6	7	2	6	17
Int 5	3	8	8	8	17
Int 6	3	3	12	5	17
Int 7	0	0	2	0	16

Los Angeles region (maximum number of stations = 306)					
		RCP 4.5		RCP 8.5	
	current	2050	2100	2050	2100
Int 1	0	6	0	6	3
Int 2	0	0	4	15	5
Int 3	0	18	0	60	76
Int 4	0	0	0	34	84
Int 5	12	0	19	0	57
Int 6	12	112	86	26	143
Int 7	1	4	16	0	174

San Francisco Bay Area region (maximum number of stations = 238)					
		RCP 4.5		RCP 8.5	
	current	2050	2100	2050	2100
Int 1	0	2	2	2	0
Int 2	0	0	2	2	10
Int 3	0	1	0	3	0
Int 4	0	0	0	0	6
Int 5	0	0	0	0	77
Int 6	0	0	3	0	20
Int 7	0	0	0	0	2

Int 1: June 1—15, Int 2: June 16—30, Int 3: July 1—15, Int 4: July 16—31, Int 5: August 1—15, Int 6: August 16—31, Int 7: September 1—15.

Source: Altostratus Inc.

In the Los Angeles region (top two images in Figure 16), observational data from the monitoring networks indicated that in the current climate, only a few scattered areas (12 stations) in the IE (east basin) were above the threshold. These sparse areas were located in the eastern and southern parts of the EB. In the San Gabriel Valley, only one station exceeded the threshold (located in Azusa). Except for these stations, the Los Angeles domain, overall, including east and west basins, as well as the San Fernando Valley, was below the threshold.

In the 2050 RCP 4.5 projection of this interval (top right, Figure 16), a much larger area is above the threshold, including all of the IE, areas in San Gabriel Valley, Glendale, Pasadena, and central and western San Fernando Valley (112 stations above the threshold). In the 2100 RCP 4.5 projection of this same interval (not shown), the areas above the threshold were similar to those in 2050, but with a smaller number of stations above the threshold (86). In the 2050 RCP 8.5 projection of interval 6 (not shown), the spatial pattern of areas exceeding the threshold was similar to that of the 2050 RCP 4.5 projection, with most of the exceedances in the IE, but with relatively more stations over the threshold (26 instead of 12). Finally, in the 2100 RCP 8.5 projection of this interval (not shown), exceedances were throughout the IE (east basin), San Gabriel Valley, San Fernando Valley, and surrounding areas. The number of stations exceeding the threshold in this scenario was 143. In this scenario also was the first appearance of exceedances in the quasi-coastal areas of the west basin, including in areas that are in generally mild climates, such as cities of Bellflower, Paramount, La Mirada, Whittier, Yorba Linda, Mission Viejo, and Irvine.

Figure 16: Exceedances Above 95°F (35°C), Los Angeles Region and San Francisco Bay Area

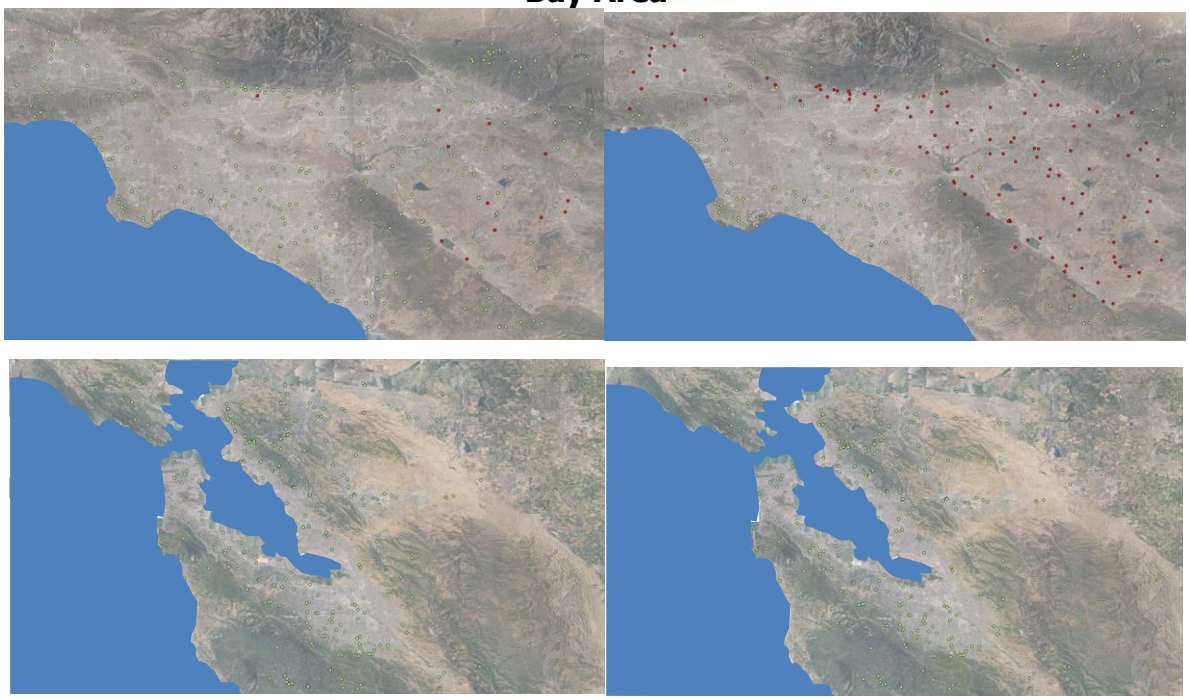

Top row, Los Angeles region; Bottom row, San Francisco Bay Area. Stations with 15-day average maximum temperature > 35°C are color-coded red. Left: Interval 6 (August 15—31 years 2013—2015 averages based on observations; Right: Interval 6, year 2050 RCP 4.5 (based on observations + modeling).

Source: Altostratus Inc.

In the San Francisco Bay Area domain, and as seen in the bottom of Figure 16, the current conditions (based on observational data) exhibited no exceedances above the 35°C threshold. This is still the case in the 2050 RCP 4.5 projection of this interval (bottom right of Figure 16). In the 2100 RCP 4.5 projection (not shown) a very small area (two stations) exceeded the threshold in the city of Tracy. In the 2050 RCP 8.5 projection, as in the 2050 RCP 4.5 case, no exceedance above the threshold existed in the San Francisco Bay Area. However, in the 2100 RCP 8.5 projection (not shown), a large area (20 stations) was above the threshold, including cities of Tracy, Antioch–Discovery Bay, Martinez, Concord-Clayton, Pleasant Hill, Walnut Creek, Danville, Blackhawk, Dublin-Livermore, and Morgan Hill (also see Figure 18 in Appendix B).

3.2.5 Comparison with CEC Climate Zones

In this section, the probabilistic fine-resolution intraurban temperature zones (developed in this study) are compared to the existing climate zones adopted by the CEC (16-zone scheme discussed in Chapter 1). The goal is to demonstrate the potential for improvement by possibly redrawing the boundaries of the current CEC climate zones or by considering new zones that are finer in scale (as discussed in the following sections). To provide a basis for comparisons, fine-scale temperature zones are first discussed here based on observational data from existing mesonet and metar networks in each area. Then, the temperature zones based on model will be discussed later in following sections.

In Figure 17, examples of all-hour averages in temperature are presented (the same exercise can be carried out for peak hours, minima, or any other selected time interval and some examples are shown in following sections). Figure 16 shows observational synthetic months 2013—2015 (units of DH/day, non-threshold, and the ranges are provided in a caption beneath each figure). Figure 17.A through Figure 17.D show the Los Angeles region; Figure 17.E through Figure 17.H are for the San Francisco Bay Area. In each figure, the colored Thiessen polygons reflect the DH/day metric for each station location, while the thick black lines show the existing CEC building climate zones superimposed on the domain of interest. Arrows indicate the difference (°C) between all-hour average temperatures of (across) the indicated CEC climate zones (obtained from CZ weather files for corresponding climate zones and month). The CEC climate zones are numbered on each figure, corresponding to the weather files that represent them.

To evaluate whether the intraurban variability in temperature at the finer scales are meaningful, the variations in all-hours temperature (computed from DH/day) were compared to the inter-zone temperature differences across each CEC climate zone for the month of interest. The arrows across each pair of CEC climate zones (in Figure 17) indicate the differences between the all-hours temperature averages (for the month) of each of the indicated pairs of climate zones. In other words, the arrows show the difference across the boundaries of each CEC climate zones pairs so it can be compared to the magnitudes of intraurban temperature variability within each of the two zones in the pair. These differences were computed by averaging all-hours temperatures in the weather files corresponding to each zone for the month in question. Table 12 lists the all-hours averages of air temperature in each CZ file for the given region and month.

Thus, while Figure 17 (A through H) shows the spatial characteristics of the intraurban (intra-zone variations) relative to inter-zone variations (across CEC climate zones), Table 13 and

Table 14 provide the ranges of these temperature differences for the Los Angeles and San Francisco Bay Area domains. In each of these two tables, the top row identifies the CEC climate zones across which the differences are calculated, and within which the ranges of intraurban (intra-zone) variability are given for each month.

Table 12: All-hours Average Temperature in CEC Building Climate Zones

CEC climate zone	June	July	August	September
CZ 03	60.63	62.55	62.42	63.61
CZ 04	65.66	68.19	68.27	69.91
CZ 06	66.94	69.74	68.08	69.05
CZ 08	67.89	71.23	72.15	71.88
CZ 09	68.77	72.97	74.56	74.44
CZ 10	71.11	75.50	76.95	75.16
CZ 12	71.68	74.77	73.36	72.17
CZ 13	78.40	84.12	81.81	76.88
CZ 16	64.30	72.10	70.67	64.25

Temperatures are °F averaged from climate-zone weather files of corresponding zone and month. Only zones of interest of the 16 California climate zones are listed in this table.

Source: Altostratus Inc.

To explain how Table 13 and Table 14 are interpreted, the following random example is provided for the yellow-highlighted cells in Table 13. In this example, for the month of June in the Los Angeles domain, the value 0.52°C (in row 3) is the difference between the all-hours average temperature (in June) in CEC zone 6 and the all-hours average temperature in CEC zone 8 (as indicated by the two-way arrow in row 1). Thus the value 0.52 is positioned at the center of the cell, midway between the two ends of the arrow to indicate that this is a cross-boundary temperature difference, in this case, across CEC climate zones 6 and 8. Next, the two values 2.36 and 3.54 in row 4 are the intra-zone (intraurban) variations within each respective CEC climate zone, computed from mesonet and metar stations in the area. That is, 2.36°C is the range of variations in all-hours temperature average within CEC zone 6, and 3.54°C is the range of variations in all-hours temperature average within CEC zone 8. Thus in this example, the intra-zone (intraurban) variability in all-hours temperature averages within each of the two CEC zones (6 and 8) is several times larger than the cross-boundary temperature difference of 0.52 (4.5 to 6.8 times larger, respectively), suggesting that there is reasonable basis to redraw the existing CEC climate zone boundaries or introduce finer-resolution zones in this area, which was one objective of this study. In a similar manner, comparisons of row 4 to 3 (for June), row 7 to 6 (for July), row 10 to 9 (for August), and row 13 to 12 (for September) are repeated for each set of temperature zones. It can be concluded that except for a very few cases, that the intraurban fine-scale variations in temperature (within each CEC climate zone) are of the same magnitude or substantially larger than the inter-climate zone (across CEC zones) variations in temperature. Thus, this justifies at least some consideration in the future for the use of revised summer climate zones such as the ones discussed here.

Furthermore, because there is large intraurban variability in temperature (intra-zone), for example, up to ~14.4°F (8°C) in the Los Angeles domain and up to ~9°F (5°C) in the San Francisco Bay Area domain, there is potential (at least in theory) to better allocate resources meaningfully, if utilities considered such intraurban temperature zoning in their forecasts and

long-term planning for electricity. For example, using data from Garcia-Cerrutti et al. (2010), the daily peak demand (megawatts, MW) sensitivity to daily peak temperature (max631)[3] in investor-owned utilities[4] service territory is computed as follows (for years 2008—2010) on the average:

For PG&E:	360 MW/°F	(648 MW/°C)
For SCE:	320 MW/°F	(576 MW/°C)
For SDG&E:	63 MW/°F	(113 MW/°C)

Thus, the intraurban (intra-zone) temperature variability discussed above, and shown in rows 4, 7, 10, and 13 of Table 13 and Table 14, is very important and should be accounted for in some fashion in planning and forecasting for the electric system. Other analysis (Davis et al., 2004) estimates even larger sensitivities for the California Independent System Operator peak temperature versus demand: 1,000 MW/1°C peak temperature (but not based on 631). Thus, the improved accuracy in allocating generating resources could actually by twice as large from improved model performance and establishment of new temperature zones as proposed here.

Table 13: Comparison of Inter- and Intra-Zone Temperature Variability in Los Angeles Domain

1	CEC climate zones	6 ◄─► 8		8 ◄─► 9		8 ◄─► 10		9 ◄─► 10		9 ◄─► 16		10 ◄─► 16	
2	June												
3	Inter-zone	0.52		0.48		1.78		1.30		2.48		3.78	
4	Intra-zone	2.36	3.54	3.54	4.72	3.54	7.08	4.72	7.08	4.72	8.26	7.08	8.26
5	July												
6	Inter-zone	0.82		0.96		2.37		1.40		0.48		1.88	
7	Intra-zone	3.39	3.39	3.39	4.52	3.39	5.65	4.52	5.65	4.52	6.78	5.65	6.78
8	August												
9	Inter-zone	2.26		1.33		2.66		1.32		2.16		3.48	
10	Intra-zone	2.40	3.60	3.60	4.80	3.60	4.80	4.80	4.80	4.80	7.20	4.80	7.20
11	September												
12	Inter-zone	1.57		1.42		1.82		0.40		5.66		6.06	
13	Intra-zone	2.74	2.74	2.74	5.48	2.74	2.74	5.48	2.74	5.48	8.22	2.74	8.22

In °C based on observational data from mesonet and metar networks.

Source: Altostratus Inc.

[3] max631 temperature is defined by Garcia-Cerrutti et al. (2010) as 60 percent of today's peak temperature + 30 percent of yesterday's peak temperature + 10 percent of peak temperature from two days prior.

[4] Investor-owned utilities (IOU) are managed by the California Independent System Operator and comprised of PG&E, SCE, and SDG&E)

Table 14: Comparison of Inter- and Intra-Zone Temperature Variability in San Francisco Bay Area Domain

1	CEC climate zones	4 ◄─► 3		4 ◄─► 12		3 ◄─► 12	
2	June						
3	Inter-zone	2.79		3.34		6.13	
4	Intra-zone	3.50	5.25	3.50	7.00	5.25	7.00
5	July						
6	Inter-zone	3.13		3.65		6.78	
7	Intra-zone	4.08	5.44	4.08	5.44	5.44	5.44
8	August						
9	Inter-zone	3.25		2.82		6.07	
10	Intra-zone	3.24	4.32	3.24	5.40	4.32	5.40
11	September						
12	Inter-zone	3.50		1.25		4.75	
13	Intra-zone	4.74	4.74	4.74	4.74	4.74	4.74

In °C based on observational data from mesonet and metar networks.

Source: Altostratus Inc.

Figure 17: Inter- and Intra-Zone Differences in All-Hours Temperature Averages (Los Angeles Region and San Francisco Bay Area)

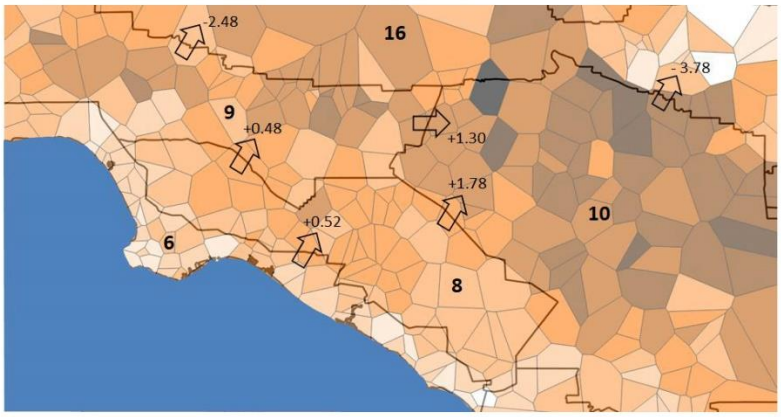

A

Range (light color to dark): 376—631°C·hr/day; each interval change in color is equivalent to a change of 4.1°F (1.18°C) in all-hour average temperature for June.

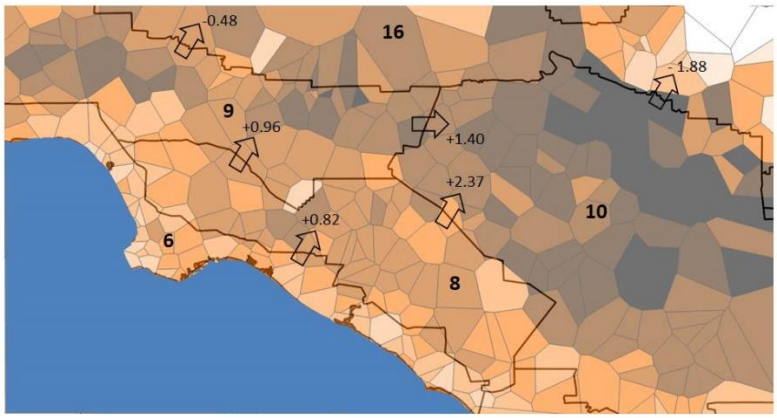

B

Range (light color to dark): 392—637°C·hr/day; each interval change in color is equivalent to a change of 2.03°F (1.13°C) in all-hour average temperature for July.

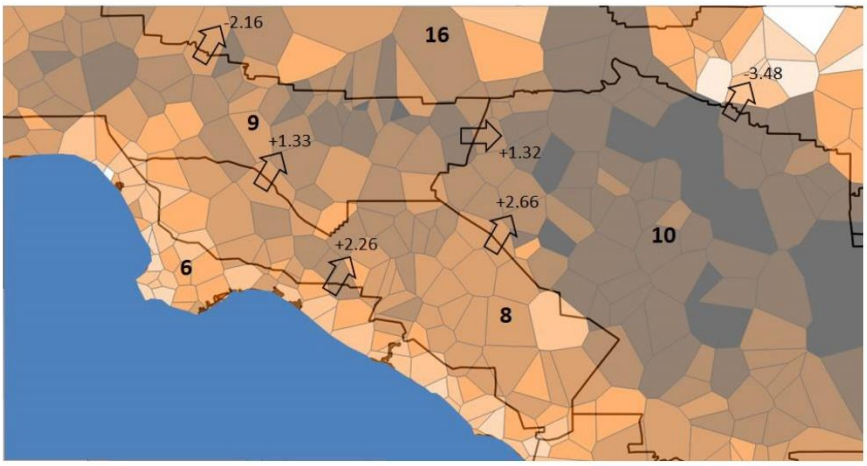

C

Range (light color to dark): 395—654°C·hr/day; each interval change in color is equivalent to a change of 2.16°F (1.20°C) in all-hour average temperature for August.

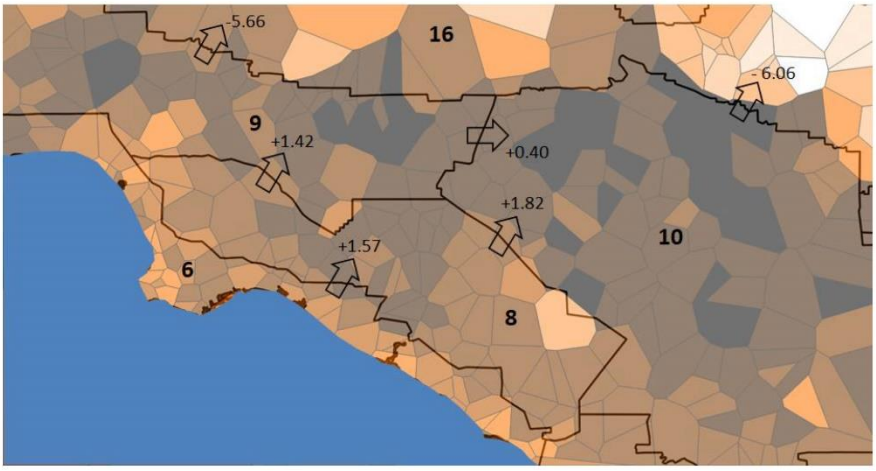

D

Range (light color to dark): 345—642°C·hr/day; each interval change in color is equivalent to a change of 2.47°F (1.37°C) in all-hour average temperature for September.

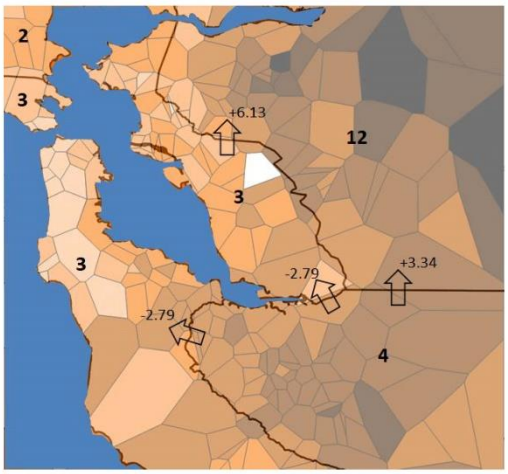

E

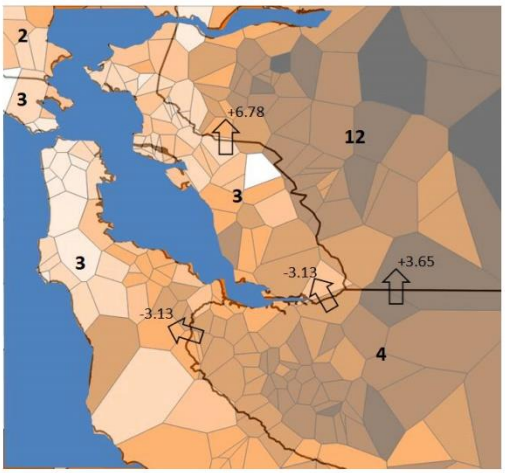

F

Range (light color to dark): 215—591°C.hr/day; each interval change in color is equivalent to a change of 2.15°F (1.75°C) in all-hour average temperature for June I, Range: 307—601°C.hr/day; each interval change in color is equivalent to a change of 2.45°F (1.36°C) in all-hour average temperature for July (F).

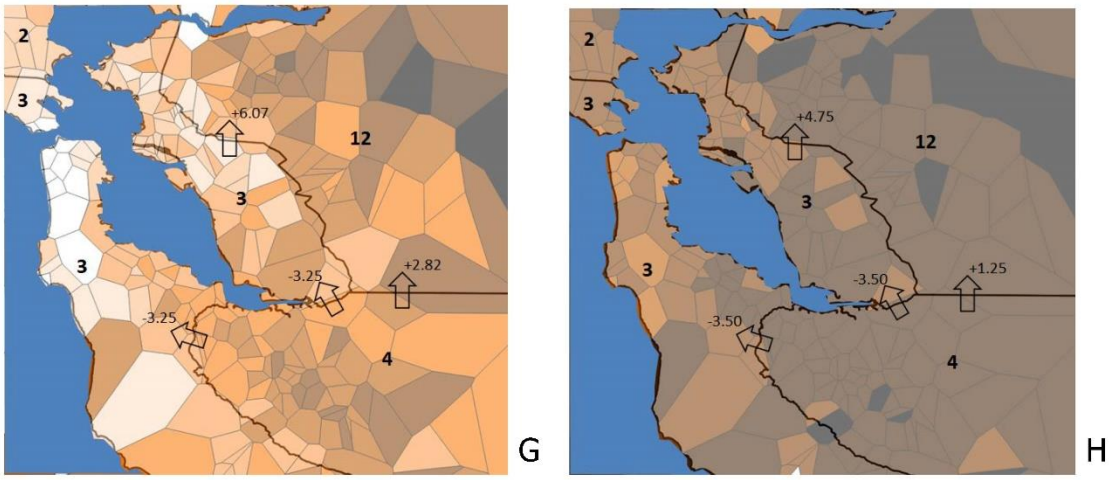

Range (light color to dark): 357—590°C·hr/day; each interval change in color is equivalent to a change of 1.94°F (1.08°C) in all-hour average temperature for August (G), Range: 64—576°C·hr/da); each interval change in color is equivalent to a change of 4.27°F (2.37°C)in all-hour average temperature for September H.

Source: Altostratus Inc.

3.2.6 Temperature Changes from Current to Future Climates

This section provides a discussion of how the temperature field (based both on observations and modeling) changes in future climate and land use. This can also form the basis for proposing new intraurban climate (temperature) zones for the study areas, such as the San Francisco Bay Area and Los Angeles region. Figure 18 (A through L), below, shows snapshot examples from this analysis as averages over JJAS (other times, areas, and years are shown in Figures 19.1 through 19.36 in Appendix B).

Of note:

- The temperature fields presented in Figure 18 (and 19 in Appendix B) resulted from applying the Altostratus-modified uWRF model (modifications discussed earlier) in dynamically downscaling the CCSM4 climate-model fields, running the localized simulations with uWRF, and accounting for the effects of both changes in climate and in land use in the future (the latter based on the USGS LUCAS projections presented earlier).
- To develop the perturbations in 2050 or 2100 relative to current climate, the same RCP scenario was used (in the model) for current years (for example, 2015) as for the future years. To compute, for instance, the changes in 2050 RCP 4.5 relative to current climate, the model used current years, 2015 in this case, with a corresponding RCP of 4.5 as the basis to compute the differences. This ensured consistency across the scenarios and years when quantifying changes relative to current conditions.
- The temperature field plotted in these figures is in units of degree-hours per hour (DH/H), hence it represents an all-hours averaged temperature (°C) including all day and night hours throughout the calculation periods (intervals). The DH/H metrics represents long-term averages in each interval and thus provides a probabilistic assessment of the changes in intraurban temperature zones (along with perturbations and standard error to be discussed further below).

The examples shown in Figure 18 are changes by the year 2050 relative to current climate, for RCP 4.5 and 8.5, and for all hours, 0300 PDT, and 1500 PDT averages over JJAS. These are model-predicted air temperature changes for the Los Angeles region and the San Francisco Bay Area. The light blue background in each figure depicts the urban land-use extent at the corresponding year (2050 in this example) and the small circles represent the locations of the mesonet stations where the model results are computed.

It is important to recall that these are changes (such as warming) predicted at each weather station location in 2050 or 2100 relative to its conditions in current climate. Thus, this is relative local change at each station location, or area, not a change across different regions. In other words, if a certain location appears to have larger warming than another (as shown in the figures), that does not necessarily mean that the location has become warmer (in absolute terms) relative to other areas but, rather, that it warmed relatively more than those other locations.

Some observations on the spatial characteristics of temperature changes (across all periods and including all-hours, 1500 PDT, and 0300 PDT averages) are as follows:

Los Angeles region (some examples shown in Figure 18 A, B, E, F, I, and J):

- The higher elevations (San Gabriel, San Bernardino, San Jacinto, and the Santa Ana Mountains) are consistently impacted by increased temperatures, but to varying degrees. This is mainly because of the shallower boundary layer at those elevations. Thus, changes in temperature are more noticeable in those areas, because of more limited vertical mixing. In 2050 (relative to current climate), there is a more pronounced contrast between the warming at the higher elevations and warming elsewhere in the domain. In 2100, that contrast becomes either moderate or nonexistent in some cases, indicating a more mixed temperature-change field in 2100 relative to 2050, possibly as a result of increased venting.
- The northern mountains range (San Gabriel–San Bernardino Mountains) and areas nearby warm up more, relative to other parts of the domain, at the times of the nighttime minimum temperature than during the daytime.
- The coastal areas see warming under the RCP 4.5 scenario in 2050 and 2100 (relative to current climate), but no substantial warming in the RCP 8.5 scenario for either 2050 or 2100. Again, it is possible that this is a result of a *reverse coastal cooling* effect as discussed in Lebassi et al. (2011) and Taha (2017).
- Compared to warming in other parts of the domain, the west basin's (WB) semi-coastal and coastal areas warm more during the night than during the day.
- The EB/IE areas see warming in all scenarios but with different magnitudes compared to other areas in the domain. The eastern and southern parts of the IE warm up consistently more than the rest of the IE or relative to other areas in the domain.
- San Fernando Valley (SFV) and San Gabriel Valley (SGV) generally see increased temperatures except for RCP 4.5 in 2050 (relative to current climates). In certain cases, such as RCP 8.5 2100, SFV sees larger local warming than SGV.
- The WB generally warms up in all cases, but to varying degrees. In RCP 4.5 2050, the WB sees larger warming than EB/IE and other areas surrounding the WB.

- The San Pedro–Long Beach–Whittier–East Los Angeles (SLWELA) heat plume is generally warmer than its surroundings in the rest of the WB through all scenarios. In some cases (RCP 4.5 2100 and RCP 8.5) the SLWELA plume warms up more than the rest of the WB and also sees more warming than in SFV and SGV.

San Francisco Bay Area (some examples shown in Figure 18 C, D, G, H, K, and L):

- RCP 4.5 for year 2050 is the only scenario where the Santa Clara Valley proper (floor) warms up the most in the domain. In all other scenarios and years, it is the mountains surrounding the valley that warm up the most. In these conditions, however, there is a U-shaped warming pattern (following the valley's outline) with increased temperatures in the NW—SE direction, away from the bay and toward Gilroy, especially during the times of the daily maximum temperature.
- In most scenarios, the eastern and southern parts of the San Francisco peninsula warm up more than its western part, as the latter is influenced by proximity to the Pacific Ocean.
- The area from San Francisco International airport (SFO) to Palo Alto warms up dramatically in various scenarios, particularly during the times of the daily maximum temperature.
- Other areas that warm up considerably in this domain include Pittsburg-Antioch–Discovery Bay, East Concord, and Walnut Creek.
- Areas that warm up the least are the western parts of the San Francisco peninsula and the Richmond-Berkeley-Oakland strip closest to the bay, because they are influenced by the wind flow pattern from the ocean and the Golden Gate, respectively.
- The Tracy-Manteca area, as well as San Rafael, often see larger warming than some other parts of the domain

Table 15 provides a summary of domain-wide ranges of temperature change. In coastal areas (Los Angeles region and San Francisco Bay Area), a few small negative values in the table may be attributable to the reverse coastal cooling effect that is a consequence of increased inland air temperature (Taha 2017; Lebassi et al., 2011), as discussed above. Note that there are no negative changes in temperature in the Fresno region. It is also to be noted that (1) the cooling (negative values) is small compared to the warming, as seen in Figure 18 (and Figures 19.1 through 19.36 in Appendix B), and (2) that it is limited to smaller areas, although the warming is dominant throughout the domains.

Results in Table 15 also indicate, in general, that the minimum temperatures rise relatively more than the maximum daily temperatures, which is in line with most current research findings. However, it's to be borne in mind that the results here are from a much higher-resolution observational-modeling characterization compared to other efforts. As shown in Figure 18 (and 19.1 through 19.36 in Appendix B), and in the summary notes above, certain areas (intraurban variations) in the domain indeed are affected by larger nighttime warming. It can also be seen in Table 15 that, in general, temperature increases with RCP scenario and year. Finally, the largest range of warming among the three regions is seen in the Fresno domain.

Table 15: Range of Temperature Change for Years 2050 and 2100 Relative to Current Climate

		RCP 4.5		RCP 8.5	
		2050 minus current	2100 minus current	2050 minus current	2100 minus current
All-hours mean (JJAS) domain range ˚C					
1	LA region	-0.25 - 1.42	0.32 - 1.20	-0.13 - 1.75	2.32 - 4.18
2	Fresno region	0.97 - 1.23	1.50 - 1.83	1.50 - 1.72	4.62 - 4.97
3	SFBA	0.83 - 1.81	0.49 - 1.78	-0.48 - 1.37	1.86 - 4.48
Mean daily minimum (JJAS) domain range ˚C					
4	LA region	-0.13 - 1.43	0.49 - 1.34	-0.50 - 1.90	2.26 - 4.20
5	Fresno region	1.01 - 1.36	1.86 - 2.37	1.33 - 1.80	4.73 - 5.34
6	SFBA	0.93 - 1.80	0.73 - 2.13	-0.46 - 1.41	1.90 - 4.65
Mean daily maximum (JJAS) domain range ˚C					
7	LA region	-0.51 - 1.67	-0.21 - 2.06	-0.18 - 1.87	2.20 - 4.34
8	Fresno region	0.85 - 1.07	1.02 - 1.20	1.62 - 1.80	4.32 - 4.57
9	SFBA	0.31 - 2.00	-0.09 - 1.40	-0.64 - 1.50	1.54 - 4.34

Domain-wide; DH/H in °C as averages over June, July, August, and September.

Source: Altostratus Inc.

This table corresponds to the ranges shown in Figures 19.1 through 19.36 in Appendix B, as well as the examples shown in Figure 18.

Figure 18: Changes in Model Temperature Field Averaged for Four Months

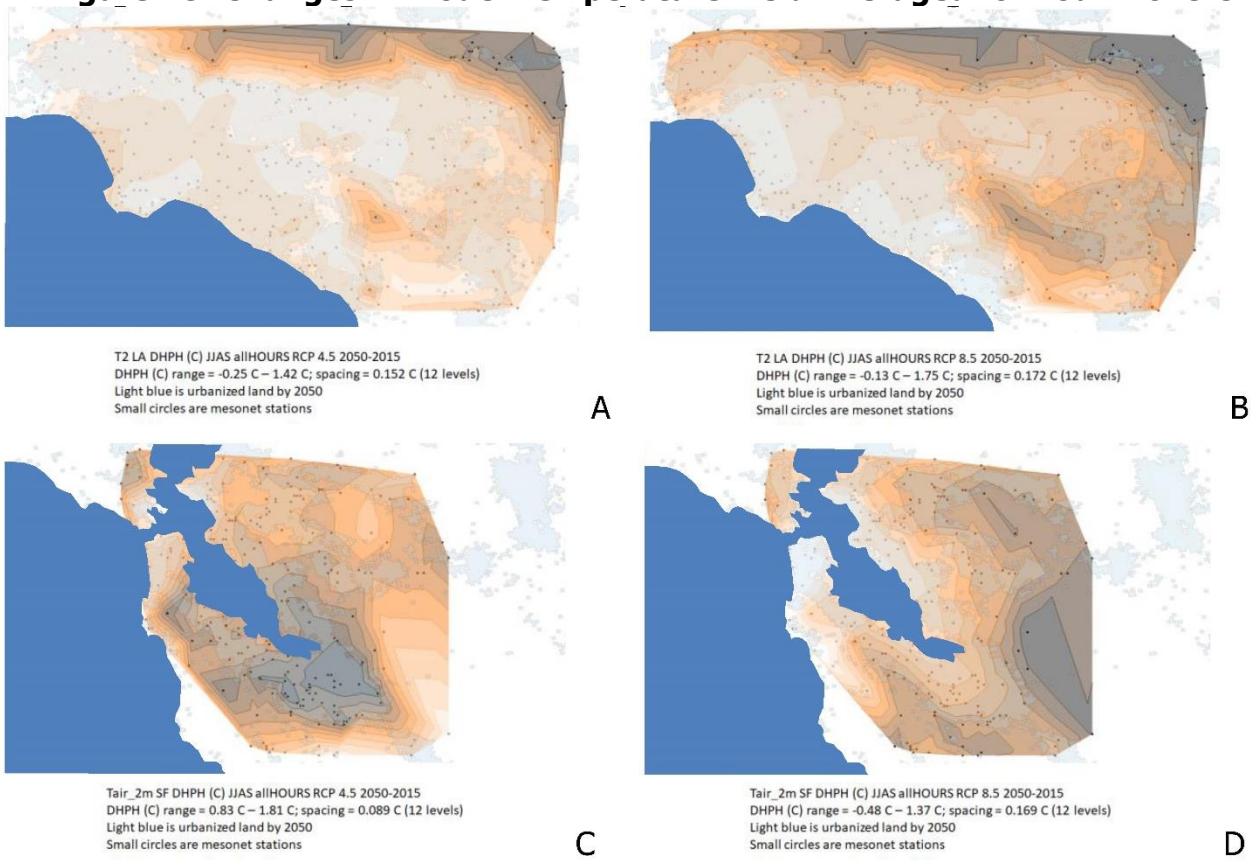

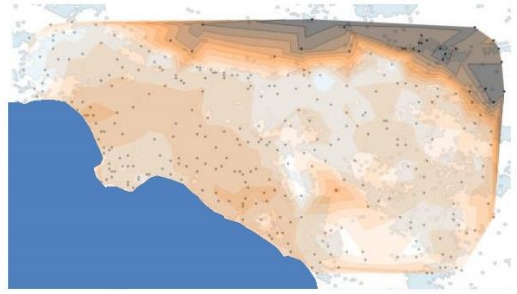

T2 LA DHPH (C) JJAS 0300_PDT RCP 4.5 2050-2015
DHPH (C) range = -0.13 C – 1.43 C; spacing = 0.1422 C (12 levels)
Light blue is urbanized land by 2050
Small circles are mesonet stations

E

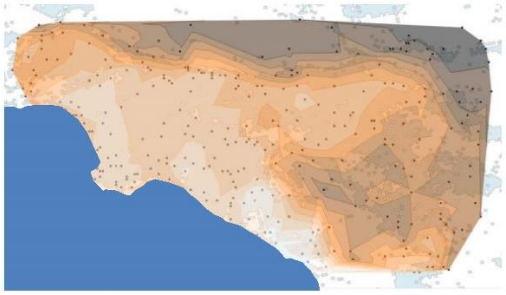

T2 LA DHPH (C) JJAS 0300_PDT RCP 8.5 2050-2015
DHPH (C) range = -0.5 C – 1.90 C; spacing = 0.22 C (12 levels)
Light blue is urbanized land by 2050
Small circles are mesonet stations

F

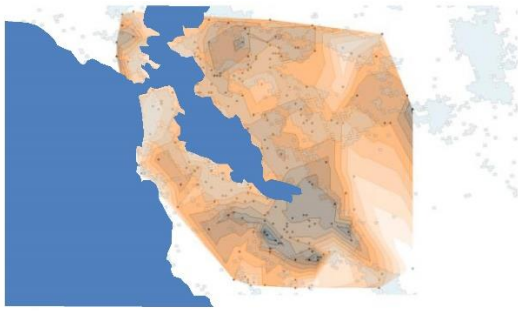

Tair_2m SF DHPH (C) JJAS 0300_PDT RCP 4.5 2050-2015
DHPH (C) range = 0.93 C – 1.80 C; spacing = 0.0793 C (12 levels)
Light blue is urbanized land by 2050
Small circles are mesonet stations

G

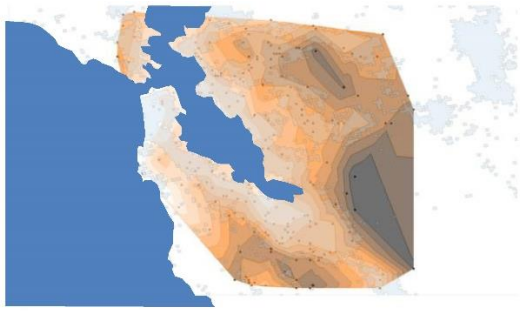

Tair_2m SF DHPH (C) JJAS 0300_PDT RCP 8.5 2050-2015
DHPH (C) range = -0.46 C – 1.41 C; spacing = 0.17 C (12 levels)
Light blue is urbanized land by 2050
Small circles are mesonet stations

H

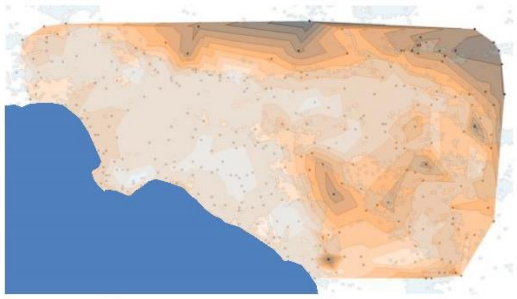

T2 LA DHPH (C) JJAS 1500_PDT RCP 4.5 2050-2015
DHPH (C) range = -0.51 C – 1.67 C; spacing = 0.198 C (12 levels)
Light blue is urbanized land by 2050
Small circles are mesonet stations

I

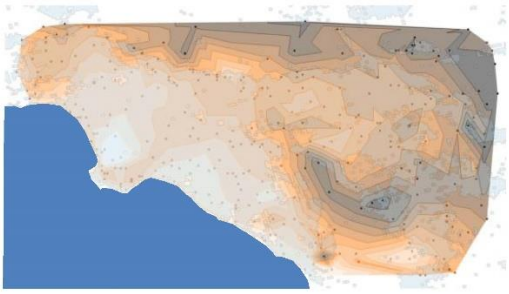

T2 LA DHPH (C) JJAS 1500_PDT RCP 8.5 2050-2015
DHPH (C) range = -0.18 C – 1.87 C; spacing = 0.187 C (12 levels)
Light blue is urbanized land by 2050
Small circles are mesonet stations

J

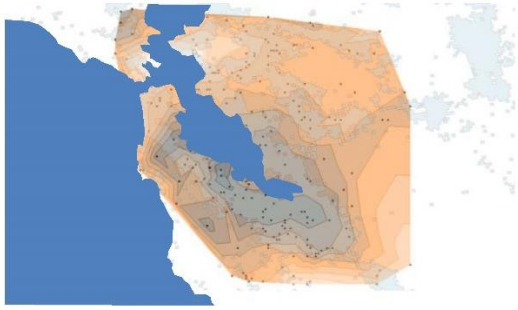

Tair_2m SF DHPH (C) JJAS 1500_PDT RCP 4.5 2050-2015
DHPH (C) range = 0.31 C – 2.00 C; spacing = 0.154C (12 levels)
Light blue is urbanized land by 2050
Small circles are mesonet stations

K

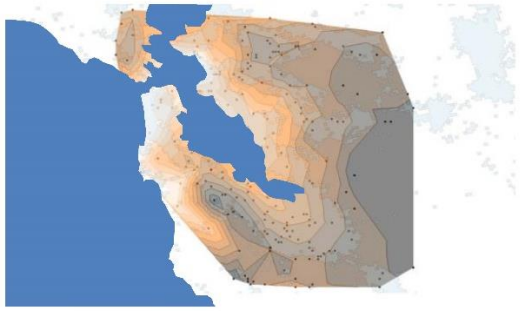

Tair_2m SF DHPH (C) JJAS 1500_PDT RCP 8.5 2050-2015
DHPH (C) range = -0.64 C – 1.50 C; spacing = 0.195 (12 levels)
Light blue is urbanized land by 2050
Small circles are mesonet stations

L

Temperature (DH/H) differences (2050 – 2015) averaged for June, July, August, and September for all hours, 0300 PDT, and 1500 PDT. Left column: RCP 4.5; Right column: RCP8.5. Other intervals and year 2100 differences are provided in Figure 19 in Appendix B.

Source: Altostratus Inc.

3.2.7 Mean Departures from California Energy Commission Climate-Zone Stations

3.2.7.A Mean Departures from California Energy Commission Climate-Zone Stations in Current Climate

In this section, the probabilistic intraurban variability in climate (focusing on temperature) is characterized in terms of mean departures (from values at handshake points) and perturbations (standard error) around the mean departures.

In Section 3.2.5, absolute observed temperatures at each station in the domain were used to construct synthetic-month DH/day metrics and compute all-hours average temperatures at each station and for each synthetic month. The ranges of these all-hours temperature averages were then compared to temperature from CZ weather files representing CEC climate zones. That is, the intra-zone variations in all-hours averages were compared to inter-zone (cross-boundary) all-hours average differences in temperature across CEC climates zones.

In this section, the analysis for current climate still relied on observational data from metar and mesonet stations, but temperature differences (not absolute) were used to characterize intraurban variability relative to CEC weather stations (as an example of handshake or reference points). That is, the observed hourly temperatures at a selected CEC station and at each mesonet and metar stations in the domain were used to develop the correlations discussed here. Note that the temperature at the CEC stations (used in these calculations) were the actual hourly observed temperatures corresponding to the periods of interest, not temperatures from a CZ weather file as was done in Section 3.2.5.

Thus, this section presents the development of correlations among each and all mesonet station locations and the CEC climate-zone stations (three CEC stations in the Los Angeles region, and two in the San Francisco Bay Area), used here as handshake points. The correlations were developed as mean departures from the CEC-stations values and a perturbation (standard error) around that mean departure, as defined below in equations 7 and 8. The handshake points, of course, could be any other point or metrics of interest—here the project used the CEC climate-zone stations to show the improvements targeted in this study as well as for comparison with results presented in Section 3.2.5.

The first step in developing the temperature correlations among various weather stations and the handshake points and in developing the intraurban microclimate zones was to split the variables (temperature differences) by solar radiation. This was done to isolate periods of cloudiness throughout the domains or during times of coastal stratus (in the San Francisco Bay Area and Los Angeles domains) and account for them separately when developing the correlations. The daily accumulated solar radiation was calculated (in this project) from sunrise to 1500 PDT each day at weather stations reporting solar radiation observations (these stations were shown in Figure 11). This analysis resulted in the ordering of mesonet stations from inland-most to coastal-most locations, focusing on stations in urban areas (analysis not shown in this report).

Following this step, correlations were developed at each of the mesonet stations locations in each study region. The correlations were developed in each temperature zone relative to handshake points, that is metars or CEC climate-zone stations, and were grouped by

accumulated solar radiation in each temperature zone and for each synthetic month (that is, June, July, August, and September across years 2013—2015).

The correlations discussed in this section were based on observations from the monitor networks in the study regions. In following sections, similar correlations are presented based on modeling of current years, future climates, and land-use scenarios to develop summer temperature zones as probabilistic intraurban climate characterizations. The correlations are presented here as mean departures and perturbations within each temperature zone relative to CEC climate-zone stations.

Thus, for air temperature:

$$Tair_{i,z,m,s,t} = \overline{TairM_{z,m,s,t}} + \overline{\Delta T_{i,z,m,s,t}} + \Delta T'_{i,z,m,s,t} \qquad (7)$$

$$Tair_{i,z,m,s,t} = \overline{TairCECn_{z,m,s,t}} + \overline{\Delta Tn_{i,z,m,s,t}} + \Delta Tn'_{i,z,m,s,t} \qquad (8)$$

where:

Tair The forecast temperature, that is, to be characterized at the mesonet station *i.*

TairM The temperature averaged over metar stations in a temperature zone (*z*). Thus, this is not only a temporal average over the period *t*, but also a spatial average over the metars located in a temperature zone (*z*) (see Figures 20.A through 20.E in Appendix B).

TairCECn The temperature at each CEC climate-zone station (*n*), averaged over period *t* (but not averaged spatially—that is, each mesonet station was correlated to one CEC station, *n*, at a time, separately). The CEC stations in the Los Angeles region are KLGB, KBUR, and UCRC1 and in the San Francisco Bay Area, they are KOAK and KSJC.

ΔT The mean departure of temperature at the mesonet station *i* (averaged over *t*) from the mean of the metar temperatures (*TairM*).

$\Delta T'$ Standard error of temperature differences around the mean departure (range of temperature perturbations around the mean ΔT).

ΔTn The mean departure of temperature at the mesonet station *i* (averaged over *t*) from the CEC station *n* temperature (*TairCECn*).

$\Delta Tn'$ Standard error of temperature differences around the mean departure (range of temperature perturbations around the mean ΔTn relative to a CEC station *n*).

The departure means and perturbations were computed at the 95 percent confidence interval. The subscripts in the equations have the following meanings:

i Station index (ID) of the mesonet station whose variables are correlated to variables at metars or CEC climate-zone stations.

z Temperature zone (1—5), within each study region (see Figures 20.A through 20.E in Appendix B), in which the correlations were established, that is, the zone where the mesonet stations (*i*) and metar stations were located (note that CEC climate-zone stations

are located throughout the domain and may or may not be in the temperature zone under consideration). The temperature zones were developed earlier in this project.

m Synthetic month (over years 2013—2015), that is, a representative June, July, August, and September for which the correlations were established.

s Accumulated solar radiation at representative stations in the temperature zone being considered. Accumulated solar radiation was categorized into ratio ranges of 1—33 percent, 34—66 percent, and 66—100 percent relative to the highest solar radiation value in each region (most often San Bernardino in the Los Angeles area and Livermore/Tracy in the San Francisco Bay Area). The goal was to group the correlations into various solar heating regimes as indicated by daily accumulated radiation from sunrise to 1500 PDT.

t The time interval for which the correlations were established—thus *t* can be the hour of the daily maximum temperature (e.g., 1500 PDT), the hour of the minimum (e.g., 0500 PDT), or all hours included (full 24 hours per day).

The same approach was applied to other variables including station pressure, wind speed, humidity, and accumulated solar radiation. Equations such as 7 and 8 served as the basis for developing finer-scale intraurban probabilistic microclimate zones. These equations describe the extent of intraurban climate variability that was not captured by the existing climate zones (for example, CEC 16 or 20 climate zones), the magnitude of such variability, and the potential improvements that can be attained if such finer-scale zones were adopted in energy planning and forecasting for the electric system, which is one of the stated goals of this project.

Figure 19.A through Figure 19.F represent an example from this analysis for the Los Angeles domain (similar analysis was done for other regions). These figures are essentially a graphic representation of the equations above (in this example, equation 8). Figure 19 A, C, and E depict the mean departure of temperature, that is ΔTn in equation 8, whereas Figure 19 B, D, and F showed the perturbations around these mean departures (standard error), that is, $\Delta Tn'$ in equation 8 at the 95 percent confidence interval. These examples are for departures and perturbations at the time of the daily maximum temperature for the synthetic month of June relative to three CEC stations in the Los Angeles domain, that is, KLGB (A and B), KBUR (C and D), and UCRC1 (E and F). These examples are only for accumulated solar radiation calculated in the range of 66—100 percent as defined above. For other solar radiation ranges, the information is provided in the companion datasets (see description of datasets at the end of this document).

The figures show the large intraurban temperature variability relative to any given CEC station currently used in planning or forecasting for the electric system (recall that these were based on observations). For example in Figure 19.A, the information provided suggests that relative to CEC station KLGB (Long Beach), the coastal stations could be up to 5.4°F (3°C) cooler on average at 1500 PDT (in June), but that the rest of the domain is much warmer, for example, up to 10.8°F (6°C) warmer in SFV, SGV, EB, and IE. The perturbations around the mean departures (Figure 19.B), in this case are relatively small (less than ±1.8°F (±1°C) throughout most of the domain) except for a few polygons near the higher elevations with perturbations of up to ±2.7°F (±1.5°C) and a single polygon at 8.1°F (4.5°C) (likely an outlier). The information on perturbations (standard error) defines the level of confidence in the computed departures (at CI 95 percent) and is also of value in probabilistic forecasting.

Figure 19: Mean Temperature Departures and Corresponding Standard Errors

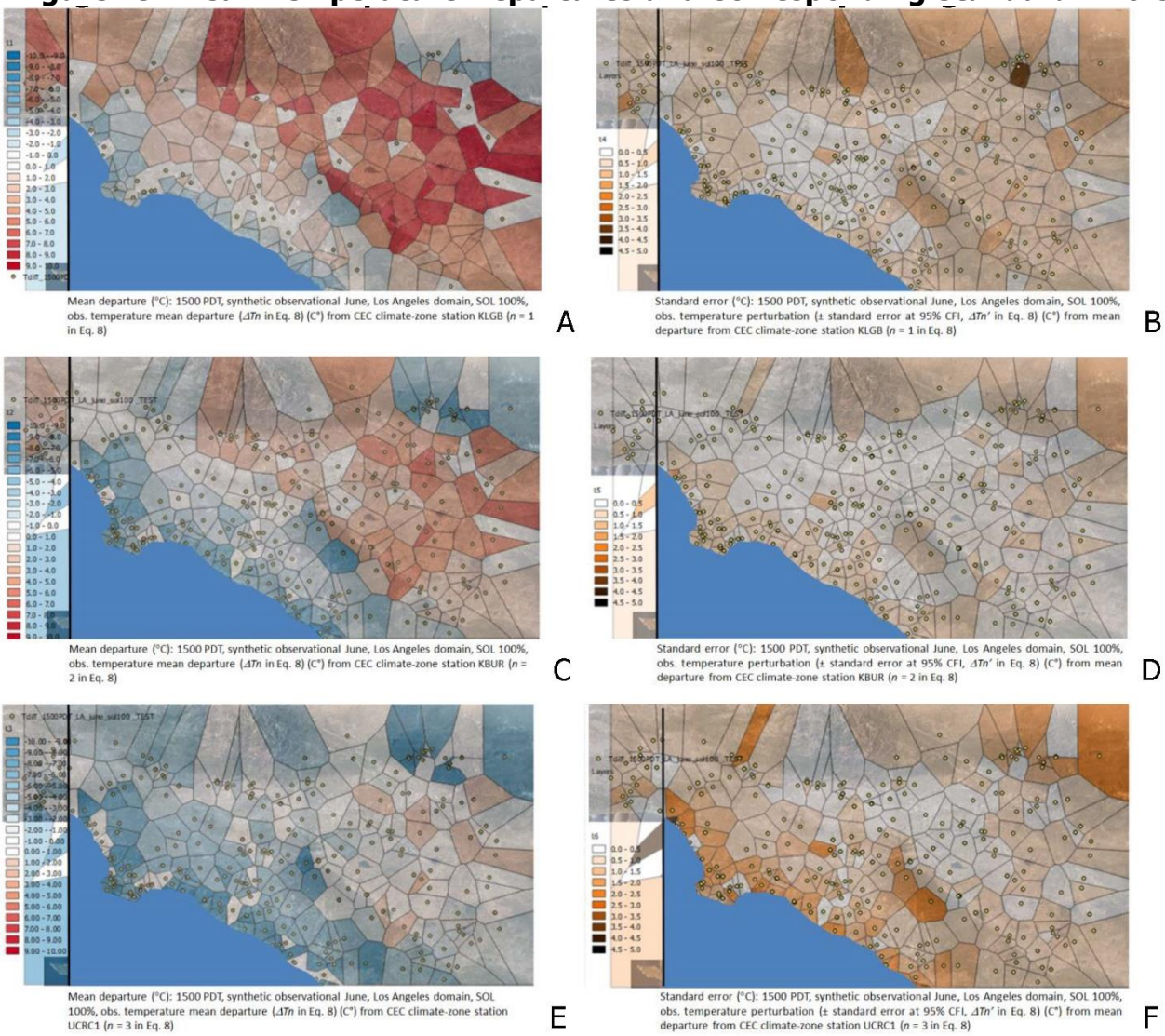

Departures and standard errors (°C) computed at mesonet stations relative to CEC climate zone stations, averaged for the month of June.

Source: Altostratus Inc.

Relative to KBUR (Burbank), see Figure 19.C, the coastal areas are up to 7.2°F (4°C) cooler and the inland-most areas (IE) are up to 9°F (5°C) warmer. The corresponding standard error field (Figure 19.D) shows relatively small values (small perturbations) of less than ±0.9°F (±0.5°C) throughout most of the domain, except for a few polygons near the coast and the higher elevations where the perturbations reach up to ±1.8°F (±1°C).

Relative to UCRC1 (UC Riverside), as seen in Figure 19.E, most of the domain is either similar to or cooler, except for a few polygons in IE that are warmer. The coastal areas could be up to 9°F (5°C) cooler and the IE can be up to 5.4°F (3°C) warmer. The standard error (Figure 19.F) is relatively low in the domain, in the range of ±0.9—1.8°F (±0.5—1°C), except for a few areas near the coastline and near the higher elevations where it could be as high as ±2.7°F (±1.5°C).

Based on this and similar analysis for other time periods, stations, and regions, the spatial properties of intraurban variability in temperature was defined. This exercise was repeated for every month, CEC station, solar radiation range, domain, and time period. Because of the large number of figures and data files, they are not included in this report but, rather, in the appendixes.

A large number of figures can be generated to depict the various combinations of solar radiation ranges, metar handshake points and CEC reference stations, synthetic months, times of day, hourly averages, mean departures of the variables, perturbations around the mean (standard error), and so on. To keep the discussion relatively compact, the following sections present results relative to only one CEC reference station per domain (KLGB for Los Angeles region and KOAK for the San Francisco Bay Area), provide only mean temperature departures from the CEC climate-zone stations (perturbations are provided in the appendixes), show correlations only for solar radiation range of 67—100 percent, and only for hours 0500 and 1500 PDT (that is, at the times near the minima and maxima). All times, CEC stations reference points and metars, solar radiation ranges, and metrics not shown here are included in the companion datasets.

Thus, while all-hours averages were used in Section 3.2.5 as examples for comparing inter-zone and intra-zones variabilities, in the following sections the intraurban variations are discussed for the averages near the times of temperature minima and maxima.

Departures at Time of Nighttime Minimum

Figure 20.A through Figure 20.H depict the mean departures near the time of the daily minimum temperature relative to CEC station KLGB (for Los Angeles region) and relative to CEC station KOAK (for the San Francisco Bay Area). In the Los Angeles region (Figure 20.A through Figure 20.D), the range of mean temperature departures from CEC climate zone station KLGB was -16.3°F to +3.1°F (-9.09°C to +1.75°C) in synthetic observational June, from -13.4°F to +3.9°F (-7.45°C to +2.20°C) in July, from -16.1°F to +4.6°F (-8.97°C to +2.55°C) in August, and from -15.8°F to +3.8°F (-8.80°C to +2.12°C) in September. Thus the across-region temperature range was 19.5°F, 17.3°F, 20.7°F, and 19.6°F (10.84°C, 9.65°C, 11.52°C, and 10.92°C) in synthetic observational June, July, August, and September, respectively. In the figures, it is evident that no particular spatial pattern exists (at the time of the minimum) across these months. For example, there is no contrast between the western and eastern parts of the region, nor in areas such as SFV or SGV.

In the San Francisco Bay Area (Figure 20.E through Figure 20.H), the range of mean temperature departures from CEC climate zone station KOAK was from -6.4°F to +5.6°F (-3.56°C to +3.12°C) in synthetic June, from -7°F to +8.7°F (-3.89°C to +4.83°C) in July, from -8°F to +4.7°F (-4.49°C to +2.65°C) in August, and from -6.8°F to +1.8°F (-3.82°C to +1.00°C) in September. Thus the across-region temperature range was 12°F, 15.7°F, 12.8°F, and 8.6°F (6.68°C, 8.72°C, 7.14°C, and 4.82°C) in synthetic June, July, August, and September, respectively. As seen in the figures, the areas surrounding the bay were generally warmer than areas to the southwest of the domain (coast) and east of the Richmond, Berkeley, and Oakland Hills, which was expected around the time of nighttime lows.

Figure 20: Current-Climate Mean Departures in Temperature Near Time of Daily Minimum Temperature

Mean departure: 0500 PDT, synthetic observational June, Los Angeles domain, SOL 100%, obs. temperature mean departure (ΔTn in Eq. 8) (°C) from CEC climate-zone station KLGB (n = 1 in Eq. 8)

A

Mean departure: 0500 PDT, synthetic observational July, Los Angeles domain, SOL 100%, obs. temperature mean departure (ΔTn in Eq. 8) (°C) from CEC climate-zone station KLGB (n = 1 in Eq. 8)

B

Mean departure: 0500 PDT, synthetic observational August, Los Angeles domain, SOL 100%, obs. temperature mean departure (ΔTn in Eq. 8) (°C) from CEC climate-zone station KLGB (n = 1 in Eq. 8)

C

Mean departure: 0500 PDT, synthetic observational September, Los Angeles domain, SOL 100%, obs. temperature mean departure (ΔTn in Eq. 8) (°C) from CEC climate-zone station KLGB (n = 1 in Eq. 8)

D

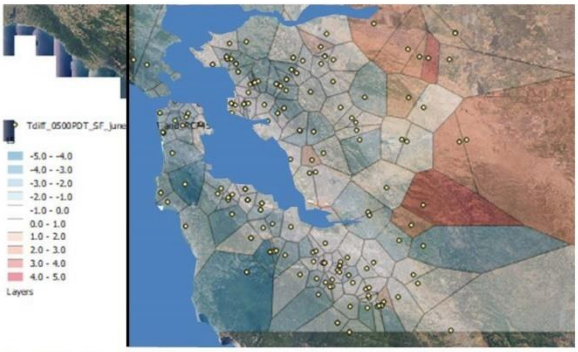

Mean departure: 0500 PDT, synthetic observational June, SFBA domain, SOL 100%, obs. temperature mean departure (ΔTn in Eq. 8) (°C) from CEC climate-zone station KOAK (n = 1 in Eq. 8)

E

Mean departure: 0500 PDT, synthetic observational July, SFBA domain, SOL 100%, obs. temperature mean departure (ΔTn in Eq. 8) (°C) from CEC climate-zone station KOAK (n = 1 in Eq. 8)

F

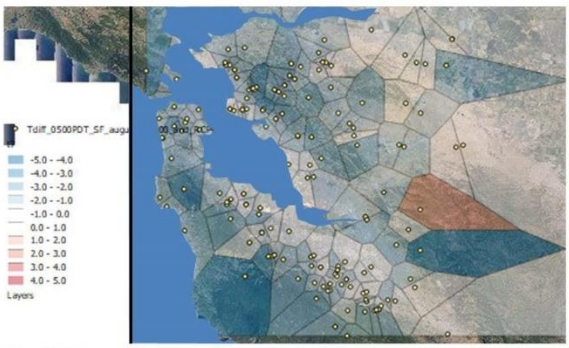

Mean departure: 0500 PDT, synthetic observational August, SFBA domain, SOL 100%, obs. temperature mean departure (ΔTn in Eq. 8) (°C) from CEC climate-zone station KOAK (n = 1 in Eq. 8)

G

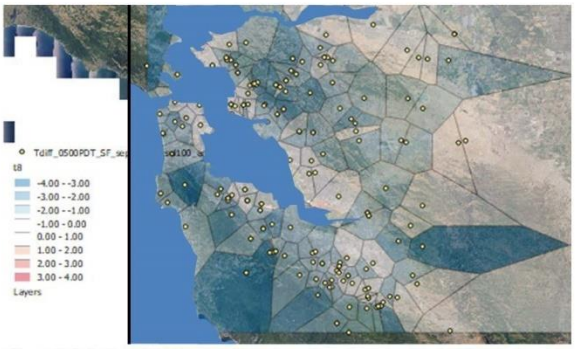

Mean departure: 0500 PDT, synthetic observational September, SFBA domain, SOL 100%, obs. temperature mean departure (ΔTn in Eq. 8) (°C) from CEC climate-zone station KOAK (n = 1 in Eq. 8)

H

Departures (°C) from stations KLGB and KOAK for the Los Angeles region and San Francisco Bay Area, respectively, averaged for June, July, August, and September.

Source: Altostratus Inc.

Departures at Time of Daytime Maximum

Figure 21.A through Figure 21.H depict the mean departures near the time of the daily maximum temperature. As before, the examples shown are for synthetic observational months in each region (Los Angeles and San Francisco Bay Area) only for accumulated solar radiation 67 percent—100 percent and relative to only one CEC climate-zone station (KLGB for Los Angeles region and KOAK for San Francisco Bay Area). All other times and conditions are provided in the appendixes.

In the Los Angeles region (Figure 21.A through Figure 21.D), the range of mean temperature departures from CEC climate zone station KLGB is -9.1°F to +17°F (-5.07°C to +9.48°C) in synthetic observational June, -9.9°F to +16.4°F (-5.53°C to +9.16°C) in July, --11°F to +15.1°F (-6.15°C to +8.43°C) in August, and -13°F to +12.8°F (-7.24°C to +7.15°C) in September. Thus, the across-region temperature range is 26.1°F, 26.4°F, 26.2°F, and 25.8°F (14.55°C, 14.69°C, 14.58°C, and 14.33°C) in synthetic June, July, August, and September, respectively. These ranges are notably larger than the ones at the time of the temperature minimum (discussed above). In general, the range at 1500 PDT is roughly 7.2°F (4°C) larger than at 0500 PDT. The figures also indicate that a spatial pattern exists in which the contrast between the west and east basins is considerable and much more demarcated. In addition to the fact that the IE is substantially warmer than the coastal and quasi-coastal areas in the west basin, the SFV and SGV also are much warmer than their surroundings. Areas in the central parts of the IE are generally cooler than areas to the north, east, and south parts of IE. Another observation is that the range (~26.1°F (~14.5°C)) across the region is relatively unchanged for all months, regardless of the lower and upper bounds. In other words, the range is shifted up or down from one month to another (at 1500 PDT), but is relatively unchanged.

In the San Francisco Bay Area (Figure 21.E through Figure 21.H), the range of mean temperature departures from CEC climate zone station KOAK is -11.9°F to +19.9°F (-6.65°C to +11.1°C) in synthetic June, -11.5°F to +22.8°F (-6.42°C to +12.7°C) in July, -9.8°F to +18.5°F (-5.46°C to +10.29°C) in August, and -10.1°F to +13.6°F (-5.65°C to +7.56°C) in September. Thus, the across-region temperature range is 31.9°F, 34.4°F, 28.3°F, and 23.7°F (17.75°C, 19.12°C, 15.75°C, and 13.21°C) in synthetic observational June, July, August, and September, respectively. These ranges are more than double those at 0500 PDT (discussed above). As seen in the figures, the reverse of the 0500 PDT pattern is true, that is, the areas around the bay are coolest than other areas in the domain (again, this is as expected for the time of maximum temperatures). The spatial pattern is relatively similar across the four months, in which the warmest areas are found in Palo Alto, southwest Santa Clara Valley, Pittsburg–Discovery Bay, East Concord–Walnut Creek, Dublin-Livermore, and Tracy-Manteca.

Figure 21: Current-Climate Mean Departures in Temperature Near Time of Daily Maximum Temperature

Mean departure: 1500 PDT, synthetic observational June, Los Angeles domain, SOL 100%, obs. temperature mean departure (ΔTn in Eq. 8) (°C) from CEC climate-zone station KLGB (n = 1 in Eq. 8)

A

Mean departure: 1500 PDT, synthetic observational July, Los Angeles domain, SOL 100%, obs. temperature mean departure (ΔTn in Eq. 8) (°C) from CEC climate-zone station KLGB (n = 1 in Eq. 8)

B

Mean departure: 1500 PDT, synthetic observational August, Los Angeles domain, SOL 100%, obs. temperature mean departure (ΔTn in Eq. 8) (°C) from CEC climate-zone station KLGB (n = 1 in Eq. 8)

C

Mean departure: 1500 PDT, synthetic observational September, Los Angeles domain, SOL 100%, obs. temperature mean departure (ΔTn in Eq. 8) (°C) from CEC climate-zone station KLGB (n = 1 in Eq. 8)

D

Mean departure: 1500 PDT, synthetic observational June, SFBA domain, SOL 100%, obs. temperature mean departure (ΔTn in Eq. 8) (°C) from CEC climate-zone station KOAK (n = 1 in Eq. 8)

E

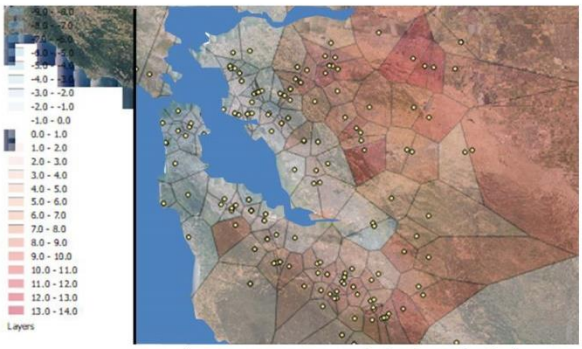

Mean departure: 1500 PDT, synthetic observational July, SFBA domain, SOL 100%, obs. temperature mean departure (ΔTn in Eq. 8) (°C) from CEC climate-zone station KOAK (n = 1 in Eq. 8)

F

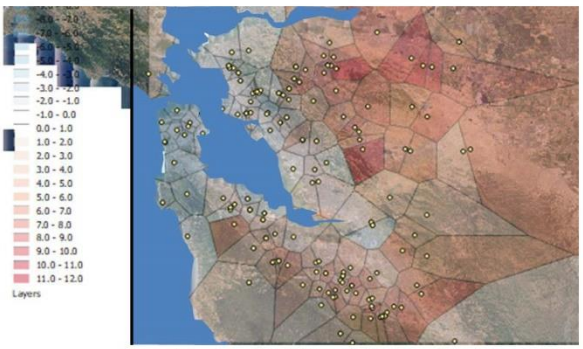

Mean departure: 1500 PDT, synthetic observational August, SFBA domain, SOL 100%, obs. temperature mean departure (ΔTn in Eq. 8) (°C) from CEC climate-zone station KOAK (n = 1 in Eq. 8)

G

Mean departure: 1500 PDT, synthetic observational September, SFBA domain, SOL 100%, obs. temperature mean departure (ΔTn in Eq. 8) (°C) from CEC climate-zone station KOAK (n = 1 in Eq. 2)

H

Temperature departure from stations KLGB and KOAK for the Los Angeles region and San Francisco Bay Area, respectively, averaged for June, July, August, and September.

Source: Altostratus Inc.

Population-Weighted Departures at Time of Daytime Maximum

Population-weighted mean departures at the time of the daily maximum were evaluated for the current climate (as well as future climates as will be discussed later). For the current climate, samples from the analysis are shown in Figure 22 (all other periods are included in the appendixes).

The top two figures show the population-weighted departures for the Los Angeles region and the bottom two for San Francisco Bay Area. Figures at left are for synthetic June and at right for synthetic August (as examples). Thus, Figure 22.A is to be compared to Figure 20.A, Figure 22.B compared to Figure 20.C, Figure 22.C compared to Figure 21.E, and Figure 22.D compared to Figure 21.G. Based on these comparisons, the following can be observed.

In the Los Angeles region, the nonweighted departures in temperature are such that the IE, especially its northern, eastern, and southern parts, is distinctively much warmer than the rest of the domain (Figure 21.A and Figure 21.C). The eastern basin is clearly demarcated from the rest of the domain. The SFV and SGV areas also are warmer than their surroundings. On the other hand, the population-weighted temperature departures are such that the warmest areas in IE shift north toward the hills, that is, to San Bernardino, as well as to other areas near the foothills including SGV, Glendale, Pasadena, and SFV (Figure 22.A and Figure 22.B). In addition, downtown Los Angeles also becomes a warmer area than its surroundings, unlike in the nonweighted departures.

In the San Francisco Bay Area, and except for cities closer to the central valley, such as Stockton and Tracy, the population-weighted departures in temperature are generally similar in pattern to the nonweighted departures. In both cases, the warmest areas include southwest and west Santa Clara valley, Pittsburgh-Antioch–Discovery Bay, and Dublin-Livermore.

Figure 22: Population-Weighted Mean Departures in Temperature

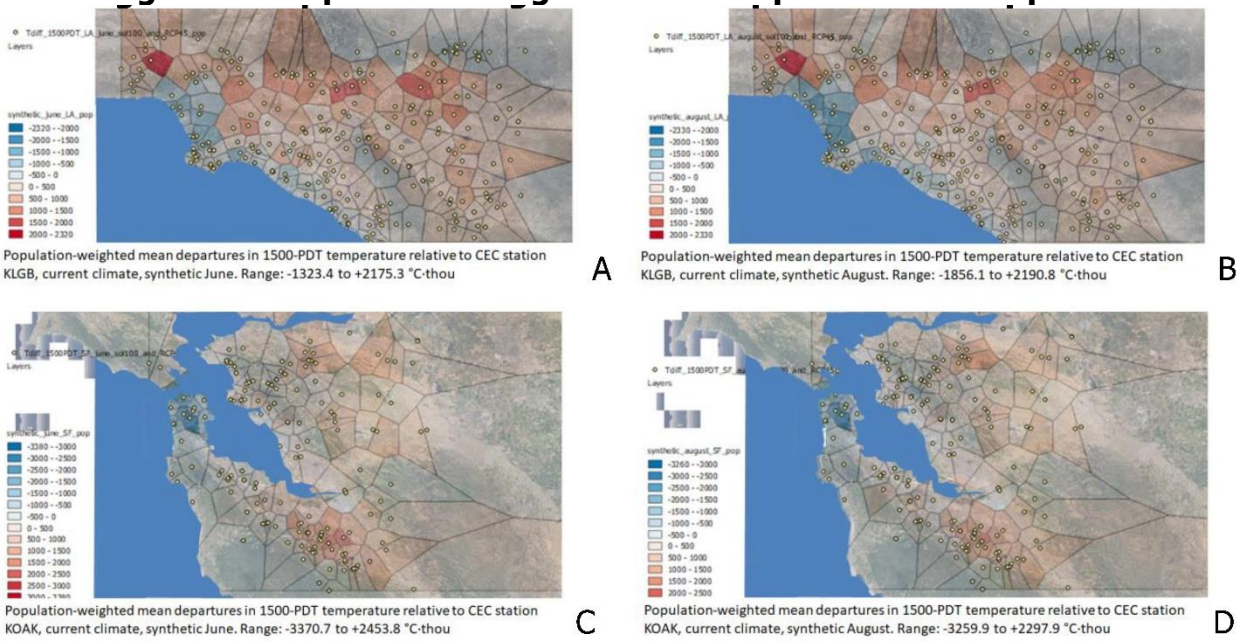

Population-weighted mean departures in 1500-PDT temperature relative to CEC station KLGB, current climate, synthetic June. Range: -1323.4 to +2175.3 °C·thou

A

Population-weighted mean departures in 1500-PDT temperature relative to CEC station KLGB, current climate, synthetic August. Range: -1856.1 to +2190.8 °C·thou

B

Population-weighted mean departures in 1500-PDT temperature relative to CEC station KOAK, current climate, synthetic June. Range: -3370.7 to +2453.8 °C·thou

C

Population-weighted mean departures in 1500-PDT temperature relative to CEC station KOAK, current climate, synthetic August. Range: -3259.9 to +2297.9 °C·thou

D

Source: Altostratus Inc.

3.2.7.B Mean Departures from CEC Climate-Zone Stations in Future Climate

For future climates, equations 7 and 8 are modified by including an additional tendency term, as shown in equation 9, to develop probabilistic correlations at each metar and mesonet station in future conditions. This equation is for air temperature as the variable of interest (other variables are treated similarly).

$$Tair_{i,z,m,s,t} = \overline{TairCECn_{z,m,s,t}} + \overline{\Delta Tn_{i,z,m,s,t}} + \overline{\Delta Sn_{\iota,z,m,s,t}} + \Delta Tn'_{i,z,m,s,t} \qquad (9)$$

Thus, in equation 9, the term, ΔSn, is added to equation 8 (to account for future-climate changes in temperature) and is defined as the change in departure (from the mean) in future years (and RCP scenarios) relative to current climate at each station. This term is based on model, as discussed in Section 3.2.3—all other terms in the equation are based on observations. The term is obtained by running uWRF after downscaling the fields from CMPI5 CCSM4 model. The CCSM4 data were obtained from NCAR (Monaghan et al., 2014). The downscaling process is described elsewhere, in Taha (2017) and Taha et al. (2018).

Data files were generated for these equations and for each of the combinations under consideration in this study to create new microclimate (temperature) zones. Diagram 1, below, represents a file-naming scheme for datasets produced in this effort, and shows some of the possible combinations of data. Since this translates into a large number of files, equations, and figures, a small sample is included in this report as an example. Other figures corresponding to this section are provided in companion datasets A, B, and C.

Diagram 1: File-naming Scheme

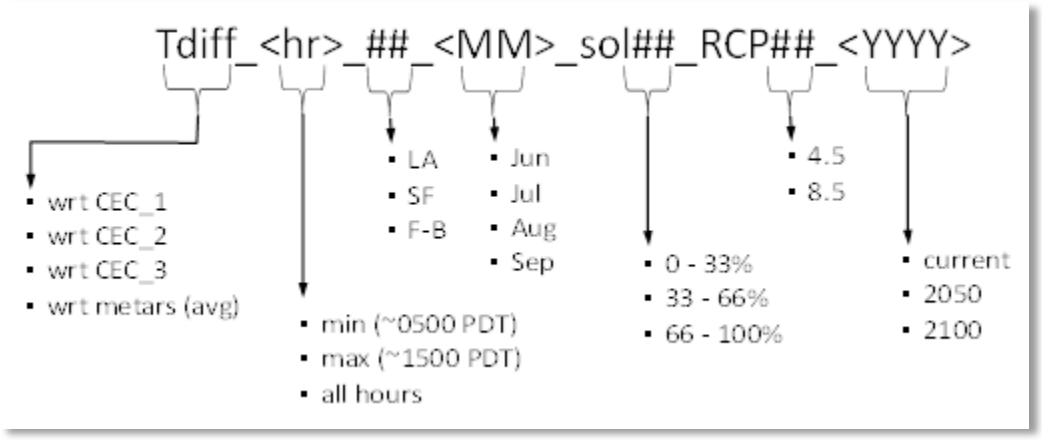

Departures at Time of Nighttime Minimum

The datasets corresponding to Diagram 1 for nighttime lows can be found in the appendixes.

Departures at the time of the daytime maximum

For reference, all figures related to the combinations shown in Diagram 1 at the times of the daily maximum are included in Appendix I and Appendix J. Here, only two examples are shown in Figure 23 (A through D), namely, for June and July, year 2050, RCP 4.5, for the Los Angeles (A, B) and San Francisco Bay Area domains (C, D).

These figures are depictions of Equation 9 as applied to the combinations highlighted in Diagram 1. To keep the discussion relatively compact, only the solar range 67 percent —100

percent is plotted in these figures (all other ranges are provided in the appendixes). In this section, the ranges of mean departures and spatial patterns in future climate are compared to those of current climate.

Table 16 and Table 17 summarize the ranges of mean departures (across the domain) relative to CEC climate zone stations (KLGB and KOAK) and for the conditions specified above. The tables also include a recap of current-climate conditions (shaded cells) for the sake of comparison with future conditions. To reiterate, the current-climate ranges are based on observational data, while future-climate ranges are based on observations and model results per equation 9.

Figure 23: Future-Climate Temperature Departures at Time of Daily Maximum

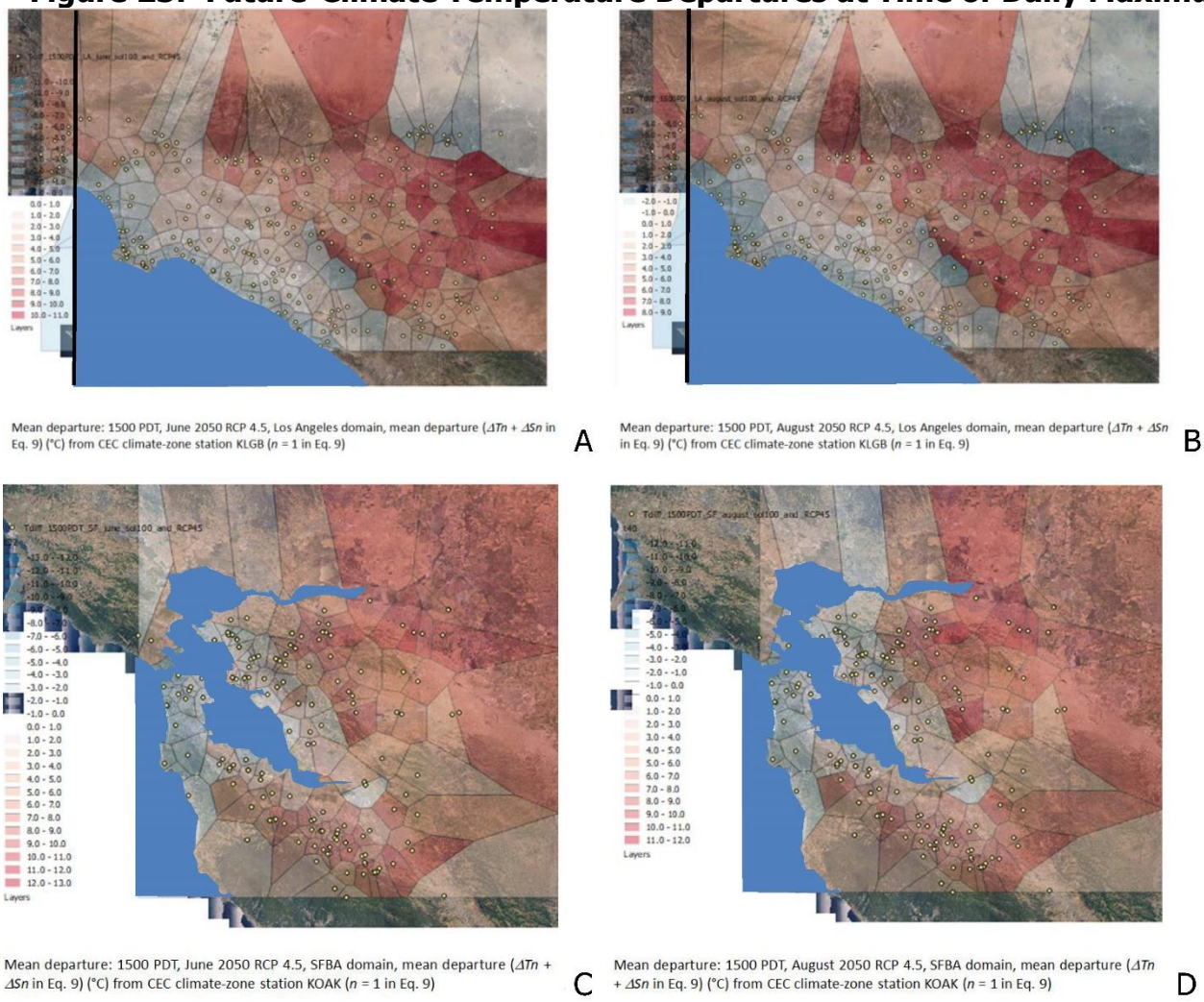

Mean departure: 1500 PDT, June 2050 RCP 4.5, Los Angeles domain, mean departure ($\Delta Tn + \Delta Sn$ in Eq. 9) (°C) from CEC climate-zone station KLGB (n = 1 in Eq. 9) A

Mean departure: 1500 PDT, August 2050 RCP 4.5, Los Angeles domain, mean departure ($\Delta Tn + \Delta Sn$ in Eq. 9) (°C) from CEC climate-zone station KLGB (n = 1 in Eq. 9) B

Mean departure: 1500 PDT, June 2050 RCP 4.5, SFBA domain, mean departure ($\Delta Tn + \Delta Sn$ in Eq. 9) (°C) from CEC climate-zone station KOAK (n = 1 in Eq. 9) C

Mean departure: 1500 PDT, August 2050 RCP 4.5, SFBA domain, mean departure ($\Delta Tn + \Delta Sn$ in Eq. 9) (°C) from CEC climate-zone station KOAK (n = 1 in Eq. 9) D

Source: Altostratus Inc.

For current climate, the range of mean temperature departures across the domain in the Los Angeles region (shaded cells in Table 16) is nearly constant—around 26.1°F (14.5°C) but is shifted up or down from one month to another. On the other hand, in the San Francisco Bay Area, the range across the domain (shaded cells in Table 17) actually varies considerably from one month to another in addition to shifting up or down. However, in the future climate in the Los Angeles region (Table 16), there is some notable variation in the ranges from one month to another, as well.

In the Los Angeles domain future climate, except for September (Table 16), the coolest mean departures in 2050, regardless of RCP scenario, are almost unchanged relative to current conditions (but note that this is relative departure, not absolute temperatures). For 2100 (including September), the coolest mean departures are pointedly smaller than those of current climate (smaller negative numbers), suggesting an increase in temperature minima by 2100, especially in the RCP 8.5 scenario. The warmest mean departures, on the other hand (including September), increase with year and RCP scenario, suggesting that at the times of the daily temperature peaks, it is the higher temperatures that are exacerbated further. This is in general agreement with findings by Taha (2017) that warmer weather exacerbates urban heat in California.

Table 16: Ranges of Mean Temperature Departures — Los Angeles Region Relative to CEC Climate Zone Station KLGB at 1500 PDT

Los Angeles region		Coolest mean departure (˚C)	Warmest mean departure (˚C)	Range (˚C) across domain
June	Current climate*	-5.07	+9.48	14.55
	2050 RCP 4.5	-5.06	+10.14	15.20
	2100 RCP 4.5	-4.55	+10.19	14.74
	2050 RCP 8.5	-5.09	+11.26	16.35
	2100 RCP 8.5	-2.61	+13.32	15.93
July	Current climate*	-5.53	+9.16	14.69
	2050 RCP 4.5	-5.35	+9.82	15.17
	2100 RCP 4.5	-4.96	+9.87	14.83
	2050 RCP 8.5	-5.31	+10.94	16.25
	2100 RCP 8.5	-2.91	+13.00	15.91
August	Current climate*	-6.15	+8.43	14.58
	2050 RCP 4.5	-6.12	+8.86	14.98
	2100 RCP 4.5	-5.61	+8.94	14.55
	2050 RCP 8.5	-6.15	+9.96	16.11
	2100 RCP 8.5	-3.67	+11.76	15.43
September	Current climate*	-7.24	+7.15	14.39
	2050 RCP 4.5	-6.22	+7.77	13.99
	2100 RCP 4.5	-6.63	+7.60	14.23
	2050 RCP 8.5	-5.93	+8.24	14.17
	2100 RCP 8.5	-3.95	+10.70	14.65

Relative to CEC climate zone station KLGB at 1500 hours Pacific daylight time.
***Current-climate is based on observational data only, that is, the synthetic months JJAS years 2013 – 2015 as discussed earlier. The future-climate scenarios are based both upon observations and modeling, as explained by Equation 9.**

Source: Altostratus Inc.

In future climate in the San Francisco Bay Area (Table 17), the ranges (across the domain) in years 2050 and 2100 and both RCP scenarios are consistently larger than the ranges of the corresponding months in current climate. The ranges monotonically increase in the order of 2050 RCP 4.5, 2100 RCP 4.5, 2050 RCP 8.5, and 2100 RCP 8.5. The coolest mean departures in the San Francisco Bay Area have no identifiable pattern of change—some increase, some decrease. The only consistent pattern is the smallest negative value in 2100 RCP 8.5, suggesting the largest increase in temperature minima under those conditions. The warmest departures increase monotonically, except for September, in the order of 2050 RCP 4.5, 2050 RCP 8.5, 2100 RCP 4.5, and 2100 RCP 8.5.

In terms of the spatial patterns, the following observations can be made (see Figure 23.A through Figure 23.D):

In the Los Angeles region, in general, there are variations at the fine scales (weather stations and polygons shown in the figures), such that some areas warm up more than others and there are variations in spatial patterns. However, some of the dominant features appear to be relatively consistent, for example in north, east, and south IE, the SGV, and the SFV, are consistently warmer than other parts of the domain (this can also be seen through the months of JJAS in Appendix I).

Similarly, in the San Francisco Bay Area, there also are spatial variations from one year and scenario to another, but the dominant features appear to be consistent: Palo Alto, southwest Santa Clara Valley, Pittsburg–Discovery Bay, East Concord–Walnut Creek, Dublin-Livermore, and Tracy-Manteca, are consistently warmer than other parts of the domain (this can also be seen in Appendix J).

Table 17: Ranges of Mean Temperature Departures — San Francisco Bay Area Region Relative to CEC Climate Zone Station KOAK at 1500 PDT

San Francisco Bay Area		Coolest mean departure (˚C)	Warmest mean departure (˚C)	Range (˚C) across domain
June	Current climate*	-6.65	+11.10	17.75
	2050 RCP 4.5	-5.60	+12.26	17.86
	2100 RCP 4.5	-6.11	+12.37	18.48
	2050 RCP 8.5	-7.17	+12.33	19.50
	2100 RCP 8.5	-4.77	+14.91	19.68
July	Current climate*	-6.42	+12.70	19.12
	2050 RCP 4.5	-5.60	+13.86	19.46
	2100 RCP 4.5	-6.10	+13.97	20.07
	2050 RCP 8.5	-7.07	+13.93	21.00
	2100 RCP 8.5	-4.76	+16.51	21.27
August	Current climate*	-5.46	+10.29	15.75
	2050 RCP 4.5	-4.54	+11.45	15.99
	2100 RCP 4.5	-5.04	+11.56	16.60
	2050 RCP 8.5	-6.02	+11.52	17.54
	2100 RCP 8.5	-3.70	+14.10	17.80
September	Current climate*	-5.65	+7.56	13.21
	2050 RCP 4.5	-4.61	+8.69	13.30
	2100 RCP 4.5	-5.10	+8.48	13.58
	2050 RCP 8.5	-6.16	+8.47	14.63
	2100 RCP 8.5	-3.75	+11.26	15.01

Relative to CEC climate zone station KLGB at 1500 hours Pacific daylight time.
***Current-climate is based on observational data only, that is, the synthetic months JJAS years 2013 – 2015 as discussed earlier. The future-climate scenarios are based both upon observations and modeling, as explained by Equation 9.**

Source: Altostratus Inc.

Population-Weighted Departures at Time of Daytime Maximum

Population-weighted mean departures at the time of the daily maximum were also evaluated for future climate scenarios, as shown in the following example figures (all other periods are included in Appendixes H and I). The examples in Figure 24 (A through D) are for year 2050 and RCP 4.5 only. These figures can be compared to Figure 23 (A through D), respectively.

The shifts in the spatial patterns caused by population-weighting are similar to those occurring during current climates. Thus, in the Los Angeles region, the nonweighted departures in temperature in 2050 RCP 4.5 are such that the northern, eastern, and southern parts of the IE are distinctively much warmer than the rest of the domain (Figure 23.A and Figure 23.B). The SFV and SGV areas also are warmer than their surroundings. However, the population-weighted temperature departures (Figure 24.A and Figure 24.B) are such that the warmest areas in IE shift north toward the foothills in San Bernardino, SGV, Glendale, Pasadena, and in SFV. Downtown Los Angeles and surrounding areas also become warmer than in the nonweighted departures. In the San Francisco Bay Area (Figure 24.C and Figure 24.D), the population-weighted departures in temperature are generally similar in pattern to the nonweighted departures. In both cases, the warmest areas include southwest and west Santa Clara valley, Pittsburgh-Antioch–Discovery Bay, and Dublin-Livermore.

Figure 24: Population-Weighted Mean Temperature Departures at Time of Daily Maximum in Future Climate

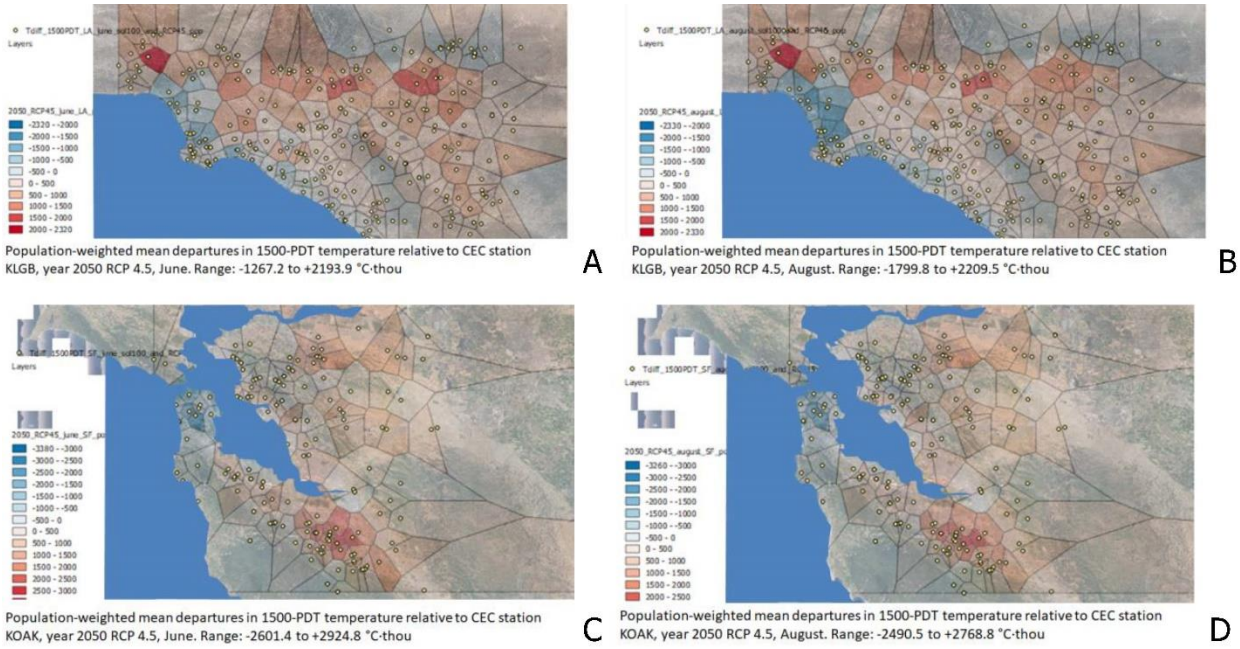

Population-weighted mean departures in 1500-PDT temperature relative to CEC station KLGB, year 2050 RCP 4.5, June. Range: -1267.2 to +2193.9 °C·thou

A

Population-weighted mean departures in 1500-PDT temperature relative to CEC station KLGB, year 2050 RCP 4.5, August. Range: -1799.8 to +2209.5 °C·thou

B

Population-weighted mean departures in 1500-PDT temperature relative to CEC station KOAK, year 2050 RCP 4.5, June. Range: -2601.4 to +2924.8 °C·thou

C

Population-weighted mean departures in 1500-PDT temperature relative to CEC station KOAK, year 2050 RCP 4.5, August. Range: -2490.5 to +2768.8 °C·thou

D

Source: Altostratus Inc.

Departures at All Hours

These can be found in the companion datasets.

CHAPTER 4:
Conclusions and Recommendations

This project demonstrated that improvements in meteorological model performance and the creation of probabilistic fine-scale micoclimate (temperature) zones that account for variations in intraurban microclimates can improve planning and forecasting for California's electric grid. Improved forecasting and planning would optimize the allocation of generating resources and increase the grid's resilience to short- and long-term climate variations. By extension, such improvements would also reduce greenhouse gas emissions and improve thermal environmental conditions.

Focusing on the Los Angeles region and the San Francisco Bay Area during summer months, the multi-faceted project did the following.

- Developed and evaluated a method to characterize intraurban microclimate variability in the context of climate forecasting for the electric system. The method also accounted for the effects of long-term changes in urban land use by developing the corresponding input to the microclimate model in addition to the dynamically downscaled meteorological fields for future years.
- Improved meteorological-model performance by applying study-modified and customized urban parameterizations and representations in the atmospheric and land-surface modules of the urbanized Weather Research and Forecasting (uWRF) model.
- Developed probabilistic fine-scale intraurban temperature zones as an enhancement to forecasting under current and future climates.

Project Results

Study results demonstrate that it is critical to account for the intraurban variability in microclimates, especially in urban areas, when forecasting and planning for the electric system.

- A comparison of the fine-scale temperature zones with the forecast climate zones currently used by the California Energy Commission in planning for the electric system and in building energy modeling showed that the intra-zone variability in temperature was considerable and could be several-fold larger than the inter-zone differences.
- Improvements to the uWRF model showed significant reduction in forecasting errors. Studies have shown that 1.8°F (1°C) of peak temperature is equivalent to approximately 0.5 to 1.0 Gigawatts of power. Thus, even a 0.9°F (0.5°C) reduction in forecasting error systemwide could translate to a reduction or reallocation of approximately 500 megawatts in generating capacity, the equivalent of one to three large power plants. With improved uWRF modeling, the project reduced temperature forecasting error up to 3.2°F (1.8°C) in the San Francisco Bay Area and up to 1.4°F (0.8°C) in the Los Angeles region.

- Simulations to develop microclimate zones for current and future conditions based on observational analysis and modeling suggest substantial intraurban variations in microclimate, as shown in Figure 25.

Figure 25: Proposed Temperature Zones Versus Current CEC Forecast Climate Zones

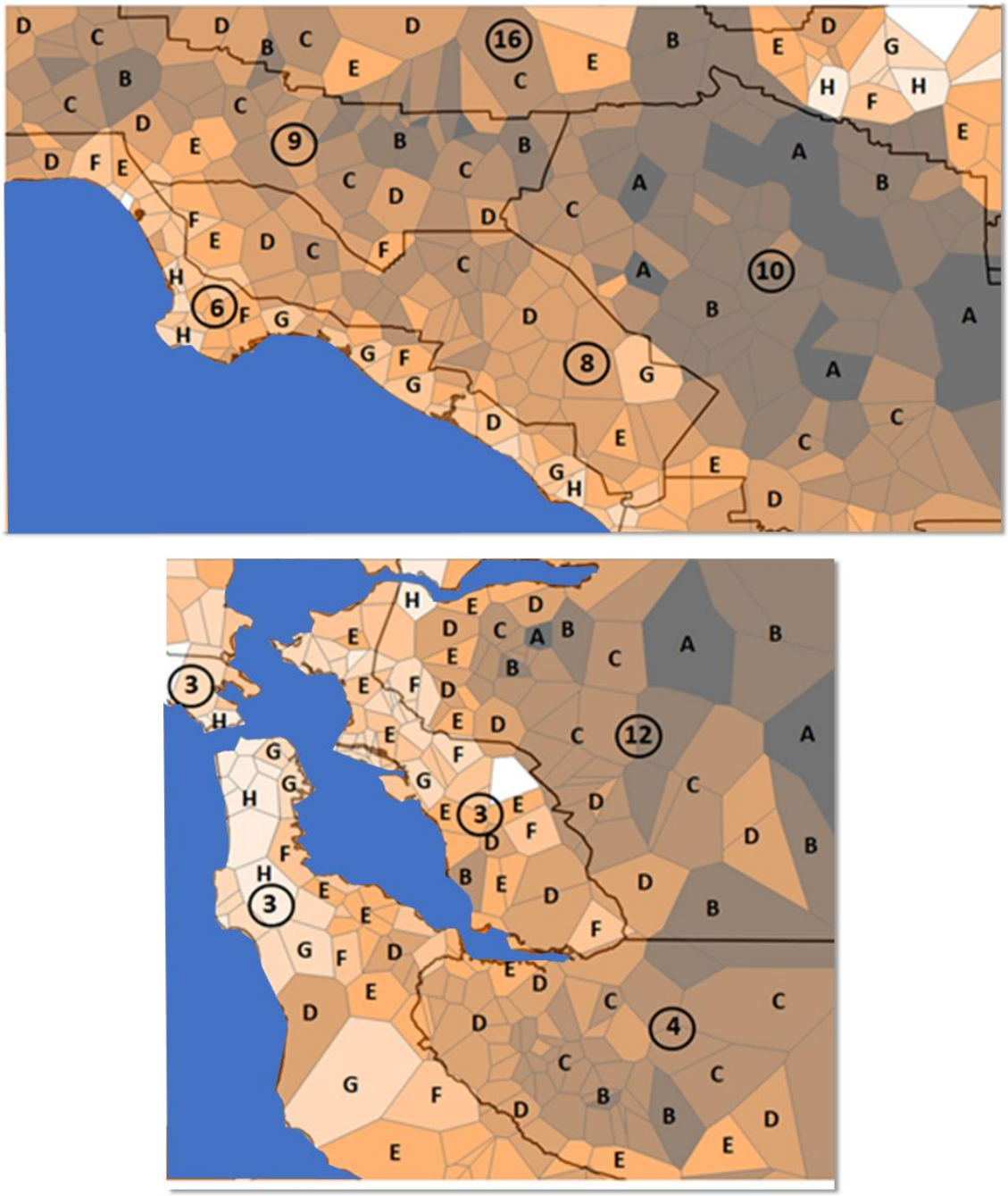

Proposed temperature zones are lettered; climate zones currently used for forecasting by the California Energy Commission are numbered. The top figure represents the Los Angeles region; the bottom figure, the San Francisco Bay Area. This example is for synthetic observational August all-hours averages, nonthreshold. The proposed fine-scale zones are structured at intervals equal to the trans-boundary (across boundary) temperature differences in corresponding climate zone weather files (all-hour averaged temperatures from climate zone file for the month).

Source: Altostratus Inc

Project Recommendations

Before 2016, forecasting and planning for California's electric system are based on 16 climate zones identified in 1995 as a foundation for California's building energy standards. After 2016, the electricity demand forecast geography changed to 20 zones. Those climate zones do not account for the multitude of microclimates that exist within them and for the fine-scale variations and different energy needs in these microclimates. Current practice in energy forecasting has not considered the effects of urban land use, localized heat or cool islands, and intraurban heat transport, or their respective changes in the future, in planning for the electric grid. Nor are these effects considered in current building energy modeling practices. The advent of increased computing power, improved and more accurate fine-resolution atmospheric and land-surface models, and higher density of observational weather networks, as well as powerful data management and processing tools, eliminate the restrictions for climate zones to be large and contiguous and offer more precise data for electricity forecasting and planning.

Based on the results from modeling and observational analysis, the project recommends that:

- Current climate-zone boundaries be redrawn or that fine-scale zones (such as those shown in Figure 25) be created and adopted, using the proposed method, in planning for the electric system and in building energy modeling and calculations.
- Climate forecasting for electricity, as well as for energy modeling, be done at finer scales and at the site-specific resolutions that improved models and new technologies allow.

Incorporating California's multiple intraurban microclimates and using improved modeling will provide more accurate and precise weather data for forecasting and planning for electricity that will optimize allocations for the electric grid and increase its resilience to short- and long-term climate variations. By extension, such improvements would also reduce greenhouse gas emissions and improve thermal environmental conditions.

The method developed in this study can be used to create microclimate zones at different thresholds, spatial resolutions, or zone boundaries as deemed suitable for specific applications.

In follow-up efforts, the zones developed in this study can serve as the basis to create fine-scale, site-specific weather files for input to energy modeling and calculations of current and future climates for the other seasons of the year, for full years, and for additional geographical areas in California.

LIST OF ACRONYMS

Term/Acronym	Definition
AFB	Air Force base (radiosonde)
AGL	above ground level
AMSL	above mean sea level
BAAQMD	Bay Area Air Quality Management District
CDD	cooling degree-days
CDH	cooling degree-hours
CEC	California Energy Commission
CIMIS	California Irrigation Management Information System
CWOP	Citizen Weather Observing Program
CZ	climate zone
DH/day	degree-hours per day
DHPD	degree-hours per day (in figures/graphs)
EB	east basin
GIS	geographical information system
IE	Inland Empire
IQR	inter quantile range (defined specifically for the discussions)
JJAS	June, July, August, and September
LAX	Los Angeles International Airport (radiosonde)
LST	local standard time
LULC	land-use/land-cover
MADIS	Meteorological Assimilation Data Ingest System
METSTAT	meteorological statistical model performance evaluation tool
METAR	METeorological Aerodrome Reports
MPE	model performance evaluation
NCAR	U.S. National Center for Atmospheric Research
NCEP	National Centers for Environmental Prediction
NLCD	national land cover data
NOAA	National Oceanic and Atmospheric Administration
OAK	Oakland International Airport (radiosonde)
PDT	Pacific Daylight Saving Time
PG&E	Pacific Gas and Electric
QGIS	Quantum Geographical Information System

Term/Acronym	Definition
SCAQMD	South Coast Air Quality Management District
SDG&E	San Diego Gas & Electric
SFO	San Francisco International Airport (radiosonde)
SFV	San Fernando Valley
SGV	San Gabriel Valley
SJVAPCD	San Joaquin Valley Air Pollution Control District
UCI	urban cool island
UHI	urban heat island
uWRF	urbanized versions of WRF
WB	west basin
WMO	World Meteorological Organization
WRF	Weather Research and Forecasting model

REFERENCES

Alfaro, E., Gershunov, A., Cayan, D., Steinemann, A., Pierce, D., and Barnett, T. 2004. A method for prediction of California summer air surface temperature, EOS Transactions AGU, 85, 553–558 doi:10.1029/2004EO510001

Alfaro, E., Gershunov, A., and Cayan, D. 2006. Prediction of summer maximum and minimum temperature over the central and western United States: The role of soil moisture and sea surface temperature. Journal of Climate 19, 1407-1421, doi: 10.1175/JCLI3665.1

Anderson, J.R., Hardy, E.E., Roach, J.T., and Witmer, R.E. 2001. A land use and land cover classification system for use with remote sensor data. USGS Professional Paper 964, U.S. Government Printing Office, Washington, DC.

Ban-Weiss, G.A., Woods, J., Millstein, D., and Levinson, R. 2015. Using remote sensing to quantify albedo of roofs in seven California cities, Part 2: Results and application to climate modeling. Solar Energy, 115, 791-800, doi: 10.1016/j.solener.2014.10.041.

Bierwagen, B.G., Theobald, D.M., Pyke, C.R., Choate, A., Groth, P., Thomas, J.V., and Morefield, P. 2010. National housing and impervious surface scenarios for integrated climate impacts assessments. PNAS 107, 20887-20892.

Bruyere, C., Done, J.M., Holland, G.J., and Fredrick, S. 2014. Bias corrections of global models for regional climate simulations of high-impact weather. Climate Dynamics, 43, 1847-1856, doi: 10.1007/s00382-013-2011-6

California Energy Commission (CEC). 2017. Building Climate Zones, California 2017. http://www.energy.ca.gov/maps/renewable/building_climate_zones.html

California Independent System Operator Corporation (CAISO) 2007. Summer loads and resources operations assessments

Chen, F., Kusaka, H., Bornstein, R., Ching, J., Grimmond, CSB, Grossman-Clarke, S., Loridan, T., Manning, K., Martilli, A., Miao, S., Sailor, D., Salamanca, F., Taha, H., Tewari, M., Wang, X., Wyszogrodzki, A., and Zhang, C. 2010. The integrated WRF/urban modeling system: development, evaluation, and applications to urban environmental problems. International Journal of Climatology doi:10.1002/joc.2158.

Ching, J., Brown, M., Burian, S., Chen, F., Cionco, R., Hanna, A., Hultgren, T., McPherson, T., Sailor, D., Taha, H., and Williams, D. 2009. National urban database and access portal tool, NUDAPT. Bulletin of the American Meteorological Society doi:10.1175/2009BAMS2675.1

Daly, C., Halbleib, M., Smith, J.I., Gibson, W.P., Doggett, M.K., Taylor, G.H., Vurtis, J., and Pasteris, P.P. 2008. Physiographically sensitive mapping of climatological temperature and precipitation across the conterminous United States. International Journal of Climatology doi: 10.1002/joc.1688

Davis, T.D., Altalo, M.A., and Hale, M. 2004. The economic benefits of improving weather and load forecasts for the electric utility strategic and operational management. cirrus.ucsd.edu/~pierce/calenergy/deliv3.pdf

Dias, D.F., Cayan, D.R., Gershunov, A. 2018. Statistical prediction of minimum and maximum air temperature in California and western North America. California's Fourth Climate Change Assessment, California Energy Commission. Publication Number: CCCA4-CEC-2018-011

Garcia-Cerrutti, Miguel, Tom Gorin, Chris Kavalec, and Lynn Marshall. 2010. Revised Short-Term (2010-2012) Peak Demand Forecast Draft Staff Report. California Energy Commission, Electricity Supply Analysis Division. Publication Number: CEC-200-2010-011-SD. https://www.energy.ca.gov/2010publications/CEC-200-2010-011/CEC-200-2010-011-SD.pdf

Georgescu, M. 2015. Challenges associated with adaptation to future urban expansion. Journal of Climate 28, 2544-2563.

Herter K, McAuliffe P, Rosenfeld A, 2005. Observed temperature effects on hourly residential electric load reduction in response to an experimental critical peak pricing tariff. Lawrence Berkeley National Laboratory Report LBNL 58965, Berkeley, California.

Kavalec, C., and Gorin, T. 2009. California energy demand 2010–2020, adopted forecast. California Energy Commission. CEC 200-2009-012-CMF. https://www.energy.ca.gov/2009publications/CEC-200-2009-012/CEC-200-2009-012-CMF.PDF

Kistler, R., Kalnay, E., Collins, W., et al. 2001. The NCEP-NCAR 50-year reanalysis: Monthly means CDROM and documentation. Bulletin of the American Meteorological Society, 82, 247-267

Lebassi-Habtezion, B., Gonzalez, J., and Bornstein, R.D. 2011. Modeled large-scale warming impacts on summer California coastal-cooling trends. Journal of Geophysical Research – Atmospheres, 116 D20, doi: 10.1029/2011JD015759.

Livneh, B., Bohn, T.J., Pierce, D.W., Munoz-Arriola, F., Nijssen, B., Vose, R., Cayan, D.R., and Brekke, L. 2015. A spatially comprehensive, meteorological data set for Mexico, the U.S., and southern Canada (NCEI Accession 0129374). Version 1.1. NOAA National Centers for Environmental Information. Dataset. doi:10.7289/V5X34VF6

Loh, W.-Y. 2008. Classification and regression tree methods, in F. Ruggeri, R. Kenett and F.W. Faltin (eds.), Encyclopedia of Statistics in Quality and Reliability, Wiley, Chichester, UK, pp. 315–323. http://www.stat.wisc.edu/~loh/treeprogs/guide/eqr.pdf.

Martilli, A., Clappier, A., and Rotach, M.W. 2002. An urban surface exchange parameterization for mesoscale models. Boundary-Layer Meteorology, 104, 261-304

Monaghan, A.J., Steinhoff, D.F., Bruyere, C.L., and Yates, D. 2014. NCAR CESM global bias-corrected CMIP5 output to support WRF/MPAS research. Research Data Archive at the

National Center for Atmospheric Research, Computational and Information Systems Laboratory, doi: 10.5065/D6DJ5CN4, last accessed 01/16/2019.

Multi-Resolution Land-Characteristics Consortium (MRLC). 2006. National Land Cover Databases. http://www.mrlc.gov

National Oceanic and Atmospheric Administration. 2015. CM2 and CMIP5 models. https://www.ncdc.noaa.gov/data-access/model-data/model-datasets/climate-prediction

OEHHA (Office of Environmental Health Hazard Assessment). 2013. California Communities Environmental Health Screening Tool, Version 1 (CalEnviroScreen 1.0) Guidance and Screening Tool. Office of Environmental Health Hazard Assessment Report, Sacramento, California, April 2013, 116 pp.

Pierce, D.W., Kalansky, J.F., and Cayan, D.R. 2018. Climate, Drought, and Sea Level Rise Scenarios for the Fourth California Climate Assessment. California's Fourth Climate Change Assessment, California Energy Commission. Publication Number: CNRA-CEC-2018-006.

Skamarock, W., Klemp, J., Dudhia, J. 2008. A description of the Advanced Research WRF. NCAR Technical Note NCAR/TN-475+STR, National Center for Atmospheric Research, Boulder, Colorado.

Sleeter, B.M., Liu, J., Daniel, C., Frid, L., and Zhu, Z. 2015. An integrated approach to modeling changes in land use, land cover, and disturbance and their impact on ecosystem carbon dynamics: a case study in the Sierra Nevada Mountains of California. AIMS Environment Science, 2, 577–606, doi:10.3934/environsci.2015.3.577

Suckling, E.B., and Smith, L.A. 2013. An Evaluation of Decadal Probability Forecasts from State-of-the-Art Climate Models. Journal of Climate. 26, 9334-9347 doi: 10.1175/JCLI-D-12-00485.1

Sun, F., Walton, D.B., and Hall, A. 2015. A hybrid dynamical-statistical downscaling technique: Part II – End of century warming projections predict a new climate state in the Los Angeles region. Journal of Climate, 28, 4618–4636.

Taha, H. 2017. Characterization of urban heat and exacerbation: Development of a heat island index for California. Climate 5, 59. doi:10.3390/cli5030059.

Taha, H. 2015. Cool cities: counteracting potential climate change and its health impacts. Current Climate Change Reports, doi: 10.1007/s40641-015-0019-1.

Taha, H. 2013. "Meteorological, emissions, and air-quality modeling of heat-island mitigation: Recent findings for California, U.S.A.", International Journal of Low Carbon Technologies, doi: 10.1093/ijlct/ctt010

Taha, H. 2011. Multi-episodic and seasonal meteorological, air-quality, and emission-equivalence impacts of heat island control and evaluation of the potential atmospheric effects of urban solar photovoltaic arrays. Final report prepared by Altostratus Inc. for

the California Energy Commission (CEC), PIER Environmental Research Program, Sacramento, California. http://www.energy.ca.gov/2013publications/CEC-500-2013-061/CEC-500-2013-061.pdf

Taha, H. 2008a. Meso-urban meteorological and photochemical modeling of heat island mitigation. Atmospheric Environment, 42, 8795-8809 doi:10.1016/j.atmosenv.2008.06.036.

Taha, H. 2008b. Episodic performance and sensitivity of the urbanized MM5 (uMM5) to perturbations in surface properties in Houston, TX. Boundary-Layer Meteorology 127, 193-218. doi:10.1007/s10546-007-9258-6.

Taha, H. 2001. Potential impacts of climate change on tropospheric ozone in California: A preliminary assessment of the Los Angeles basin and the Sacramento valley. Lawrence Berkeley National Laboratory Report LBNL-46695, http://escholarship.org/uc/item/5s41x609

Taha, H., Levinson, R., Mohegh, A., Gilbert, H., Ban-Weiss, G., and Chen, S. 2018. "Air temperature response to neighborhood-scale variations in albedo and canopy cover in the real world: Fine-resolution meteorological modeling and mobile temperature observations in the Los Angeles climate archipelago". Climate, 6, 53, doi: 10.3390/cli6020053.

Taha, H., and Freed, T. 2015. Creating and mapping an urban heat island index for California. Report prepared by Altostratus Inc. for the California Environmental Protection Agency, Sacramento, California (April 2015). www.calepa.ca.gov/UrbanHeat/Report/Report.pdf

Tesche, T.W., McNally, D.E., Emery, C.A., and Tai, E. 2001. Evaluation of the MM5 model over the Midwestern U.S. for three 8-hour oxidant episodes, Prepared for the Kansas City Ozone Technical Workgroup. Alpine Geophysics LLC and Environ Corp.

Thorne, J., Bjorkman, J., and Roth, N. 2012. Urban Growth in California: Projecting Growth in California (2000–2050) Under Six Alternative Policy Scenarios and Assessing Impacts to Future Dispersal Corridors, Fire Threats and Climate-Sensitive Agriculture. California Energy Commission Publication number: CEC-500-2012-009

World Meteorological Organization (WMO) 2006. Instruments and Observing Methods, Report No. 81: Initial guidance to obtain representative meteorological observations at urban sites (by Time Oke). WMO/TD-No. 1250

APPENDICES

Appendices A-J are available upon request under separate cover (Publication Number CEC-500-2021-XXX-ADA-J) by contacting Susan Wilhelm, Susan.Wilhelm@energy.ca.gov.